# Beam-Steering Passive Phased Array with Integrated Printed Ferroelectric Phase Shifters

Vom Fachbereich Elektrotechnik und Informationstechnik
der Technischen Universität Darmstadt
zur Erlangung der Würde eines eines
Doktor-Ingenieurs (Dr.-Ing.)
genehmigte

## Dissertation

von

M. Sc.
**Mohammad Nikfalazar**
geboren am 21.09.1983
in Teheran, Iran

| | | |
|---|---|---|
| Referent | : | Prof. Dr.-Ing. Rolf Jakoby |
| Korreferent | : | Prof. Dr. Lambert Alff |
| | | |
| Tag der Einreichung | : | 06.07.2016 |
| Tag der mündlichen Prfüng | : | 23.11.2016 |

D17
Darmstadt 2017

# Preface

This PhD thesis contains a summary of my research conducted in the Institute of Microwave Engineering and Optics (IMP) department at the Technical University of Darmstadt. Undoubtedly, I would have never reached the point of finishing my dissertation without the help and support of my supervisor, friends, and colleagues at IMP.

I would like to extend my deepest gratitude to my supervisor, Prof. Dr.-Ing. Rolf Jakoby who gave me this opportunity. I would like to thank him for his advice, helpful guidance, and valuable input.

These years have been a challenging journey with ups and downs. Several people have supported this work, contributing both academically and practically. Fortunately, I was accompanied by an extended team of experts, always willing to coach, discuss, help, and motivate me. For this support, I would like to kindly thank them. I deeply appreciate the help of Dr. Holger Maune, Dr. Yuliang Zheng, Dr. Mohsen Sazegar, Alex Wiens, Dr. Christian Kohler, Dr. Joachim R. Binder, Dr. Andreas Friederich and Morten Mikolajek in particular, in addition to the fruitful collaboration of Arzhang Mani, Arshad Mehmood and Daniel Kienemund.

The interdisciplinary cooperation with the partners from the group of Advanced Thin Film Technology (ATFT) in the Technical University of Darmstadt and the Institute for Materials Research in the Karlsruhe Institute of Technology play a pivotal part of this thesis.

I would also like to extend my love and gratitude to my mother and my father for their continued help and support. Without a doubt, my beloved wife Elnaz deserves a special word of appreciation for her moral support, patience, and love.

# Abstract

The phased array antenna (PAA) is a key concept in the realization of electronic beam forming and beam steering for numerous radar and communication applications such as detection and tracking, satellite communications and weather research. In on-the-move applications, where the beam of the antenna needs to be steered towards the transmitter or receiver, the phased array antennas offer a compact, fast, and compatible alternative to the mechanical beam steering. Significant research and development efforts towards the successful implementation and commercialization of cost-effective and efficient phased array antennas are currently underway.

One of the most important components determining the cost and performance of the phased array antennas is the phase shifter. A number of technologies have been employed for tunable phase shifters, equipped by variable capacitors. Among other technologies, ferroelectric tunable varactors offer quick tuning, low power consumption, high durability, and adequate tunability and quality factor.

In this work, the fabrication and optimization of ferroelectric varactors and their integration in a phased array antenna are discussed. In particular, barium strontium titanate (BST) material is investigated in both thin- and thick-film technologies within the framework of a number of interdisciplinary collaborations. Furthermore, thick-film technology is proposed as a low-cost and integrable solution for reconfigurable front ends. In this context, the potential of BST thick-film technology is discussed in two phase shifter structures, using the right- and left-handed loaded lines concepts. The major scientific contributions of this thesis are:

First: Design and implementation of a compact phase shifter with more than 360 ° differential phase shift for two-dimensional beam steering, which enables the array to theoretically provide a semi hemisphere area coverage. The proposed left-handed phase shifter with a compact structure based on inkjet-printed thick film achieved a phase shift of 390 ° with a FoM of 38 °/dB at 12 GHz. Consequently, the left-handed phase shifter was integrated in a two-dimensional phased array antenna on a system level. The array archived a beam scanning range of up to ± 25 ° in both E- and H-planes.

Second: Further investigation of the feasibility of fully printed phase shifters where conductive electrodes are printed as well as the ferroelectric film. Several configurations and methods for the fabrication of fully printed phase shifters were established, offering significant performance improvement in comparison to the previously reported fully printed phase shifters. This investigation include the material processing, development,

fabrication, and integration of tunable components based on inkjet- and screen-printing technologies. The fully printed phase shifter in microstrip environment achieved a phase shift of 274 ° with a FoM of 37.3 °/dB at 3 GHz. This phase shifter was implemented in a phased array with a beam scanning range reaching up to ± 30 ° for operation at S-band.

Third: The reduction of the biasing voltage has been investigated and demonstrated, which is essential to ease the system integration. Further investigation have been made to reduce the biasing voltage of the varactors based on the BST thick film. The available biasing voltage is limited in some particular applications. Therefore, it is important to develop technologies with functionality at low voltages. This work will reveal how the use of novel inkjet printing technology for the fabrication of metal-insulator-metal (MIM) varactors can reduce the biasing voltage of the tunable phase shifter based on BST thick film to a variable below 50 V with maximum tunability of 46%, which is significant improvement in comparison to the conventional tunbale phase shifters based on BST think film with biasing voltage up to 400 V. These varactors were integrated in a right-handed phase shifter at 8 GHz with a phase shift of 260 ° with a FoM of 44 °/dB. The phase shifter functionality is presented in a linear phased array antenna with a beam scanning range reaching up to ± 30 °. Moreover, the array is equipped by a dielectric resonator antenna as a compact and high efficiency-radiating element.

For further reduction of the biasing voltage below 5 V, novel processing method based on BST thin film is presented. This method employes low resistivity oxide material as a conducting bottom layer for the MIM structure. This material has a similar lattice structure compared to the BST40:60 and hence significantly reduces the defect density. Consequently, thinner BST layer are feasible without risking high leakage currents or short circuits between the top and bottom electrodes. Reduced defect density is also, ideally, accompanied by a lower film loss tangent.

# Kurzfassung

Die phasengesteuerte Gruppenantenne (PAA) ist ein Schlüsselkonzept in der Realisierung von Strahlformung und Strahlschwenkung für zahlreiche Radar- und Kommuni- kationsanwendungen wie Detektierung und Verfolgung, Satellitenkommunikation und Wetterforschung. In mobilen Anwendungen, bei denen der Antennenstrahl sich zum Sender oder Empfänger ausrichten soll, bieten phasengesteuerte Gruppenantennen eine kompakte, schnelle und kompatible Alternative zu mechanisch-gesteuerten Gruppenantennen. Aktuell gibt es vielfältige Forschungs- und Entwicklungsanstrengungen mit dem Ziel einer kosteneffizienten Implementierung und Kommerzialisierung von phasengesteuerten Gruppenantennen.

Eine der wichtigsten Komponenten phasengesteuerter Gruppenantennen sind die Phasenschieber, welche die Kosten und Leistung der Antenne maßgeblich beeinflussen. Mehrere unterschiedliche Technologien wurden genutzt, um steuerbare Phasenschieber zu implementieren, primär mit einfachen Varaktoren. Vielversprechend sind steuerbare Varaktoren auf der Basis von Ferroelektrika, die sich durch schnelle Steuerung, geringe Leistungsaufnahme, hohe Lebensdauer, sowie adäquate Steuerbarkeit und Gütefaktoren auszeichnen.

Schwerpunkt dieser Arbeit ist die Fabrikation und Optimisierung ferroelektrischer Varaktoren und ihre Integration in eine phasengesteuerte Gruppenantenne. Insbesondere wird als steuerbares Material Barium-Strontium-Titanat (BST) in Dünnfilm- und Dickfilm-Technologie untersucht. Dies erfolgt im Rahmen einer interdisziplinären Kollaboration. Weiterhin wird die Dickfilm-Technik als kostengünstige und integrierbare Lösung für rekonfigurierbare Frontends vorgestellt. In diesem Zusammenhang wird das Potential der BST-Dickfilm-Technologie in zwei neuen Phasenschieberstrukturen, mit einer linksh- ändigen Leitung und einer periodisch-belasteten Leitung diskutiert. Diese Arbeit widmet sich der Untersuchung folgender drei Aspekten:

Erstens: Entwicklung eines kompakten Phasenschiebers mit einer kontinuierlich einstellbaren differentiellen Phasenänderung von mindestens 360 ° für zweidimensionale Strahlsc- hwenkung. Dadurch würde theoretisch eine Anstrahlung des gesammten Halbraum ermö- glicht. Der vorgestellte linkshändige Leitungs-Phasenschieber in kompakter Bauform basiert auf Inkjet-gedrucktem Dickfilm. Er erreicht eine Phasenverschiebung von 390 ° und FoM von 38 °/dB bei 12 GHz. Er wurde in einer zwei-dimensionalen phasengesteuerten Gruppenantenne eingesetzt, die einen Schwenkbereich von ± 25 ° in beiden Achsen erreicht.

Zweitens: Tiefergehende Untersuchung der Machbarkeit und Realisierung von vollständig gedruckten Phasenschiebern. Hierbei sollen die metallisch leitende Schicht sowie die Isolationsschicht in einem Druckprozess realisierbar sein. In einem weiteren Ansatz werden mehrere Konfigurationen und Methoden für die Herstellung vollständig gedruckter Phasenschieber eingeführt, welche signifikante Leistungsverbesserungen im Vergleich zu bisherigen Arbeiten bieten. Diese Untersuchung beinhaltet die Materialverarbeitung, Entwicklung, Herstellung und Integration von steuerbaren Komponenten basierend auf Inkjet- und Siebdruck-Technologie. Der vollständig gedruckte Phasenschieber, realisiert in Mikrostreifenleitungstechnik, wurde in einer phasengesteuerten Gruppenantenne mit einer Arbeitsfrequenz von 3 GHz integriert. Die erreichte differenzielle Phasenänderung wurde mit 274 ° und einer FoM von 37.3 °/dB gemessen. Dadurch wurde eine Strahlschwenkung von bis zu ± 30 ° im S-Band erreicht.

Drittens: Die Verringerung der benötigten Steuerspannungen ist unumgänglich für eine direkte System-Implementierung der steuebaren Komponenten. Weitere Untersuchungen wurden angestrebt um die Bias-Spannung der BST Dickfilm-Varaktoren zu reduzieren. In manchen spezifischen Anwendungen ist die Bias-Spannung der Phasensteuerung begrenzt. Hierfür ist die Entwicklung von Technologien mit Niederspannungs-Bias wichtig. Diese Arbeit zeigt, wie der Einsatz der neuen Inkjet-Technologie in der Herstellung von BST Metall-Isolator-Metall (MIM) Varaktoren die Bias-Spannung auf unter 50 V bei einer Steuerbarkeit von 46% reduzieren kann, welches eine signifikante Verbesserung im Vergleich zu konventionellen BST Dickfilm-Phasenschiebern mit Bias-Spannungen bis zu 400 V darstellt. Diese Varaktoren wurden in einen rechtshändigen Phasenschieber integriert, welcher für eine Frequenz von 8 GHz entworfen worden ist. Die erreichte differenzielle Phase wurde mit 260 ° und einer FoM von 44 °/dB gemessen. Diese Phasenschieber-Funktionalität wird in einer linearen phasengesteuerten Gruppenantenne mit einem Schwenkbereich von ± 30 ° präsentiert. Diese Gruppenantenne ist darüberhinaus mit dielektrischen Resonatoren, als kompakte und hoch-effiziente Abstrahlelemente, ausgestattet.

Um die benötigte Steuerspannung der BST varactoren bis/unter 5 V zu reduzieren, wurden neuartige Prozessansätze für die Herstellung der Komponenten untersucht. Das Verfahren basiert auf hochleitendem Oxidmaterial, welches als Unterseitenelektrode der MIM Sturktur verwendet wird. Dieses Material besitzt eine ähnliche Gitterkonstante verglichen mit BST40:60, wodurch die Defektdichte in der BST Schicht deutlich reduziert werden kann. Demzufolge können dünnere BST Schichten realisiert werden, ohne die Gefahr von Kurzschlüssen zwischen der Ober- und Unterelektrode. Darüber hinaus führt die reduktion der Defektdichte idealerweise zu einer Reduktion des Verlustwinkels.

# Contents

# Chapter 1

# Introduction

Reconfigurable microwave components play a significant role in modern and future wireless systems. There is considerable demand for cost-effective, reconfigurable, tunable, high performance, flexible, and compact devices in radio frequency (RF) front-end modules [1]. Such smart hardware requires adaptive filters, mixers, matching networks and frequency-agile multi-band antennas, as well as polarization-agile and beam-steering antennas [2, 3]. Adaptive antennas in wireless systems are especially crucial. These antennas have a variety of communication applications, including broadcasting to enhance signal strength, space probe communications, extending the range of coverage, radar, and on-the-move [4, 5]. These adaptive antennas are used either for frequency-tuning and adaptive matching or for polarization-tuning and electronic beam steering [6].

Moreover, there is a continuous increase in data transfer rates and the pursuit of further compactness. Therefore, many of the future wireless systems will be in a frequency range above 1 GHz, in particular at S-, C-, X- and Ku-bands. The beam steering of high-gain antennas is of utmost importance for a reliable link in on-the-move applications at higher frequencies, where antennas need to adjust their beam dynamically towards the receiver/transmitter of interest [7].

The most important technical criteria for beam steering include high gain and directivity, and a fast beam scan. There are three techniques to steer the beam of the antenna: mechanically, electronically, and the hybrid method (mechanically for azimuthal movement and electronically for elevation or the other way around) [7, 8]. In a mechanical array, the phase difference between the antenna elements is constant. Therefore, the steered beam of the antenna is defined by the rotation angle.

The mechanical or hybrid method for beam steering is bulky, heavy, exhibiting a relatively low beam steering speed, sensitive to gravitational force, and costly to maintain. In contrast, the electrical beam steering phased array antennas fulfill the aforementioned set of criteria [4, 7]. In this case, the amplitude and phase difference between the antenna elements are controlled and adjusted to steer the effective beam of the array and to suppress the radiation pattern in the undesired direction [9].

There are two methods for electrical beam steering of the antenna [1, 9]:

- Passive Electronically Scanned Array: In such an array, there is a single large amplifier and source. The amplified signal is distributed and fed to each of the individual radiating elements. The phase of each radiating elements signal can be electronically varied through a phase shifter. The phase of the elements in line is reduced or increased, respectively. The multiple radiations add up to one single radiation front traveling in the desired direction [9].
- Active Electronically Scanned Array: Each array element is capable of generating its own signal, incorporating transmit/receive amplification and phase shift for altering its phase. Moreover, each individual antenna can operate at a different frequency at any given time and may change the operation frequency around 1000 times per second. Therefore, the phased array beam operates at different frequencies, as a wide band signal.

The active antenna is widely used in military radar system applications. However, such arrays are costly, require high power, generate lots of heat, and require complex signal processing. Contrarily, many commercial fields of application have emerged in recent years, which demand an alternative low cost method. In comparison to the active electronically scanned array, the passive electronically scanned array is low cost yet demands numerous low loss phase shifters. The phase shifter is an important component in the phased array antenna and has a significant influence on the array characteristics and functionality of the entire system, which includes both analog and digital phase shifters. Analog phase shifters offer continuous range of phase shifts. Comparatively, digital phase shifters have discrete values of phase shifts. In another classification, phase shifters are divided into active (amplifying while phase shifting or providing gain) and passive (attenuating while phase shifting or lossy).

### Technologies for Implementation of Tunable Phase Shifters

Compactness, loss, speed, power consumption, and maximum phase shift (tuning range) of the phase shifters as well as their integration capability are important factors for phased array antennas [6]. The cost factor of the final product is strongly influenced by the complexity of the applied technologies, namely of the variable capacitor as an important control element for the phase shifters. Since phase shifters incur a large portion of the total phased array cost, the high number of required system components leads to exorbitant expenses for commercial applications. The tunable components can be implemented through different technologies [10, 11] such as semiconductors, reconfigurable ferrite components, ferroelectrics, micro-electromechanical systems (MEMS), and liquid crystals. In the following section, the advantages and disadvantages of these technologies are expanded:

- Semiconductors: These are characterized as a well-established and cost-effective industrial technology, which are most often used in applications where only limited power capability is required [12]. On the one hand, this technology relies on complex fabrication process steps and have low linearity (power handling) and high power consumption. On the other hand, for phased arrays containing a great number of elements, the power consumption and heating of the devices become crucial [10].

- Ferrite: Reconfigurable ferrite components are preferred to high power handling. Magnetic properties of the ferrite are utilized for tunable microwave components [13]. These components show fast tuning speed and high quality factor, but have high power consumption and narrow bandwidth [10].
- MEMS: These devices show high tuning speed of the capacitance value, low power consumption, and integrability [14, 15]. On the downside, they need vacuum packaging. MEMS have a rather complex fabrication process increasing the production costs [10]. For MEMS switches, continuous tuning is not possible and each varactor is either switched off or on through the use of electrostatic forces to vary the separation between two plates. Therefore, to increase tuning resolution, numerous shunt MEMS capacitor elements need to be connected. On the other hand, MEMS varactor can tuned contentiously. But because of the periodic mechanical stress on the movable electrode, fatigue occurs usually. Therefore MEMS varactor has reliability problem.
- Liquid crystals (LC): In this technology, varactor tunability is achieved through anisotropy of the molecules [10]. LCs show low loss at millimeter wave frequencies, which are suitable for high performance phase shifters. Nevertheless, the disadvantage of this technology are high loss at frequencies below 10 GHz and low tuning speed ($>$1 s) [16, 17].
- Ferroelectrics: This material class has spontaneous electric polarization, which is altered under an external electric field. Ferroelectrics are one of the most promising candidates for application in tunable electric devices [10, 18]. Their highly tunable permittivity, as well as endurance, fast tuning speed, low power consumption, and adequate losses have enabled the realization of various integrated microwave components. The high relative permittivity considerably reduces the footprint of the capacitors, which are one of the most area-demanding components in integrated circuits. The very low power consumption of ferroelectric varactors, due to the low leakage current, is indispensable for battery-driven and power-harvesting electronics, e.g. in back scattered radio frequency identification (RFID) [6].

In summary, tunable circuits such as tunable phase shifters, require a wide tuning range and high quality factor $Q$ from the variable capacitors. The ferroelectrics show sufficient quality factor and tunability to be implemented into tunable microwave components [3, 10]. Especially for analog phase shifters, ferroelectrics are quite advanced when compared to digital phase shifters with discrete phase steps such as MEMS switch based phase shifters. On the one hand, the phase errors occur in digital phase shifters due to the approximation of the ideal phase shifts to the nearest available phase states. This error creates distinct high side lobes (quantization lobes). To reduce the level of the quantization lobes, a large number of bits to quantize the phase shifts is demanded, which complicates design and control circuits with many control lines [19]. On the other hand, the phase shifters based on ferroelectrics can achieve continuous phase shift, and thus, enable continuous steering of the antenna beam. The available voltage steps of the controlling device are the only factors that limit these phase shift steps.

The ferroelectric varactors can be realized in several technologies including ceramic (thick-film), crystal (thin-film), and bulk. In recent years, several attempts were made to fabricate phase shifters based on barium strontium titanate (BST) thin and thick films [3, 20–22]. The beam steering of the phased array antennas have been reported after employing phase shifters based on thin film BST in [23] and thick film technology in [24], however none of them present two-dimensional beam steering. One main reason for this is the higher than half wavelength size of the phase shifter, which makes it difficult to implement two-dimensional beam steering in planar arrays. Moreover, the biasing voltage in these phase shifters reach 400 V [25], which is not suitable for particular applications. The goal of this work is to determine the potential of fully printed and low voltage tunable phase shifters based on ferroelectric material for implementation in phased array antenna systems as a compact, non-complex, and low-cost technology. These phase shifters have the potential to replace the expensive semiconductor based phase shifters [10].

### Thesis Overview and Organization

**Chapter 2** addresses a review of the tunable ferroelectric materials. It chiefly introduces the tuning and dielectric loss mechanisms in BST.

**Chapter 3** provides a review of thin- and thick-film technologies for the implementation of tunable components. Screen and inkjet printing are later presented as methods for selective printing of the BST thick film. Unlike the BST thin film technology, the thick-film technology does not require vacuum processing and is easily scalable. The use of printed thick films and the implementation of a simplified fabrication process for the RF and bias circuitry significantly reduce the complexity and production cost of arrays. In particular, inkjet printing is a simple and flexible technology for selective BST film fabrication and has a high potential for the realization of planar phased arrays.

Thick BST layers have already been investigated in several works [6, 10, 26]. One limitation of the conventional thick-film varactors is the high biasing voltage (up to 400 V). To reduce the biasing voltage, the low voltage metal-insulator-metal (MIM) varactors are presented. However the use of such components requires further optimization of material properties. This is especially true for low temperature sintered BST composites to integrate into low temperature co-fired ceramics (LTCC) technology, allowing for the fabrication of fully printed tunable components. The aforementioned fabrication was achieved in this work with the interdisciplinary collaboration of material scientists in KIT. The sintering temperature of the BST layer was decreased to below 850 °C through doping and the addition of different materials. This temperature is within a suitable range for LTCC. The fabricated MIM varactor, whose electrodes were fabricated by photolithography and an inkjet-printed dielectric layer, achieves a tunability of 32 % at 8.5 GHz by applying only 25 V across a 1.2 μm thick BST film and a tunability of

46 % by applying 50 V. Further to this finding, fully printed MIM varactors with silver electrode layers are presented as a non-complex and flexible method.

**Chapter 4** covers the implementation of tunable phase shifters based on MIM varactors. The microwave properties and integrable circuit design of the phase shifter are of enormous importance for the development of the phase shifter in this work. To this end, various phase shifter concepts have been experimentally tested and analyzed with regard to their microwave properties and their integration into arrays (linear and planar). Primarily, the calculation of the array factor for the planar phased array antenna is presented to show the functionality of the phase shifters for beam steering. Furthermore, the essential parameters of the phase shifter are explained, which should be considered in the design. As proposed structures for the implementation of tunable phase shifters, an analysis of the fundamentals of the conventional right-handed transmission lines (RH-TL) and composite right/left-handed transmission lines (CRLH-TL) is given. A left-handed phase shifter based on inkjet-printed BST layer is presented as a compact structure for two-dimensional beam scanning at X/Ku-band. Moreover, novel methods for the implementation of fully screen- and inkjet-printed phase shifters are presented at L-, S-, and C-bands, which results in higher functionality (phase shift and insertion loss) and extension of the operation frequency range, in comparison to the reported fully printed components [3, 27]. Through the implementation of the presented low voltage varactor, a loaded line phase shifter at C/X-band is alternatively presented. It achieves the highest FoM/V reported for phase shifters based on BST thick film (0.88 °/(dB·V) at 8 GHz).

**Chapter 5** presents the phased array antenna demonstrator with the aforementioned BST phase shifters. The compact left-handed phase shifters were implemented in a two-dimensional beam scanning phased array antenna (4 × 4). The functionality of the printed components is demonstrated by a phased array antenna at 3 GHz, which utilizes fully printed phase shifters in a microstrip environment. Within this process, the low voltage phase shifters are implemented in a steerable phased array antenna at C/X-band. A dielectric resonator antenna, fabricated from bulk-glass ceramic, is used as a radiating element with a stacked architecture for wide bandwidth and high gain.

**Chapter 6** summarizes and concludes the work, highlighting the obtained results.

# Chapter 2

# Ferroelectric Materials for Microwave Applications

## 2.1 Dielectric Materials

Dielectric materials are electrical insulators. They are polarized under an external electric field [10, 28]. The electric charges are not free to move under the influence of an external electric field in a dielectric material as they do in a conductor. However, they are only slightly moved from their average equilibrium positions [29]. The positive and negative charges are displaced depending on the direction of the electric field. This leads to the formation of dipole moments. The dielectric polarization $P$ is the density of the dipole moments in a material.

**Permittivity**

The various properties of dielectric materials are mostly caused by their polarization. Polarization of the material under external electric field is defined by the electric susceptibility of the material $\chi_e$. This parameter influences the speed of the wave, as well as the storage capacity of the material [6, 11, 30]. The slope of the polarization curve determines the susceptibility $\chi_e$ of a nonlinear dielectric material:

$$\chi_e\,(E) = \frac{1}{\varepsilon_0}\frac{\partial P(E)}{\partial E} \tag{2.1}$$

Moreover, for linear dielectrics, the polarization is defined as a constant factor multiplied by the permittivity of free space $\varepsilon_0$ in relation to the electric field strength $E$ and the polarization $P$ (density of the dipole moments) as the following equation demonstrates:

$$P = \varepsilon_0 \chi_e E \tag{2.2}$$

The pathway of linear dielectrics has a constant slope, which results in a constant permittivity [6]. The total polarization consists of different polarization mechanisms. Under the external electric field, displacement polarization in dielectrics with a permanent dipole moment results in the arrangement and orientation of permanent dipoles. The electric displacement $D$ in relation to the polarization density $P$ is determined by:

$$D = \varepsilon_0 E + P = \varepsilon_0 (1 + \chi_e) E = \varepsilon_r \varepsilon_0 E \tag{2.3}$$

Where $\varepsilon_r$ is the relative permittivity, which is the ratio between the permittivity $\varepsilon$ and the free space permittivity $\varepsilon_0$ ($8.854\times10^{12}$ F/m), and has no units. $\chi_e$ is related to the relative permittivity $\varepsilon_r$ and is zero in the case of vacuum ($\chi_e = \varepsilon_r - 1$).

On the one hand, linear dielectrics usually have a small polarization. This leads to a small permittivity and low loss [6]. Due to these properties, linear dielectrics are often used as carrier substrates in the microwave frequencies. On the other hand, the nonlinear dielectrics have a relative permittivity depending on the applied electric field ($\varepsilon_r(E) = 1 + \chi_e(E)$), which makes them suitable for utilization in tunable components [10].

### Complex Permittivity

The dielectric permittivity $\varepsilon$ explains how a material becomes polarized by an external electric field. The permittivity has a complex value and can be defined as:

$$\varepsilon = \varepsilon'(f) - j\varepsilon''(f) \tag{2.4}$$

where $\varepsilon'$ is the real part (dielectric constant) and shows the stored electromagnetic energy as capacitance per unit length. Polarization occurs at different scales for different frequency ranges. The imaginary part of the permittivity $\varepsilon''$ (dielectric loss) shows the dissipation of the energy in the transition between the polarization mechanisms [10, 30]. The ratio between the imaginary and real parts is referred to a loss tangent:

$$\tan\delta(f) = \left|\frac{\varepsilon''(f)}{\varepsilon'(f)}\right| \tag{2.5}$$

The behavior of the real and imaginary parts of the permittivity over a wide frequency range are shown in figure 2.1. The processes that influence the response of a material to a time-varying electromagnetic field are frequency dependent [31]. There are four different mechanisms of polarization:

- Interfacial (space charge polarization): This refers to the general case of limited back and forth movement of charges in response to a time-varying electric field, which results in alignment of charge dipoles. This mechanism occurs at conductor and dielectric interfaces or at the grain boundaries.

- Dipolar (orientational polarization): Molecules (permanent dipoles) are aligned by an applied electric field in a polar dielectric. As a result, this induces a net average dipole moment per molecule and periodic rotations such as liquid crystal (LC). The absence of an electric field causes a net zero dipole moment per molecule. This mechanism changes the effective permittivity of the total material. The orientation of the molecules in LC can be achieved with both electric and magnetic fields [10].
- Ionic polarization: In this mechanism, the ions are displaced in the crystal lattice under the applied external electric field [10]. This type of polarization is named ionic polarization, which occurs in ionic crystals such as NaCl and KCl. The orientational and ionic polarizations are mainly responsible for the ferroelectric effect. This mechanism is used in the displacement of titanium ion in the crystal lattice of BST [29].
- Electronic polarization: This polarization arises from the displacement of electrons with respect to the associated nuclei in opposite directions of the external electric field.

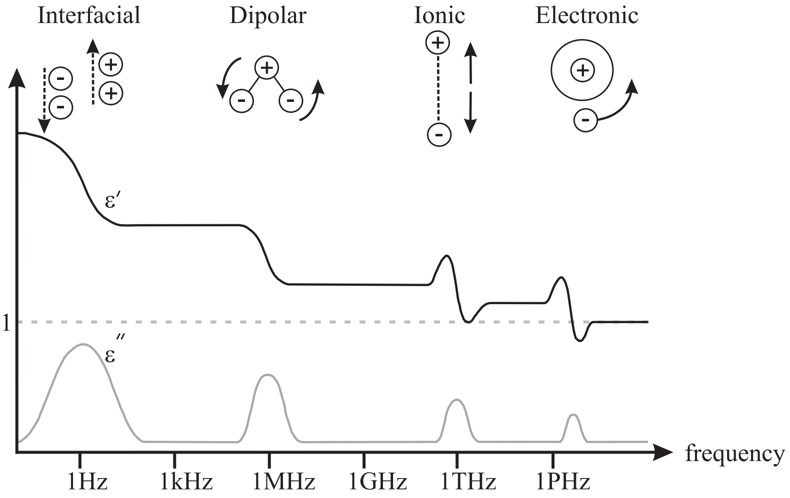

**Figure 2.1:** The dielectric permittivity versus frequency, where ′ is the real part and ″ is the imaginary part of the permittivity.

For all four mechanisms, there is a cut-off frequency in which their contribution to the permittivity disappears above a certain threshold (figure 2.1). The relative permittivity follows one above the resonance frequency of the electronic polarization.

### Controllable Ferroelectric Materials

Different classes of dielectric materials are shown in figure 2.2 [32]. A brief description of each class follows:

- Piezoelectrics: The solid group with piezoelectric properties is a subgroup of dielectric materials. Piezoelectricity is a reversible process which occurs through the linear electromechanical interaction between the mechanical state and electrical state in crystals in the absence of an inversion symmetry [11]. In this case, the applied mechanical force or electric field generates the electrical charge or mechanical strain, which can potentially be used as the piezoelectric ultrasonic transducer to generate sound waves [10].

- Pyroelectricity: In certain ion crystals, the electricity is generated when the positions of the atoms are altered in crystal structures under temperature changes [11]. This effect is used in temperature sensors [18].

- Ferroelectricity: In certain pyroelectric materials, the direction of the spontaneous polarization can be altered under an external electric field. Such pyroelectric materials are referred to as ferroelectrics. The polarization of ferroelectric materials can be reversed through the change of the direction of the external electric field. In ferroelectric materials, ion polarization is responsible for a change in the relative permittivity. The external polarization causes the ions to become displaced from their equilibrium state. As a consequence, the permittivity is changed.

  A typical property of ferroelectric materials is the hysteresis effect. The hysteresis effect is caused by the presence of several energetically equivalent states within the crystal lattice. The ferroelectric perovskites, with a chemical formula of $ABO_3$ and oxygen in the face centers, have tetragonal crystal structures (figure 2.3(a)). The hysteresis effect (butterfly) is shown in the figure 2.3(b). Applying an electric field for the first time increases the polarization from zero up to a certain point ($\pm P_r$). When the field strength is once again reduced to zero, a residual polarization remains and, hence, the polarization will be zero at a reverse electric field of $-E_c$. This effect of the ferroelectric phase is especially interesting for ferroelectric-random-access-memory (FeRAM) [30]. The temperature dependence of the spontaneous polarization based on the pyroelectric effect is another feature of the ferroelectrics, shown in figure 2.3(c). A change of temperature leads to a spatial distortion of the crystal lattice and thus causes a change of the spontaneous polarization. Dielectric materials demonstrate ferroelectricity only below a certain phase transition temperature, called the curie temperature $T_C$, and are paraelectric above this temperature.

- Paraelectricity: Above the phase transition temperature, the spontaneous polarization vanishes. In this phase, which is called paraelectric phase, symmetry in the crystal lattice appears due to the lack of spontaneous polarization (cubic crystal structure figure 2.3(d)) and no hysteresis effect is observed (figure 2.3(e)). The paraelectric material can be used as high quality dielectric in tunable capacitors for microwave application [10, 30].

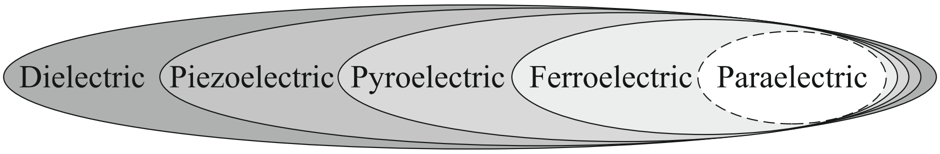

**Figure 2.2:** The relationship between dielectric, piezoelectric, pyroelectric, ferroelectric and paraelectric materials [32]

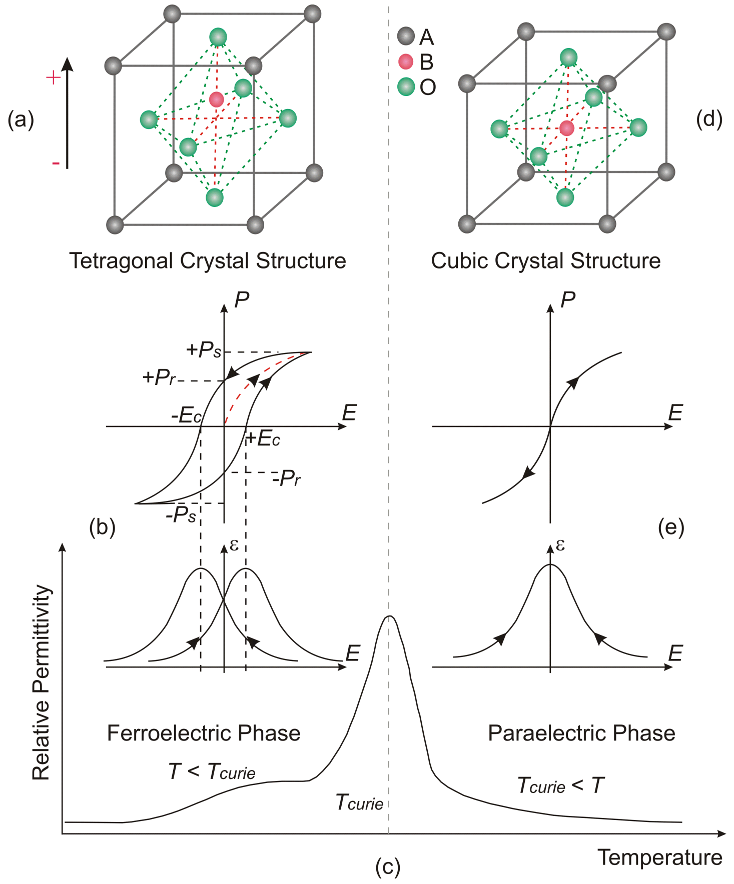

**Figure 2.3:** Tetragonal crystal structure (a) and hysteresis behavior of permittivity (b) of dielectric material in ferroelectric phase. Schematic representation of the temperature dependence of the permittivity of BST (c). Cubic crystal structure (d) and permittivity behavior (e) of dielectric material in paraelectric phase.

### Phenomenological Theory

The free energy $F$ of the ferroelectric crystal can be defined by polarization density $P$ [10, 11]:

$$F(P,T) = \frac{1}{2}\alpha P^2 + \frac{1}{4}\beta P^4 + ... \tag{2.6}$$

This equation is valid for ferroelectric and paraelectric phases. Since free energy does not depend on the direction of the electric field, only the even terms of $P$ are considered [10]. The first derivative results in:

$$\frac{\partial F(P,T)}{\partial P} = E = \alpha P + \beta P^3 + ... \tag{2.7}$$

where $\alpha$ is equal to $1/\varepsilon_0\varepsilon_r$ from the simple relationship of the electrical field and polarization. Based on Curie-Weiss law, the temperature dependency of relative permittivity is $\varepsilon_r = C/(T - T_C)$. Where $C$ is Curie constant, $T$ is temperature, and $T_C$ is Curie temperature. Therefore, the coefficient $\alpha$ is defined by $\alpha = (T - T_\mathrm{C})/\varepsilon_0 C$. The spontaneous polarization $P_s$ can be found at zero external electrical field ($\alpha P_s + \beta {P_s}^3 = 0$), which has two solutions:

$$P_{s1} = 0 \quad , \quad P_{s2} = \sqrt{\frac{T_C - T}{\varepsilon_0 \beta C}} \tag{2.8}$$

where $P_{s1}$ is valid for temperatures above curie temperature (paraelectric phase) and $P_{s2}$ is valid below curie temperature (ferroelectric phase). The dielectric relative permittivity $\varepsilon_r$ is calculated by:

$$\varepsilon_r = \frac{1}{\varepsilon_0}.\frac{\partial E}{\partial P} = \frac{1}{\varepsilon_0}.\frac{1}{(\alpha + 3\beta P^2)} \tag{2.9}$$

Without an external electrical field, relative permittivity is equal to $C/(T - T_C)$ for the paraelectric phase and equal to $C/2(T_C - T)$ for the ferroelectric phase. The relative permittivity under the external electrical field has a parabolic dependence in the paraelectric phase. By replacing $P = \varepsilon_0\varepsilon_r(0,T)E$ in the equation 2.9 [10], relative permittivity follows:

$$\varepsilon_r(E,T) = \frac{\varepsilon_r(0,T)}{1 + 3\beta(\varepsilon_0\varepsilon_r(0,T))^3 E^2} \tag{2.10}$$

where $\varepsilon_r(0,T)$ is equal to $C/(T - T_C)$. Figure 2.4 illustrates the polarization versus free energy for different temperature ranges. The two minimums in $T < T_C$ correspond to the spontaneous polarization $\pm P_s$.

The tunability $\tau_\varepsilon$ represents the dependence of the relative permittivity to the electrical field:

$$\tau_\varepsilon(E) = \frac{\Delta\varepsilon}{\varepsilon(0)} = \frac{\varepsilon(0) - \varepsilon(E)}{\varepsilon(0)} \tag{2.11}$$

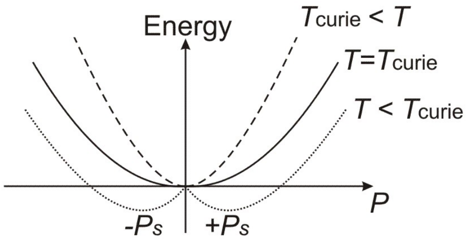

**Figure 2.4:** The free energy versus polarization for different temperature ranges.

where $\varepsilon(E)$ is the electrical field dependent permittivity and $\varepsilon(0)$ is maximum permittivity without external electrical field ($\varepsilon(E)$=$\varepsilon_0\varepsilon_r(E)$).

## 2.2 Barium Strontium Titanate

The ferroelectric perovskites such as barium strontium titanate (BST) are suitable for microwave applications of the varactors due to the relatively high permittivity and tunability of the material [10, 30]. In particular, the solid BST is used due to the fact that ferroelectric and paraelectric phase transition temperature (the curie temperature $T_C$) can be adjusted by the barium content. In this case, BST can be synthesized between $BaTiO_3$ and $SrTiO_3$ mixed crystals depending on barium stoichiometry of the material ($Ba_xSr_{1-x}TiO_3$, $0 < x < 1$). Curie point can be shifted due to the composition and is optimized for room temperature applications. The Curie point can be approximated depending on the mixture $x$ factor by [6]:

$$T_c(x) = \left[42 + 439.37x - 95.95x^2\right] K \tag{2.12}$$

The relationship of the $x$-factor and the Curie point of the BST is illustrated in figure 2.5. For $x = 0.6$ ($Ba_{0.6}Sr_{0.4}TiO_3$), the Curie temperature is -2 °C. Moreover, figure 2.6 shows the temperature dependency of the permittivity of BST ceramic with sintering temperature of 1400 °C [33]. In this investigation different mixtures of the $Ba_xSr_{1-x}TiO_3$ are measured and show the different Curie points. At the Curie temperature, each BST composition has its maximal point of permittivity. Moreover, as explained in [33], depending on the sintering temperature, the maximum value of the relative permittivity varies.

Figure 2.6 shows the permittivity of the BST bulk ceramic and BST thick film for the same stoichiometry of $Ba_{0.6}Sr_{0.4}TiO_3$ versus temperature [34]. Due to the small particle size and the high porosity, the maximum permittivity of the thick film is lower than the bulk ceramic. In addition, the thick film shows a less pronounced phase transition and a weaker dependence of permittivity on the temperature [34]. The growing grain size increases the permittivity and shifts the phase transition to higher temperatures. The impurities in the material and high porosity of the BST thick film influence the values of

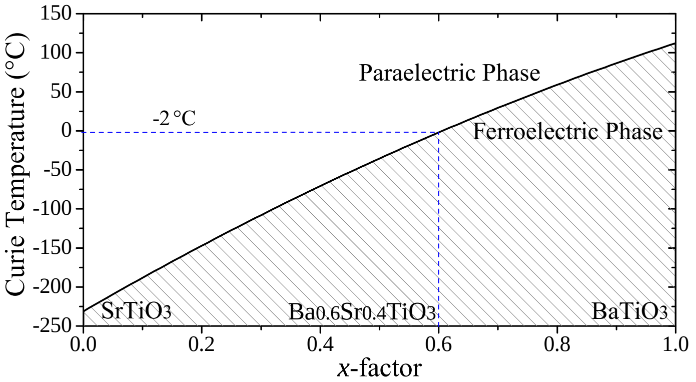

**Figure 2.5:** Curie temperature of $Ba_xSr_{1-x}TiO_3$ with different Ba contents ($x$-factor).

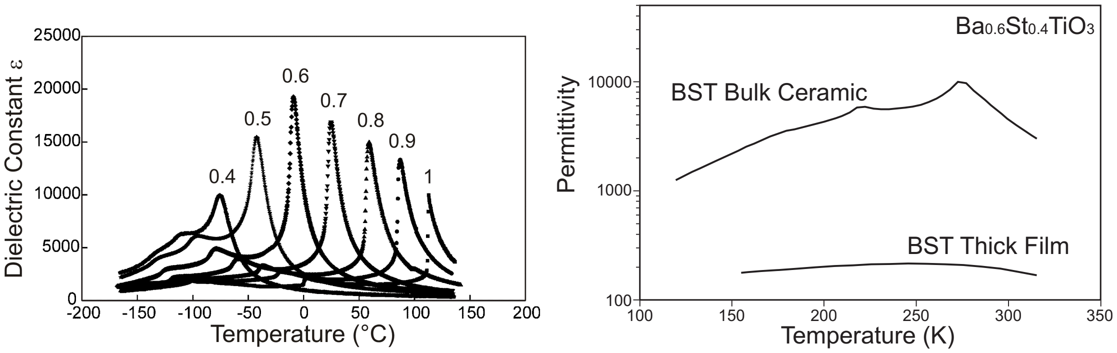

**Figure 2.6:** The permittivity versus temperature of $Ba_xSr_{1-x}TiO_3$ ceramics sintered at 1400 °C for one hour with different concentrations of Ba ($x$-factor) (left) [33]. The permittivity of the BST bulk ceramic and BST thick film for $x = 0.6$ versus temperature (right) [34].

the permittivity [28]. The same behavior is observed in thin films, which is caused by mechanical stresses in the layers, induced by the different thermal expansion coefficients at the interface of substrate/film [35].

For BST thin films, the dimension of the films is close to the crystal grains and the permittivity of BST is different from bulk ceramic. To justify this, a model of serial capacitors can be employed. On the surface of a BST thin-film, a layer with low permittivity between the BST film, electrodes and the substrate forms, such a layer is referred to as dead layer [11]. Here, the effect of the dead layers is more significant than in bulk ceramic, which is caused by external mechanisms, the charge barrier, and defects of the film [10, 11].

### Dielectric Loss in BST Film

In the microwave tunable components based on BST film, ferroelectric materials in the paraelectric phase (above Curie temperature) mainly cause dielectric losses [10, 30, 34]. The ferroelectric loss is higher than that of common non-tunable dielectrics and can be divided into:

- Intrinsic loss: This is characterized by the interaction of the electromagnetic or microwave field with the crystal structure and includes fundamental losses originated from the absorption of the microwave quanta by phonons of the material [34], which attributes to the structure of the material system and cannot significantly decrease. Three-quantum mechanism, four-quantum mechanism, and the residual ferroelectric polarization (quasi-debye loss) are the fundamental mechanisms of intrinsic loss [28, 34]. The quasi-debye loss is the transformation of microwave electric field oscillations into acoustic oscillations. This kind of loss arises through the relaxation of phonons in the THz frequency range.

- Extrinsic loss: The experiments demonstrate that in the thin- and thick-film ferroelectric varactors, the extrinsic losses dominate over the intrinsic ones in the microwave frequency range [36]. The following mechanisms are the main cause of the extrinsic loss:

    - Motion of charged defects (CD) is considered the dominant loss mechanism in BST [34], leading to a piezoelectric coupling of a part of the high-frequency wave energy, which is transformed into acoustic vibrations due to scattering of charged defects [28, 30]. Charged defects can be reduced through the doping of the BST thick films [34]. The charged defect dependency can be rationalized by the following simplified equation:

      $$\tan\delta_{CD} \propto n_d Z^2 \varepsilon(E) f(\omega,r_c) \tag{2.13}$$

      where $Z$ is the effective charge number of the defects, $\omega$ is the angular frequency, $r_c$ is the correlation length of the charge distribution, $\varepsilon(E)$ is the permittivity, and $n_d$ is the atomic concentration of defects [34].

    - Variation in charge transport barriers at the grain boundaries of the ferroelectric film.

    - Impact of local polar regions induced by various defects and structural imperfections of the ferroelectric film.

    - Formation of the lossy layer at the interfaces between the ferroelectric film and conducting electrodes, also known as dead layers.

Figure 2.7 illustrates the two loss mechanisms and their contribution to the overall loss in the absence of an electrical field. The perfect crystal structure has the lowest loss, due to low defect density. Therefore, the loss of the ferroelectric varactors can be improved by increasing BST crystal quality and reducing the density of the defects in the ferroelectric films. Moreover, unlike the intrinsic ones, the extrinsic losses (charged defects) can be reduced considerably through appropriate material additives and doping [6, 34].

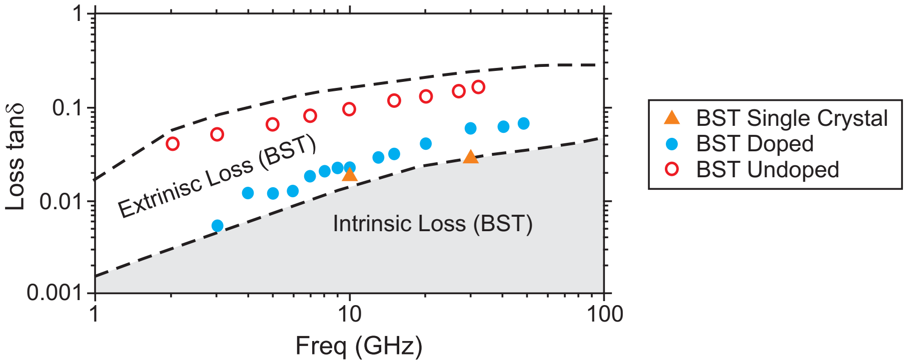

**Figure 2.7:** Loss tangent of ceramic thick films based on BST [34].

# Chapter 3

# Ferroelectric Varactors

The performance of tunable components based on ferroelectric material is influenced by processing methods [11]. For the fabrication and integration of ferroelectric films, three different technologies are used: bulk material, thin-film, and thick-film [30, 35]. The bulk technology is used for high power ferroelectric capasitors [10]. One limitation of this method is the rather high voltage needed for applying the required DC bias (20 kV/cm or higher) to obtain a high tunability, usually for stand-alone devices only. Moreover, technical reasons hinder the integration of bulk BST material into RF circuits [10]. Therefore, the thin-film and thick-film processing technologies are preferred for the integration of BST into RF components.

The thin-film technology, with a layer thickness in the range of a few tens to hundreds of nanometers, is frequently used to investigate and develop materials specifficaly for tunable microwave components [10, 11]. The demand for miniaturization of the ferroelectric varactors and their integration into existing technologies is one of the main motivations for the development of thin-film ferroelectric varactors. In particular, this technology is of high interest due to its integration capability with standard monolithic microwave integrated circuit (MMIC) processes. Thin films in general can sustain higher electrical field in comparison to bulk material [10]. Nevertheless, due to the nanometer-thick BST layers, ferroelectric varactors based on the BST thin films can be tuned with low bias voltages below 5 V [11, 34]. Moreover, temperature-dependency of the permittivity in thin films is smaller than that of the bulk materials [6].

However, thin-film technology still demands a complex processing, which usually relies on high vacuum technology similar to semiconductor processes [30]. Alternatively, thick-film technologies are mainly based on printing methods. The material fabrication and process of printing, if optimized, is a simple and low cost method, as the film fabrication does not require ultra-high vacuum and complex processing [6].

In this chapter, as an alternative to the aforementioned thin-film technology, the thick-film printing technology for the realization and fabrication of the planar and multilayer structures is presented, implementing different BST film fabrication technologies. Particularly, the printing technology is shown to be a good candidate for the implementation of the fully printed tunable components in reconfigurable RF front-ends. The components' functionality is improved by technological modifications and optimizations. This investigation have been done in cooperation with the Material Process Technology group at Karlsruhe Institute of Technology (KIT).

## 3.1 BST Thick Film

There are different printing techniques to process dielectric thick films with thickness in the micrometer range, which all have a significant influence on the performance of the devices [10]. Therefore, the topology of the components design is influenced by the implementation techniques. The printing technology is based on four steps: the processing of a paste or an ink (ink has higher dilution), printing, drying, and firing. The most used substrates for thick film processing are alumina substrates, which do not react with the BST layer below a sintering temperature of 1200 °C. In the first step, the BST paste or ink is initially printed on top of the carrier substrate. Thereafter, it is dried and fired in an air atmosphere. The printing process can be repeated several times depending on how many layers are needed to obtain the required thickness. Typically, the number of layers does not amount to more than seven layers. To increase this, one possibility involves the use of a LTCC method. In this technology, the substrates and film layers are co-fired at the same time. The conventional sintering temperature for LTCC samples is 850 °C. There are different methods for the printing of dielectric and conductor layers. In this thesis, two fabrication methods will be explained, which are used for the implementation of the tunable components: inkjet printing and screen printing.

### 3.1.1 Inkjet-Printed Thick Film Ceramics

There is high demand in the fabrication of the printed circuit, especially reconfigurable components. In the last decade, inkjet printing was used widely in digital techniques, particularly for graphic printing. Currently, there are no reported tunable components based on inkjet printing technology used in a frequency range above 1 GHz. This method prints a digital image by propelling a droplet of ink onto the substrates. In comparison to conventional screen printing and roll-to-roll printing methods, inkjet printing has high flexibility for processing [37–39]. It possesses the following advantages:

- Contact and mask-less
- Printing of two- and three-dimensional structures from digital model
- Wide variety of substrates for printing
- Multiple print head and simultaneous printing of different materials
- Cost effective and flexible

Depending on the substrate, material and printing head, however, inkjet printing has a minimum printing feature size of 30 µm [28]. The chosen technology for inkjet printed functional materials is usually the piezoelectric drop-on-demand (DOD) technology. The drop ejection is achieved through the contraction of a piezoelectric element in the print head. By using this technique, drops of a fixed size and quantity of ink are obtained. Figure 3.1 shows the basic process of the inkjet printing. By applying voltage to the piezoelectric actuator, the positive pressure wave is produced and pushes the ink outwards. The amount of this wave can control the velocity of the droplet [40].

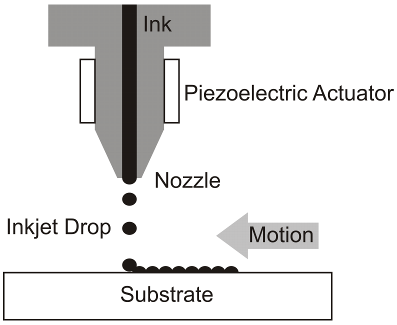

**Figure 3.1:** The basic process of a piezoelectric inkjet print head.

The main challenge of the inkjet printing process is to achieve a uniform particle deposition and a high film homogeneity [41]. The combination of several grains create particles. A grain is a single crystal which is randomly oriented and separated by grain boundaries.

Low particle viscosity leads to problems during printing and drying such as line deformation or inhomogeneous film thickness. The prevention of the purported coffee stain effect is of especially great importance in order to achieve the demanding requirements for microwave components [28]. The material must be in the liquid phase, dissolved, or dispersed in a solvent which becomes the ink of the printer [42, 43]. The control of the process parameters and the ink is therefore necessary [37].

The width and thickness of the printed lines are defined by the drop distance and the interaction with the substrate. The minimum line width is equal to the diameter ($d$) of the drop [44]. The line width can be calculated by the following:

$$W = d \cdot \sin\theta \cdot \sqrt[3]{\frac{4}{(2+\cos\theta)\cdot(1-\cos\theta)^2}} \tag{3.1}$$

where $\theta$ is the contact angle and typical value of $\theta$ for BST ink is around 45 ° .

## Ink Preparation

In inkjet printing, three optimized inks for drying based on recent investigations of Friederich [28] from KIT are used, which are well suited for the fabrication of printed microwave components:

- Undoped BST: Pure $Ba_{0.6}Sr_{0.4}TiO_3$ powder prepared for the first ink. In this thesis, the preparation of the powder was carried out by a modified sol-gel process, which allows for the production of doped and undoped BST powders [45]. Figure 3.2 shows the schematic sequence of the BST ceramic powder preparation. The sol-gel process allows for the production of ceramic powder with small particle sizes and a homogeneous distribution at the atomic level, which are advantageous for doping [28]. The process can be broken down into the following phases: sol synthesis, spray drying, and calcination. The nominal stoichiometric composition in this thesis is $Ba_{0.6}Sr_{0.4}TiO_3$. As raw materials titanium isopropoxide, strontium acetate, barium-acetate were used. The metal-organic precursors were calcined under dried purified air.

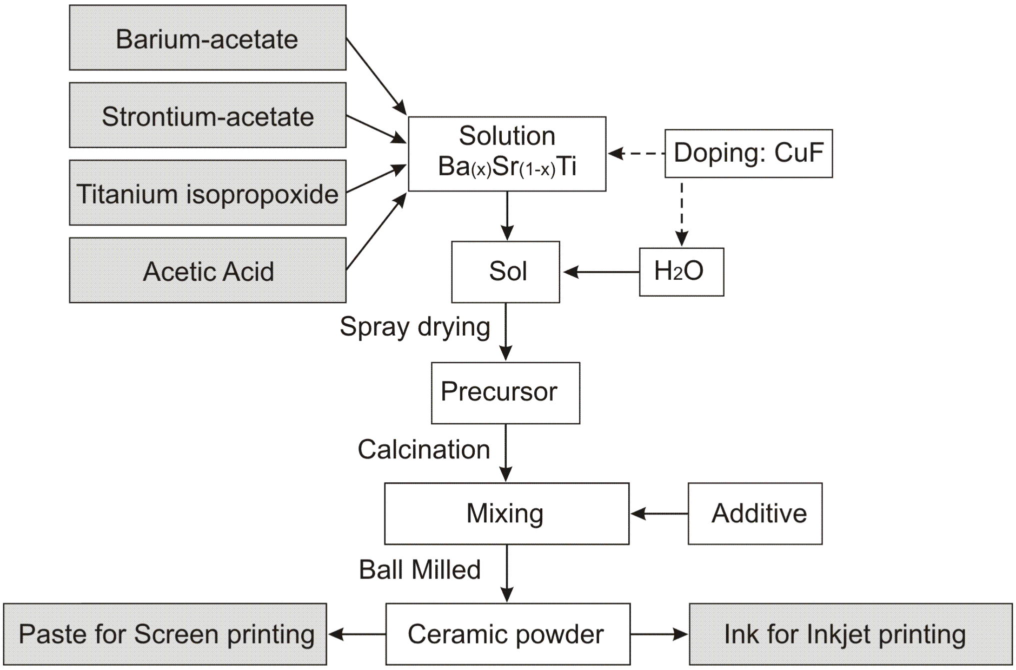

**Figure 3.2:** Preparation of the BST ceramic powder for screen and inkjet printing.

- Doped BST: For the second one, Cu-F codoped BST is mixed with a solvent through selective doping in the BST material system. The copper-acetate and Trifluoroacetic acid were used as copper and fluorine sources. The crystal lattice and, therefore, the dielectric properties can be modified by selective doping. The doping can influence and reduce defect concentrations at the atomic structure [28]. Moreover, the doping causes a change in the grain growth at the microscopic level. Therefore, the thick-film composition is further modified with copper-fluorine dopant in $Ba_{0.6}Sr_{0.4}TiO_3$ powder to achieve the best compromise between low porosity, high sintering activity as well as adequate dielectric properties of the thick-film.
- BST-ZnO-$B_2O_3$ Composites: This ink is prepared to obtain a composition suitable for a low-temperature co-firing process and fabrication of multilayer struc-

> tures. Kohler et al. shows in [46, 47] that a small addition of ZnO-$H_3BO_3$ to the BST powder can reduce the sintering temperature of BST-full ceramic and screen-printed BST thick film. For ink preparation, in contrast to [46], the additive was contributed by means $B_2O_3$ instead of $H_3BO_3$ to prevent condensation. The ink is prepared by adding 0.76% w/w ZnO (Nanostructured Amorphous Materials, Houston, TX) and 0.65% w/w $B_2O_3$ (Alfa Aesar, Ward Hill, MA) to the undoped BST powder.

The calcination of the metal-organic precursor is performed at 1100 °C for the first and third samples and is reduced to 900 °C for the second sample in the period of one hour to obtain a fine grained ceramic powder.

The schematic sequence of the ink preparation and sintering of the printed BST layer are shown in figure 3.3. For ink preparation, highly agglomerated powder was grinded and dispersed in an organic butyl diglycol (Merck) solvent and DOLACOL D1001 (Zschimmer Schwarz) dispersant using a stirred media mill (NETZSCH Feinmahltechnik, MiniCer). Before starting the milling, 40% w/w powder and 1.6% w/w dispersant are mixed in the solvent. This is followed by partially diluting the suspensions to a solid content by volume of $\Phi = 5$ vol.%, with the addition of 49 vol.% isopropanol alcohol (IPA, Merck) as a fast drying agent, and 1 vol.% ethyl cellulose (EC, Sigma-Aldrich) as a rheology additive to adjust the ink rheology.

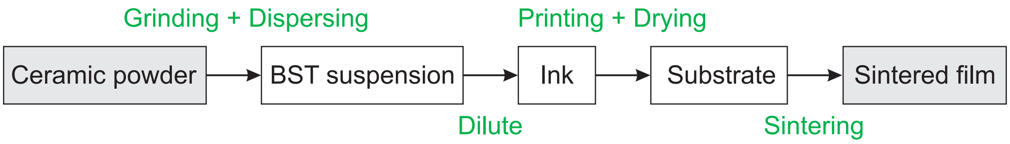

**Figure 3.3:** Processing steps from the fabrication of the BST ink to sintered BST thick film.

The printability of the inks is qualified by Ohnesorge ($Oh$) parameter [48], which is defined by:

$$Oh = \frac{\eta}{\sqrt{\gamma \rho a}} \tag{3.2}$$

where $\eta$ is the dynamic viscosity, $\gamma$ is the surface tension and $\rho$ is the density of the ink. $a$ represents the characteristic length (Nozzel diameter), which is 100 µm for the dielectric ink and 70 µm for the silver ink. In this thesis, a commercially available nanoparticle silver ink (EMD5603; Sun Chemical, Parsippany, NJ) with 20% w/w silver content is used as electrode film in the inkjet printing (table 3.1).

The $Oh$ parameter should be in the range of 0.1 to 1 for the ink to be printable [41]. To ensure a stable printing process, the inks are characterized with respect to their printability. The medium particle size is measured through image analysis after grinding.

Table 3.1 gives the results for particle size $d_{50}$ and inks properties. The Ohnesorge number $Oh$ of the inks is calculated according to equation 3.2. The calculated values of $Oh$ parameter are in the suggested range for a stable drop formation. These results show well printable inks at room temperature (20 °C).

**Table 3.1:** Results of ink properties at 20 °C.

| Ink | $d_{50}$ (nm) | $\eta$ (mPas) | $\rho$ (g/cm$^3$) | $\gamma$ (mN/n) | $Oh$ |
|---|---|---|---|---|---|
| Undoped BST | 270 | 22.7 | 1.11 | 24.4 | 0.44 |
| Cu-F Doped BST | 170 | 33.6 | 1.08 | 24.2 | 0.66 |
| BST-ZnO-$B_2O_3$ | 200 | 34 | 1.08 | 23.9 | 0.67 |
| Ag | $\leq$50 | 15.5 | 1.28 | 50 | 0.38 |

The obtained BST inks were printed using a single nozzle piezoelectric drop-on-demand inkjet printer (Autodrop Professional; Microdrop, Norderstedt, Germany). The inkjet printing was performed with 100 µm nozzle diameter. Stable drop formation of the BST ink was achieved with the driving voltage of the piezo actuator $U_{\text{Head}} = 120\,\text{V}$ and the pulse length $t_{\text{Head}} = 12\,\mu\text{s}$ at an ejection frequency of 500 Hz. The drop distance and the substrate temperature can be adjusted to control the topography of the printed lines. The BST lines were printed on a heated poly-crystalline alumina substrates (Rubalit 710, Ceram-Tec) and dried at 45 to 50 °C. Afterwards, the samples were sintered in a tube furnace (CTF1600, Heraeus, Hanau) for one hour with heating and cooling rates of 5 K/min. Figure 3.4 illustrates the topography of a line of the inkjet-printed BST film on top of the alumina substrate, which was used for the characterization of the microwave properties.

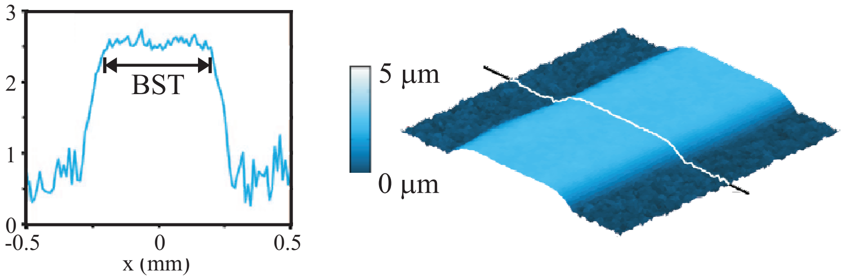

**Figure 3.4:** Topography of an inkjet-printed BST line.

## 3.1.2 Screen-Printed Thick Film Ceramics

Screen printing is a technique used for the film fabrication of multilayer structures (automatic, semiautomatic, and manual ones). An essential part of screen-printing is the screen. On this screen, a stencil is formed by blocking certain parts of the screen via by a polymeric layer. In this method, a paste is transferred through a patterned screen mesh for printing by a squeegee. The residual open spaces result in the positive image of the design, which is screen-printed on the substrate. Figure 3.5 illustrates the basic screen printing processing steps, which are based on moving a squeegee over the screen, the transferring of the paste through the open screen, and its patterning on the substrate.

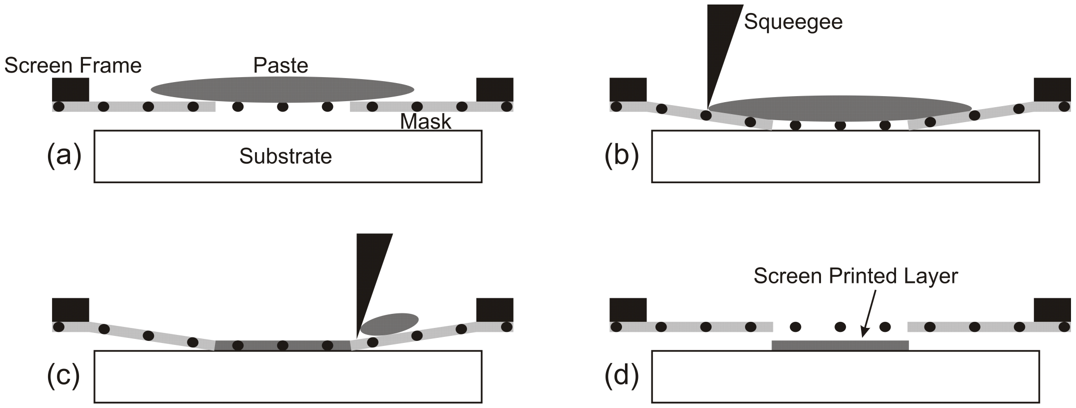

**Figure 3.5:** The process of screen printing. (a) Placing paste on top of the screen. (b) The squeegee presses the screen with force to the substrate. (c) The squeegee prints the paste onto the substrate. (d) Upon lifting the squeegee, the screen springs back.

By using different masks, it is possible to pattern dielectric and conductor layers after one other to fabricate fully printed and low cost multilayer components. Currently, the limitation of the line width and gap resolution based on screen printing is around 100 µm.

### Paste Preparation

In this work, two approaches based on recent investigations of Kohler [49] from KIT were used for the fabrication of the low temperature sintered BST composite paste, which were aiming to be implemented in multilayer structures:

- The BST powder preparation of undoped BST powder and copper-fluorine (Cu-F) co-doped BST powders were produced. The metal-organic precursors were calcined under dried purified air at 900 °C for one hour. The resulting powders possessed a specific surface area of 19.6 $m^2/g$ for undoped BST and 2.8 $m^2/g$ for Cu-F codoped BST. In the next step, the powders were mixed with different amounts of powder mixture of ZnO and $H_3BO_3$ as an additive for low temperature sintering purposes. Later, the powder mixtures were ball milled for one day in acetone with zirconia grinding media [46, 47]. With respect to the additive content in vol.%, ZnO and $H_3BO_3$ were added in different amounts (5 and 20 vol.%, respectively, resulting composites named BST-5ZB, BST-20ZB, CuF-BST-5ZB, and CuF-BST-20ZB) to the powder, obtaining a composition suitable for low-temperature sintering.

- In the second approach, ferroelectric composite thick-films based on undoped BST and magnesium borate ($Mg_3B_2O_6$) were produced. The potential of this composite ceramic as a tunable material was already demonstrated as a bulk material [50, 51] and was adapted to thick-film technology in this work. Thus, two different compositions of BST and $Mg_3B_2O_6$ were selected, with equal amounts of BST and MBO 50 vol.% ($50BST-50Mg_3B_2O_6$), as well as 80 vol.% BST and 20 vol.% $Mg_3B_2O_6$ ($80BST-20Mg_3B_2O_6$).

Figure 3.6 shows the paste preparation process for screen printing. The powder mixtures of all composite systems were grinded and dispersed in an organic solvent (terpineol) with a binder (ethyl cellulose) and dispersant (Hypermer KD1; Uniqema GmbH Co., KG, Emmerich, Germany) by means of an electronic three roll mill (EXAKT 80E; EXAKT Technologies, Norderstedt, Germany) [46]. The fabricated BST paste was screen-printed on an alumina substrate, dried, and subsequently sintered for one hour. The used mesh consists of 325 wires per inch, resulting in a screen-printed layer thickness of around 5 µm and a minimum feature resolution of 100 µm.

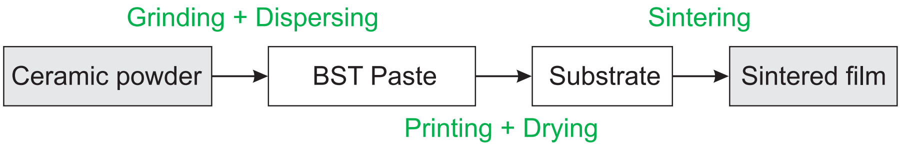

**Figure 3.6:** Preparation of the BST paste for screen printing.

## 3.2 Conformal Mapping and Characterization of Coplanar Wave Guide

The commercially available simulation software are used for the modeling of the complex microwave structures [10]. However, this software presents some accuracy problems for the narrow BST layer with high-permittivity and non-linear permittivity, which is dependent on the electrical field [6]. There are different methods for the characterization of dielectric properties such as: the direct method performed by measuring the capacitance with an impedance analyzer, the waveguide method measuring the S-parameters by network analyzer, and a resonator method such as the Hakki-Coleman method, which consists of measuring resonant frequency and the quality factor of the resonator [30].

In this thesis, the characterization of the thick film BST is achieved through the addition of the coplanar wave guide (CPW) transmission line on top of a BST layer, which is calculated by conformal mapping and partial capacitance techniques [52, 53]. The characteristics are described analytically as a function of the geometry and dielectric properties of the substrates. Moreover, this method is faster than the time-consuming full-wave simulation software for an unknown thick film layer such as the BST. This characterization method requires two input sets:

- The S-parameters of the measured CPW on the BST layer.
- The estimated BST layer properties (the relative permittivity and loss tangent), which are roughly estimated from the measured data.

Figure 3.7 shows the layout and unit cell equivalent circuit of a lossy coplanar line on multilayer substrates, which can be used to model quasi-TEM wave propagation on the CPW line. The properties of the BST layer are defined by the unit cell elements $(R, L, C, G)$

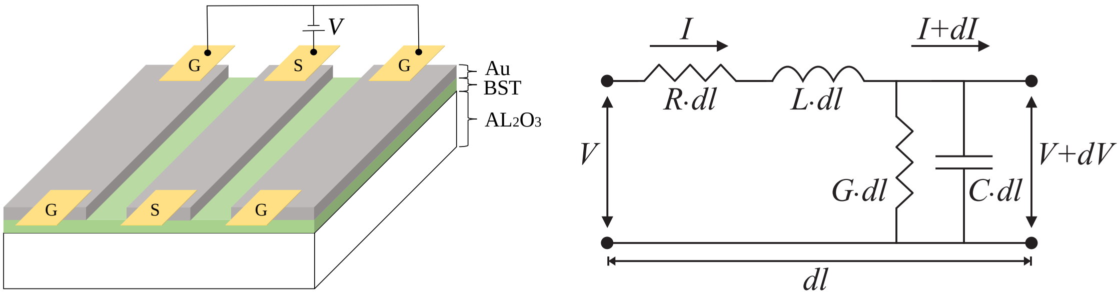

**Figure 3.7:** The CPW line configuration on top of BST layer (left). The lossy waveguide equivalent circuit model (right).

- Capacitance $C$:

  Figure 3.8 illustrates the cross-sectional arrangement of the CPW line as a symmetrical structure and the technique to divide the double-layered structure into the three parallel capacitors ($C = C_0 + C_1 + C_2$), which have modified relative permittivity [6, 52]. The admittance is explained as following:

$$Y = j\omega C + G \tag{3.3}$$

$$C = \frac{\varepsilon_0 \varepsilon_r' A}{d} \quad , \quad G = \frac{\omega \varepsilon_0 \varepsilon_r'' A}{d} \tag{3.4}$$

$$G = \omega C \tan\left(\delta_{\varepsilon_r}\right) \tag{3.5}$$

where $A$ represents the area and $d$ the distance between capacitance electrodes. In this calculation, the partial capacity is made under the assumption of an infinitely thin conductor layer [6]. Total capacitance can be calculated from the effective relative permittivity $\varepsilon_{r\text{-eff}}$ and the line capacitance $C_0$ in the absence of dielectrics.

$$C = \varepsilon_r' \cdot C_0 = 4\varepsilon_0 \varepsilon_r' \frac{K(k_0)}{K(k_0')} \tag{3.6}$$

where $K(k_0)$ and $K(k_0')$ are complete elliptic integrals of the first order [53]. $k_i'$ is represent the complementary modulus $k_i' = \sqrt{1-k_i^2}$. The elliptic integral is explained as following [52]:

$$k_0 = \frac{s}{s+g} \quad , \quad k_i = \frac{\sinh(\frac{\pi s}{2h_i})}{\sinh(\frac{\pi(s+g)}{2h_i})} \tag{3.7}$$

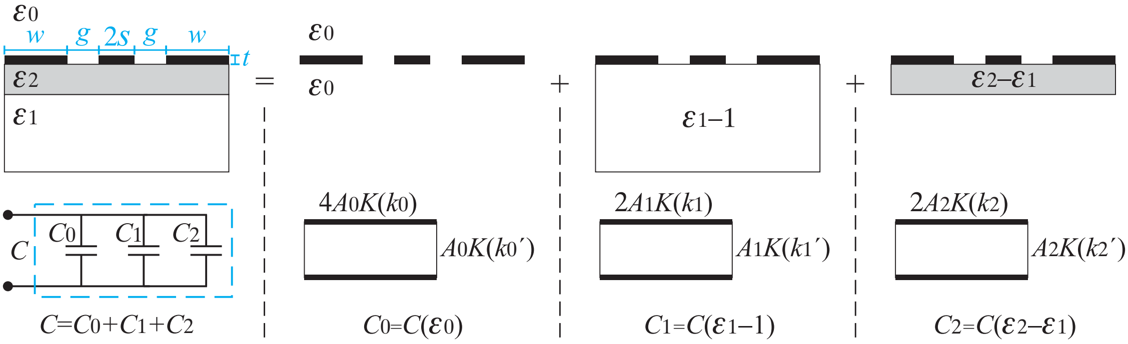

**Figure 3.8:** Parallel capacitances technique to divide the two layers structure.

The effective relative permittivity and filling factors is explained by the following:

$$\varepsilon_r' = 1 + q_1(\varepsilon_1 - 1) + q_2(\varepsilon_2 - \varepsilon_1) \tag{3.8}$$

$$q_i = \frac{1}{2} \cdot \frac{K(k_i)}{K(k_i')} \cdot \frac{K(k_0')}{K(k_0)} \quad , \quad i = 1,2 \tag{3.9}$$

- Conductance $G$:

  For the calculation of $G$ in equation 3.4, the tangent loss of the dielectric is computed by:

$$\tan(\delta_{\varepsilon_r}) = \frac{\varepsilon_r''}{\varepsilon_r'} \tag{3.10}$$

$$\varepsilon_r'' = q_1\varepsilon_1 \tan(\delta_1) + q_2(\varepsilon_2 \tan(\delta_2) - \varepsilon_1 \tan(\delta_1)) \tag{3.11}$$

  where $\tan(\delta_i)$ represents the dielectric loss of the $i$ layer and the airspace is assumed lossless [53].

- Inductance $L$ and Resistance $R$:

  The inductance $L$ and the series resistance $R$ are independent of the substrate properties. Therefore, by assuming an ideal conductor with zero resistivity $\rho$ the inductance per unit length is determined from the line capacitance $C_0'$ in the absence of dielectrics as following:

$$L = \frac{1}{c_0^2 C_0'} \tag{3.12}$$

Nonetheless, the skin depth $\delta_{skin}$ should be considered for real conductors with finite conductivity and thickness $t$ as a function of the frequency for the calculation of the inductance and resistivity. Due to the frequency dependence of the skin depth $\delta_{skin}$:

$$\delta_{skin} = \sqrt{\frac{\rho}{\pi f \mu_0 \mu_r}} \tag{3.13}$$

Three areas for the metallization are considered: $t \leq \delta_{skin}$, $\delta_{skin} < t < 3\delta_{skin}$, and $3\delta_{skin} \leq t$. The corresponding equations are documented in [29, 54].

The use of conformal mapping to calculate the partial components is made under the assumption of an infinitely thin metallization layer with $t = 0$. Therefore, for a finite metallization layer, the line width can be adjusted depending on the metallization thickness. The line geometries are corrected by the correction parameter $\Delta s$ for the effective sizes ($s_{\text{eff}}$, $g_{\text{eff}}$, and $w_{\text{eff}}$):

$$s_{\text{eff}} = s + \Delta s \quad , \quad g_{\text{eff}} = g - 2\Delta s \quad , \quad w_{\text{eff}} = w + \Delta s \tag{3.14}$$

$$\Delta s = \frac{t}{2\pi\varepsilon_e}\left[1 + \ln(\frac{4\pi w}{t})\right] \tag{3.15}$$

where $\varepsilon_e$ is the mean value of the layers permittivity.

The conformal mapping method frequency range is limited [6]. The inaccuracy of the extracted material parameter increases for frequencies below $f_{\text{min}}$ and the assumption of a quasi transverse electromagnetic propagation (quasi TEM mode) is not correct for frequencies higher than $f_{\text{max}}$ (cut-off frequency). The $f_{\text{min}}$ and $f_{\text{max}}$ are given by:

$$f_{\text{min}} = \frac{1}{4L\sqrt{\mu_0\varepsilon_0\varepsilon_{r*}}} \quad , \quad f_{\text{max}} = \frac{1}{20(g+s)\sqrt{\mu_0\varepsilon_0\varepsilon_{r*}}} \tag{3.16}$$

where $L$ is the length of the CPW and the relative permittivity $\varepsilon_{r*}$ can be estimated by the effective permittivity of the multi-layer substrate. These limitations are $f_{\text{min}} \approx 5\,\text{GHz}$ and $f_{\text{max}} \approx 40\,\text{GHz}$ for the investigation of the thick BST layer properties [28]. The BST layer parameter can be extracted by IDC for lower frequency ranges [6]. This structure can provide reliable results to about 5 GHz.

Figure 3.9 illustrates the block diagram of the analytical model of the conformal mapping method for the extraction of properties of the BST layer (relative permittivity and loss tangent) [6]. Before starting the calculation, other parameters of the structure such as the dimensions (thickness, wide, and gap) and properties (Au layer and $Al_2O_3$ substrate) need to be defined. In the first iteration, the permittivity of the BST layer is varied until the phase constants of measurement and modeling fit together. Subsequently, in the same method, the loss tangent is defined by comparison to the insertion loss of the CPW line. For the calculation of the material tunability, the S-parameters of the CPW lines are recorded in different biasing voltages and subjected to the extraction process. The tunability is obtained from the calculated relative permittivity at different electrical fields (biasing voltage/gap). In case of different structural dimensions, the distribution of the control field in the substrate can vary, resulting in different extracted values.

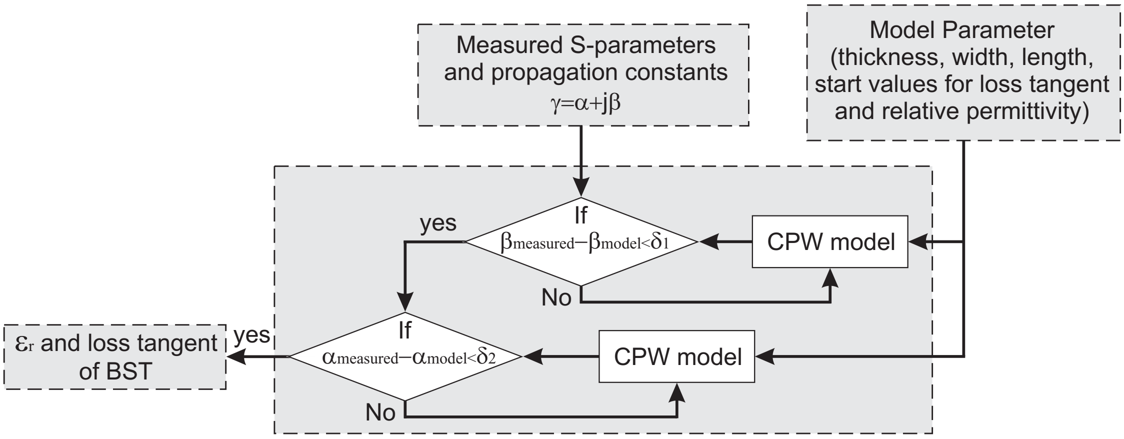

**Figure 3.9:** The block diagram of the extraction of relative permittivity and loss tangent of the BST layer from measured S-parameters.

### Electrode Layer Patterning Process

In this work, the components are mainly realized by gold electrodes. In addition to the electrical conductivity of the electrode, the chemical and mechanical stability is crucial for the choice of the electrode material. Gold is one of the metals which largely meets these requirements, but its use is only limited by the high cost of materials. Copper is therefore used in most cases. Despite having a low material cost, it has a higher electrical conductivity. However, to prevent copper corrosion, copper electrodes are covered and passivated with a protective layer of gold or other metals.

In figure 3.10, the manufacturing process of the planar components is shown with galvanization grown gold electrodes. The process was performed on top of the carrier substrate, which is covered by BST film. The $Al_2O_3$ substrate (CeramTec) is used as a carrier substrate with a height of 635 µm, relative permittivity of 10, and loss tangent of 0.0003 at 10 GHz. As shown in figure 3.10(a), the first step is thermal evaporation under a high vacuum of the seed layer as a starting metallization. Due to the poor adhesion of the gold and BST layers, adhesion promoters between the substrate and the gold layer are required. In this work, Cr/Au or Cr,Ni/Au seed layers have been used with an approximate thickness of 20 nm/60 nm. The high resistivity of the adhesion layer can be later used to resistively decouple the DC bias voltage, and the RF of the tunable capacitors [6]. The next step involves patterning the structure through positive photolithography (figure 3.10(b) and (c)). The sample was covered through the spin coating of a positive photoresist. The photoresist was then pre-baked for one minute per µm thickness at 90 °C on a hotplate. This step is crucial to wards hardening the photoresist before contacting it to the mask. For patterning the structure, precision chromium glass masks were used. All areas that should be galvanically reinforced are exposed to the light through photo structuring and are freed from positive photoresist in the subsequent development process. The intense light (ultraviolet) power, wavelength, and exposure time are crucial for the quality of the patterned structure.

The gold electrodes can now be galvanically reinforced in the open cavities. For a high accuracy of patterning, the grown gold electrode should not exceed the height of the photoresist (figure 3.10(d)). Therefore, the desired height of the electrode is critical to the photoresist and its processing. A high electroplating current can damage the photoresist during plating ($> 1$ mA/cm$^2$). To stabilize the photoresist before electroplating, it needs to be hard-baked for one minute per µm thickness at 110 °C on a hotplate.

After the electroplating process, the photoresist is completely eliminated by a solvent. In particular cases, a thin layer of the exposed photoresist remains after the development. In this case, oxygen ion etching ($O_2$ plasma) was used to clean the remained photoresist layer. In the final step, the starting metallization is removed in a two-step wet-chemical etching for the gold and adhesion layers (figure 3.10(e)). Depending on the thickness of the seed layer, the etching time should be considered to prevent undercutting. Measured conductivity of the patterned gold layer is $3.15\times10^7$ S/m, which is lower than pure gold due to the roughness of the BST film [6]. Figure 3.11 shows a structured CPW on top of the BST thick film using the presented process. The gap width is 20 µm and the line width is 30 µm.

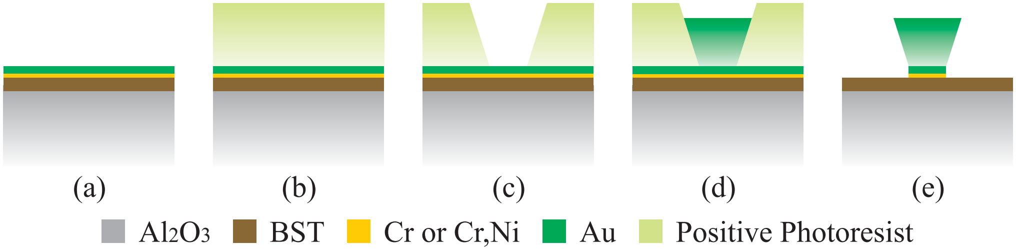

**Figure 3.10:** The structuring process of planar metallization on the thick-film BST layer by photolithography and electroplating.

## 3.3 Inkject-Printed BST Composites

This section proposes different inkjet-printed BST composites, which are developed for low-temperature sintering. Figure 3.12 observes the dependency of the printed line qual-

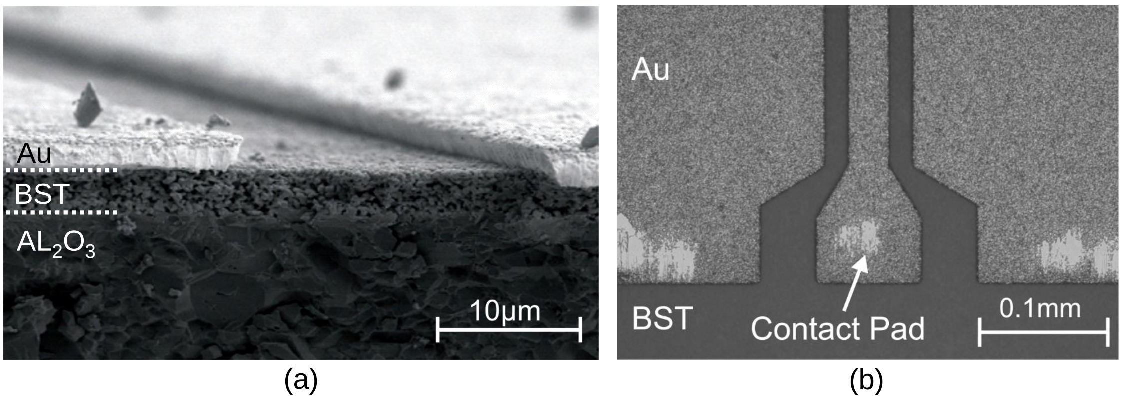

(a) (b)

**Figure 3.11:** (a) The cross section SEM image and (b) top view of structured CPW with contact pads on BST thick-film.

ity and microstructure on the sintering temperature ranges between 850 and 1200 °C, which are based on recent investigations of Friederich [28, 41] from KIT. At 1100 °C, the sintered undoped BST ink shows a porous microstructure, which is in good agreement compared to the previous screen printing experience [45]. At 1150 °C, coarse grains form due to the reaction with the alumina substrate and formation of secondary phases. This reaction is intensified by sintering the temperature and time. Due to the grains' size and BST thickness, it occurs sooner for inkjet-printed lines in comparison to the screen-printed samples [28]. For the Cu-F doped BST, a very fine microstructure is observed at a sintering temperature of 1000 °C. A slight particle size coarsening can be seen at 1050 °C and, similar to undoped BST, the reaction between BST and alumina substrate starts to intensify at higher sintering temperatures.

At low sintering temperatures, fine grained microstructure and densification of the films (high sintering activity) are observed for the BST-ZnO-$B_2O_3$ composite film. On one hand, the microstructure shows a smaller grain size (due to smaller particle size) and notably less porosity at 1100 °C compared to undoped BST films. On the other hand, the reaction with the substrate at lower temperatures occurs due to the high composite sintering activity. This reaction increases at higher temperatures.

To characterize the BST ink, this line is printed on top of the alumina substrate. Figure 3.13(a) shows the topography of the printed BST lines and CPW line patterned by photolithography and electroplating on top of the inkjet-printed BST layer. The CPW lines are characterized as shown in section 3.2. The ground-signal-ground probes (GSG) probes are contacted to CPW and the electric field is applied through the gap, penetrating into the BST layer. Figure 3.13(b), (c) and (d) illustrate the relative permittivity, loss tangent, and tunability of the BST layer over sintering temperature at 10 GHz.

The undoped BST shows the lowest relative permittivity at a low sintering temperature. By increasing the temperature up to 1200 °C, the permittivity is thus increased, which follows the development in microstructure by increasing the grain sizes. The depletion of the BST film, especially occurring at 1200 °C, is due to the reaction with alumina

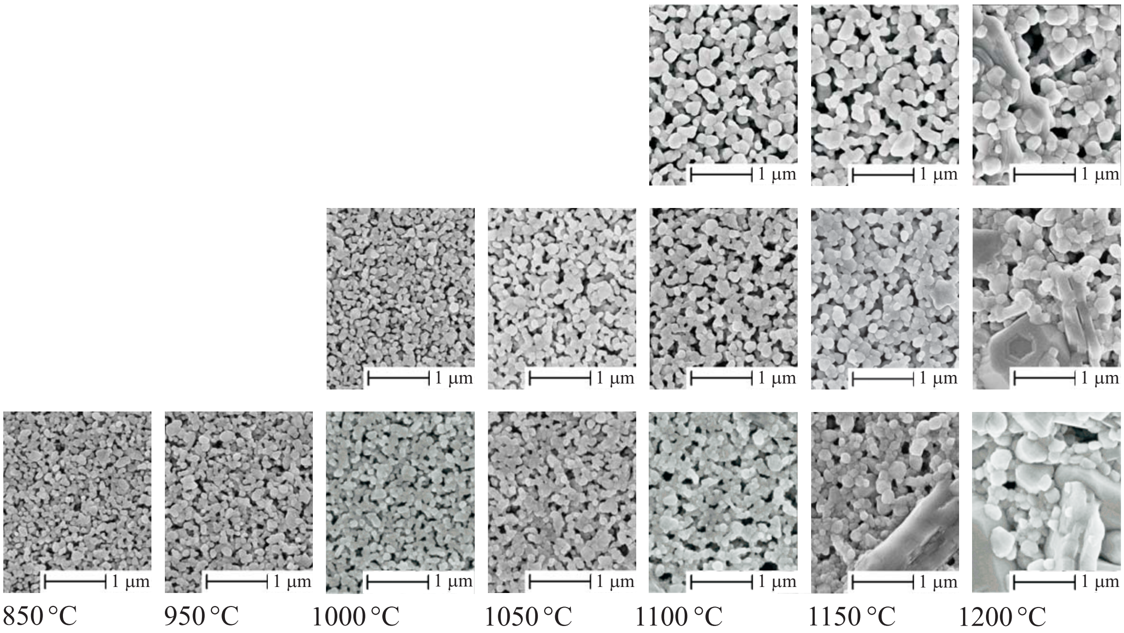

**Figure 3.12:** The microstructure of the sintered BST lines, Friederich [41], Upper row: undoped BST ink, middle row: Cu-F doped ink, lower row: BST-ZnO-$B_2O_3$ composite.

substrate [41]. The substrate reaction also results in a highly inhomogeneous structure and a significant increase in layer roughness. The measured data show a slight increase in the loss tangent with higher sintering temperatures, which is caused by higher grain sizes and can be explained by the concentration of the electrical field in the BST grains. At 1200 °C, however, severe depletion of the undoped BST layer causes the loss tangent to decrease. The tunability has been measured based on relative permittivity variations by a maximum electrical field of 10 V/μm. The maximum tunability occurs prior to the reaction with the substrate increased at 1150 °C.

For Cu-F co-doped BST, the permittivity is increased with a rising sintering temperature. The sintering temperatures of 1100 °C and 1150 °C reaches similar values as in undoped BST. For 1200 °C, however, the maximum relative permittivity was measured. The thickness for the samples with Cu-F doped BST was higher ($\approx$2.2 μm) than the other series of samples for the characterization ($\approx$1.3 μm for undoped BST). It is presumed that the influence of the interfacial reaction is reduced here, resulting in a higher relative permittivity.

As shown in figure 3.13(c), the loss tangent of Cu-F doped BST is significantly lower than the that of the undoped BST. The comparison with the undoped layers illustrates the impact of doping in this context. With an increase in the sintering temperature to 1200 °C, a slight decrease of the loss tangent is observed. It is believed that this is caused by the secondary phase formation [28].

The Cu-F doped BST shows an increase of tunability with the sintering temperature (figure 3.13(d)). Nevertheless, the measured values are slightly below those of the undoped samples. In consideration of the low insertion loss, adequate tunablity, and homogeneous structure, Cu-F doped BST sintered at 1150 °C has been identified for the development and fabrication of the planar tunable components.

The BST-ZnO-$B_2O_3$ composite film shows higher permittivity compared to other samples because of the lower porosity caused by the high sintering activity. As is the case with other samples, the maximum permittivity is measured when the first reactions with the substrate are observed [28]. The BST-ZnO-$B_2O_3$ composite and undoped BST show the same loss tangents and tunability values at 1150 °C, which is caused by the grain size effect [28].

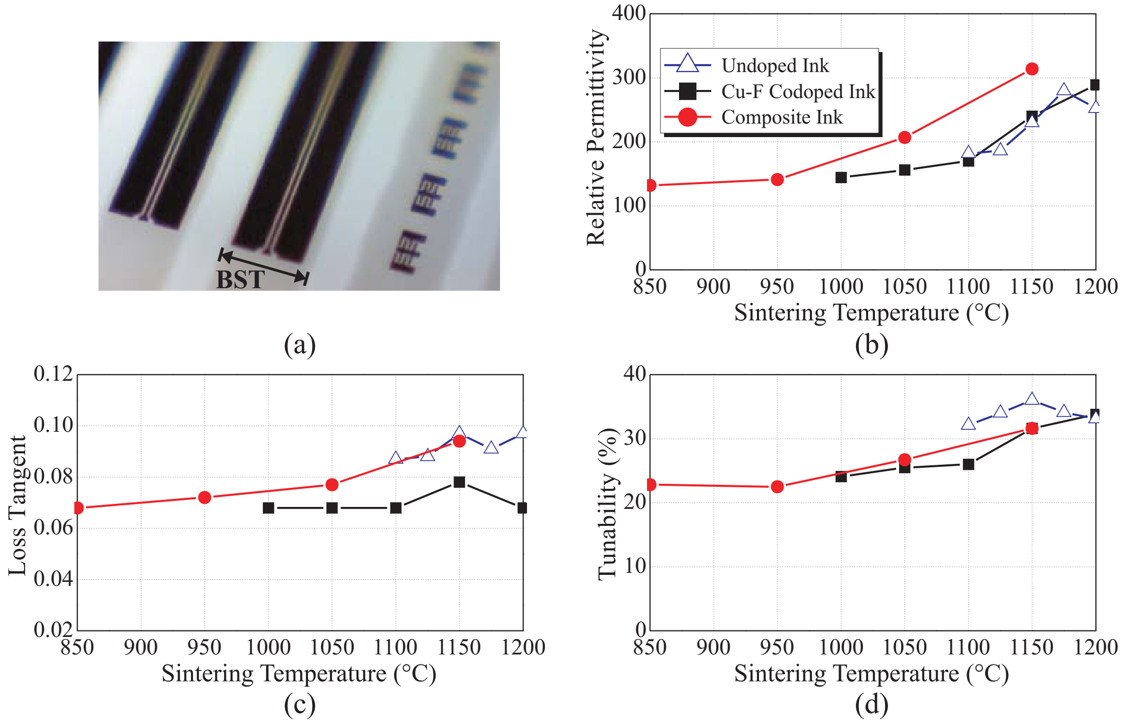

(a) (b)

(c) (d)

**Figure 3.13:** Patterned CPW on top of the inkjet-printed BST line (a). The relative permittivity (b), dielectric loss (c) and tunability under 10 V/µm (d) of the three different prepared inks at 10 GHz versus sintering temperatures.

## 3.4 Interdigital Capacitors Based on BST Thick Film

Planar microwave components, such as interdigital capacitors (IDC), coplanar wave guides (CPW), and coplanar strip lines (CPS) are suitable for planar controllable devices on BST films. The most conventional tunable components based on BST thick-films are

IDCs, fabricated on top of the BST films [10, 55]. Figure 3.14.(a) illustrates the configuration of the IDC patterned on top of a BST layer. By applying an electrical field through the IDC finger gaps, the permittivity of the BST can be altered and, as a result, the capacitance of the device is reduced [6]. Such capacitances are typically used in the planar tunable component design and the electrodes on top of the BST are fabricated by means of a photolithography process.

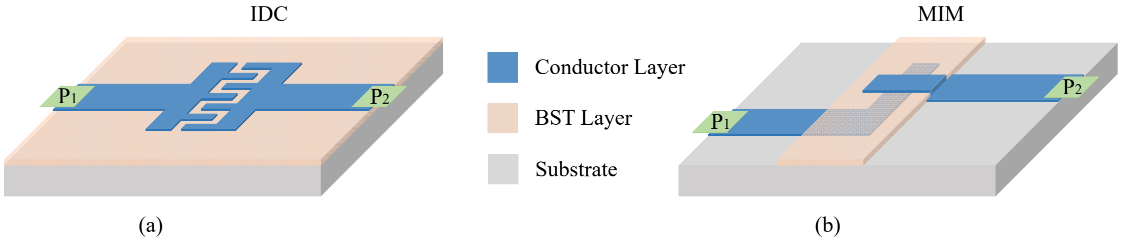

**Figure 3.14:** (a) The configuration of the IDC patterned on top of a BST layer. (b) The MIM varactor consists of three layers. The overlap area of the top and bottom electrodes define the capacitance.

An IDC varactor top view and measurement results at 12 GHz are depicted in figure 3.15. It was then fabricated on top of the inkjet-printed doped BST film and measured by on-wafer probes. Similar to the definition of permittivity tunability $\tau_\varepsilon$ in equation 2.11, the tunability of the varactor, $\tau$, is represented by:

$$\tau = \frac{C(0) - C(V_{\max})}{C(0)} \tag{3.17}$$

A capacitance of 0.28 pF was measured for an untuned state at 12 GHz. By applying 200 V through a 10 µm gap, a maximum capacitance tunability of 35% was achieved (leakage current $< 1$ nA). The minimum $Q$-factor in the untuned state is around 12. To calculate the permittivity of the material, the measured results were modeled by electromagnetic simulation in Advanced Design System (ADS) momentum. Thereby, the permittivity of the BST layers was swept to fit the measured results. The relative permittivity of the material changed from $\varepsilon_r = 200$ in the untuned state to $\varepsilon_r = 110$ in the maximum tuned state (200 V), which is in good agreement with the CPW line characterization results (figure 3.13).

## 3.5 Multilayer Varactor Based on Inkjet-Printed Thick Film

The presented IDC as a conventional tunable element in a planar structure has fabrication and performance limitations. Two main disadvantages of the tunable IDC based on BST thick film are:

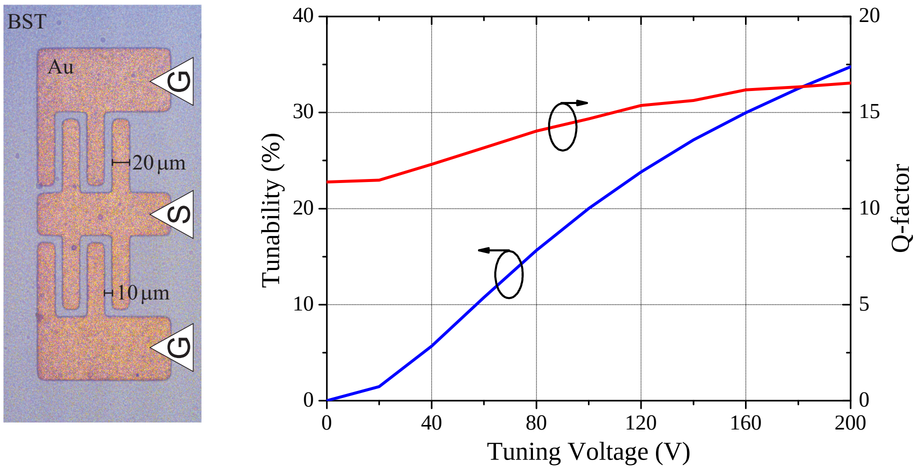

**Figure 3.15:** The top view of the fabricated IDC varactor based on Cu-F codoped BST thick film (left). Tunability and Q-factor of a measured IDC over the tuning voltage at 12 GHz (right).

- Fabrication: The photolithography process for patterning the electrode layer is a delicate and expensive procedure for structuring the tunable elements, especially for mass production.

- Biasing Voltage: Due to the technology limitations and material surface roughness, it is not possible to reduce the gap of the IDC below 8 µm. Therefore, the tuning voltage has to be raised to increase the electrical field in the gap and, therefore, the tunability. In such structures, tuning voltage reaches up to 400 V, which is not suitable for most applications. In mobile communication or portable devices, it is not easy to up convert battery voltage to 400 V for controlling. In addition, the applicable tuning voltage and, hence, the tunability is limited by the breakdown field of air if not passivated.

To reduce the biasing voltage and increase tunability of the varactor, one solution is to use metal-insulator-metal (MIM) or parallel plate capacitors instead of IDCs. This multilayer varactor is shown in figure 3.14(b), including the bottom and top layers of electrode lines which are separated by the BST layer. The intersecting area of the top and the bottom layers forms the MIM varactor. The distance between two electrodes is defined by the thickness of the BST layer that can be reduced below 1 µm. As a result, the same tunability can be achieved by applying lower tuning voltage. In addition, BST sustains higher breakdown voltage than air [29], and therefore a higher electrical field can be applied. Another advantage of the MIM capacitor is that it is possible to use the full material tunability as component tunability, however minor effects occur due to the fringe field. In conventional IDCs, it is not possible to reach more than 78% of the dielectric tunability as component tunability [29], since only a part of the tuning field is penetrating through the BST layer. Furthermore, MIM configuration can be implemented by fully printing technologies as a simple, fast, and low cost for mass production method.

The sintering of the BST thick film is necessary to make connections between the grains and obtain a mechanically stable layer. However, pure BST ceramics have a high sintering temperature ($\sim$1400 °C for bulk and $\sim$1200 °C for thick films [47]) which limits the application of pure BST. Therefore, the fabrication of multilayer structures with pure BST thick-films is only possible if using high-temperature metals [47]. In figure 3.16, micrographs of baked Au layer (thickness of 200 nm) with Cr and Cr,Ni seed layers (thickness of 20 nm) are displayed. These layers were baked between 850 °C to 1000 °C for one hour. It shows that, above 900 °C the defected layer (DL) increases. Therefore, the tunable components are limited to planar structures, which are patterned after the sintering process. As it is illustrated in figure 3.16, the Au layer grown on top of he Cr,Ni (20:80) seed layer, shows lower defected layer in comparison to Cr seed layer. Main reasons for this phenomenon are different thermal expansion and resistance to the oxidization at high temperature of Cr/Au and Cr,Ni/Au layers.

To fabricate MIM varactors and pattern conductor layers below tunable dielectrics based on commercial conductors such as gold, silver, or chromium, it is necessary to reduce the sintering temperature to 900 °C. At this temperature, it is possible to pattern conductive layers, which can sustain the sintering process. This temperature range also has a specified application in the LTCC technology, where different layers are printed on top of the green glass-ceramic tape and co-fired in a single step at 850 °C to 900 °C. Thus, one major challenge towards the fabrication of MIM varactors is the reduction of the sintering temperature of the BST layer which has been outlined in section 3.3

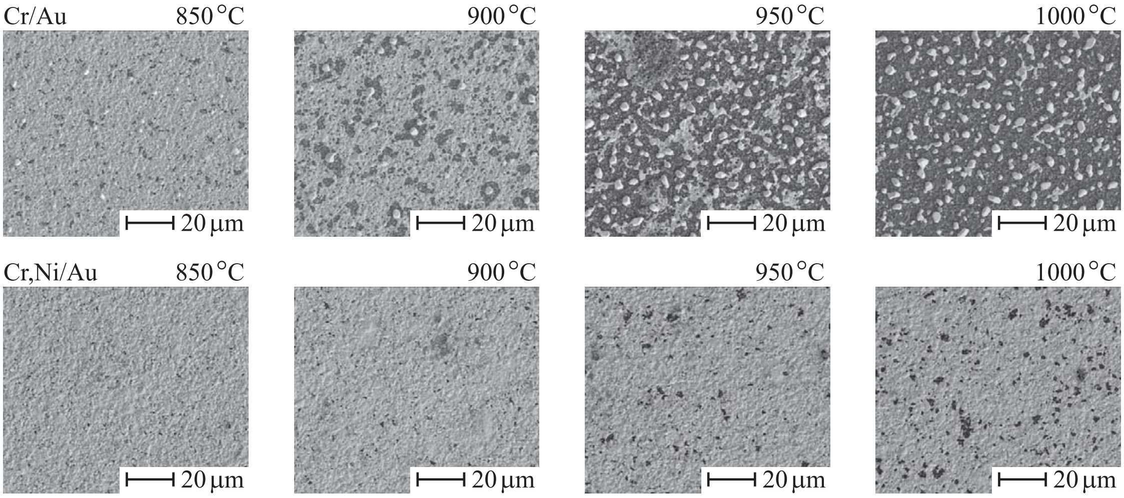

**Figure 3.16:** The Cr/Au and Cr,Ni/Au layers with 20/200 nm thickness on top of $Al_2O_3$ substrates at different temperatures for one hour.

### A. Low Voltage Tuned MIM Varactor Realization

Figure 3.18(a) shows the characterization of the MIM varactor to determine the relative permittivity and dielectric layer loss. This structure consists of the bottom Ti/Au electrode, middle BST layer, and top Cr/Au electrode. For the implementation of the varactor, a 1 µm Ti/Au electrode is evaporated on top of the $Al_2O_3$ substrate. The BST-ZnO-$B_2O_3$ ink is later printed and sintered for one hour at 850 °C with thickness of 2.3 µm. Afterwards, a 3 µm thick Cr/Au layer is patterned on the top through photolithography and electroplating. The characterized MIM varactor has a high geometric accuracy with low loss electrodes.

Figure 3.18(b) illustrates the tunability of the varactor at 10 GHz. The BST layer shows a frequency independent tunability behavior in the measured frequency range. By applying 60 V biasing voltage (26 V/µm) a tunability of 48% is achieved and, by increasing voltage to 200 V, a tunability of 75% is measured. This tunability is significantly higher at lower bias voltages compared to the reported values for IDC varactors based on BST thick film [6, 10].

### B. Equivalent Circuit Modeling

Figure A.9 shows the lumped element equivalent circuit model of the parallel plate capacitor containing a contribution from the conductor and the dielectric losses. The parasitic capacitances and resistances are negligible in the measured frequency range [56]. Also the area of the outer ring has a short circuit to the bottom electrode.

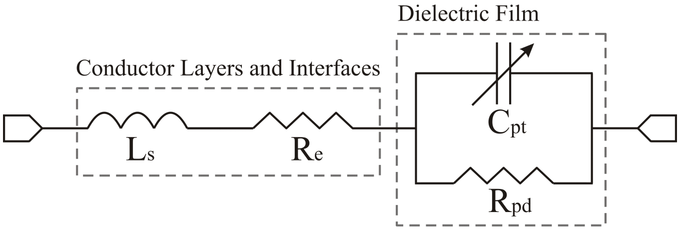

**Figure 3.17:** The simple equivalent circuit model of the MIM varactor.

The series resistance $R_e$ represents the interconnect loss from the metal-dielectric interfaces and electrodes (the intrinsic properties of the conductor layer), and $L_s$ is the parasitic inductance of the electrodes. $C_{pt}$ represents the tunable ferroelectric capacitance (the core capacitance), and $R_{pd}$ represents the resistivity of the dielectric, which is frequency dependent and includes intrinsic film properties with parallel parasitic (fringing capacitance, the electrical length inductance, measurement error). Based on the equivalent circuit in figure A.9, the total measured impedance $Z_{\text{total}}$ follows:

$$Z_{\text{total}} = j\omega L_s + R_e + R_{pd}\frac{1}{1+Q_\varepsilon^2} + \frac{Q_\varepsilon^2}{j\omega C_{pt}(1+Q_\varepsilon^2)} \tag{3.18}$$

where $Q_\varepsilon$ is the quality factor of the dielectric. By excluding the contribution of the parasitic inductance to the total impedance, the varactor's quality factor is given as:

$$\frac{1}{Q_{\text{total}}} = \tan\delta_{\text{total}} = \frac{1}{Q_e} + \frac{1}{Q_\varepsilon} \tag{3.19}$$

$$Q_\varepsilon = \frac{1}{\tan\delta_\varepsilon} = \omega R_{pd} C_{pt} \quad , \quad Q_e = \frac{1}{\tan\delta_e} = \frac{Q_\varepsilon^2}{\omega R_e C_{pt}(1+Q_\varepsilon^2)} \tag{3.20}$$

where $\tan\delta_\varepsilon$ is the dielectric loss. Figure 3.18(c) and (d) show the quality factor and capacitance of the MIM varactor based on the BST-ZnO-$B_2O_3$ films and equivalent circuit model over frequency. The varactor quality factor reduces in higher frequencies to 14.3 at 10 GHz. This behavior is typical for the varactors based on the tunable dielectric material. The capacitance is nearly frequency independent (figure 3.18(d)). The measured value for relative permittivity at 10 GHz is 130. These results match with the characterized parameters by the CPW line (figure 3.13).

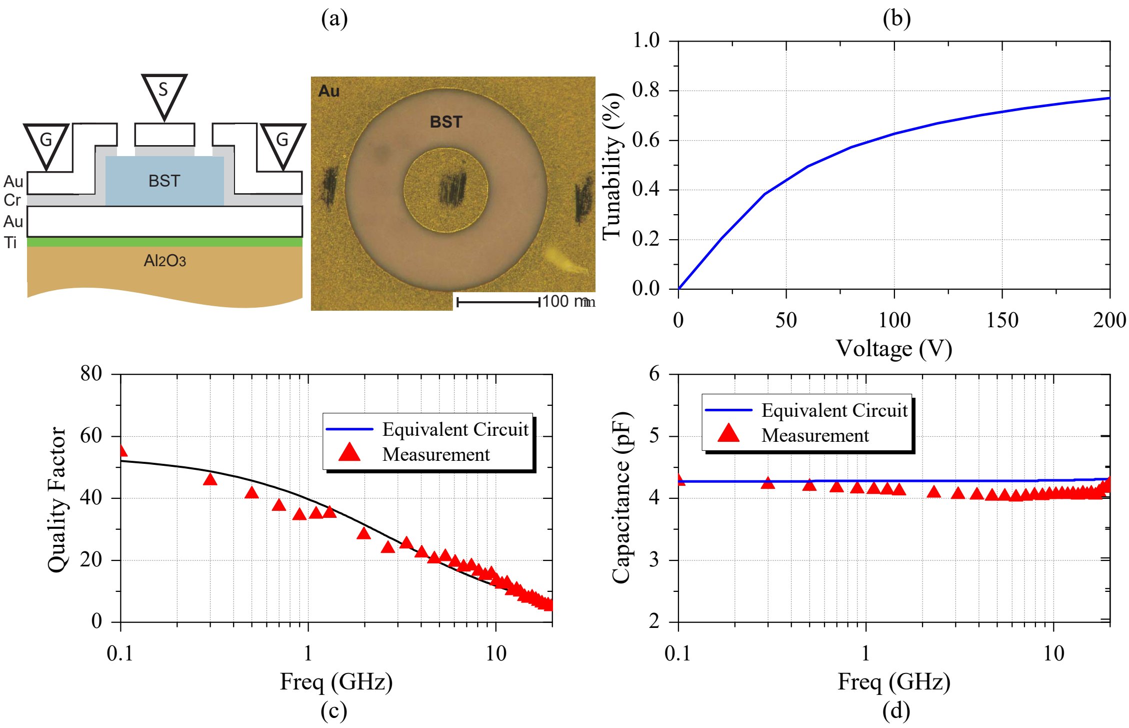

**Figure 3.18:** (a) The MIM varactor layers order and the top view, (b) The tunability of the measured MIM varactor. (c) The quality factor and (d) capacitance versus frequency of the varactor in untuned state and equivalent circuit model (figure A.9).

To implement the presented MIM varactor in tunable components, the patterning of the bottom electrode is required. The layout and equivalent circuit of the proposed MIM varactor structure (Cr,Ni/Au/BST/Cr/Au) are shown in figure 3.19. The latter consists of a tunable capacitor, the capacitor resistivity, and inductive strip lines. The MIM varactor has three layers. The bottom layer is the Cr,Ni/Au bottom electrode. Due to the sintering temperature of 850 °C, low defected layer and adhesion between the bottom electrode and the alumina substrate are critical. Therefore, the step of evaporation of a chrome-nickel/gold (20 nm / 80 nm) seed layer on the alumina carrier substrate is added to the

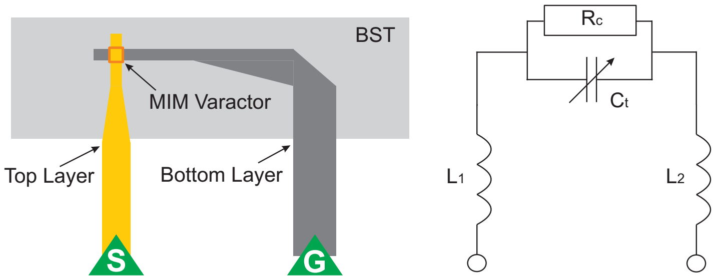

**Figure 3.19:** Layout and equivalent circuit of the MIM varactor implementing bottom Cr,Ni/Au electrode, middle BST layer and top Cr/Au electrode .

patterning process of the bottom electrode layer (figure 3.16). The Cr seed layer has lower resistivity in comparison to Cr,Ni seed layer [6]. Thus, the Cr/Au electrode is selected for pattering of the top layer and the tunable dielectric layer in the middle of the electrodes. To measure the capacitance, two lines that behave as a parasitic inductance with 350 µm gap were attached to the varactor. These lines are indicated as signal and ground lines in the figure 3.19.

The patterning of the RF electrodes is implemented by a photolithography and gold electroplating process, followed by etching of the gold seed layer. It is important for the bottom electrode to have smooth edges to reduce the surface tension and allow the BST ink to flow over the electrodes during printing, forming a homogeneous cover layer with a constant thickness [55]. Therefore, the negative photoresist with undercut structures has been used for electroplating process and the thickness of the bottom layer is limited to 1.2 µm.

In the next step, the BST layer is inkjet printed on the pre-structured alumina substrates. The BST lines with a width of approximately 300 µm and a thickness of t = 1.1 µm are printed with the process described in section 3.1.2. In the final step, top Cr/Au electrodes were patterned similarly to the bottom electrodes. Here, the thickness reached by electroplating is 3 µm. Figure 3.20 shows the topography of the fabricated MIM capacitor. The inkjet-printed BST film has a constant thickness in the MIM varactor area.

Measurements are performed using an on-wafer probe connected to the vector network analyzer (VNA, Anritsu 37397C: Anritsu, Kanagawa, Japan). Ground-source (GS) probes with 350 µm pitch were used to contact the component. The capacitance of 0.4 pF is measured for an intersection area of the top and bottom layers of $24 \times 15\,\mu\mathrm{m}^2$. A quality factor of $Q$=10 at 8 GHz is measured in an untuned state, reaching up to $Q$=12 at 50 V biasing voltage. By applying 25 V across the 1.2 µm thick BST film, a tunability of 32% is measured at 1 GHz (figure 3.20), which is increased to 46% by applying 50 V (leakage current $<$ 0.1 µA).

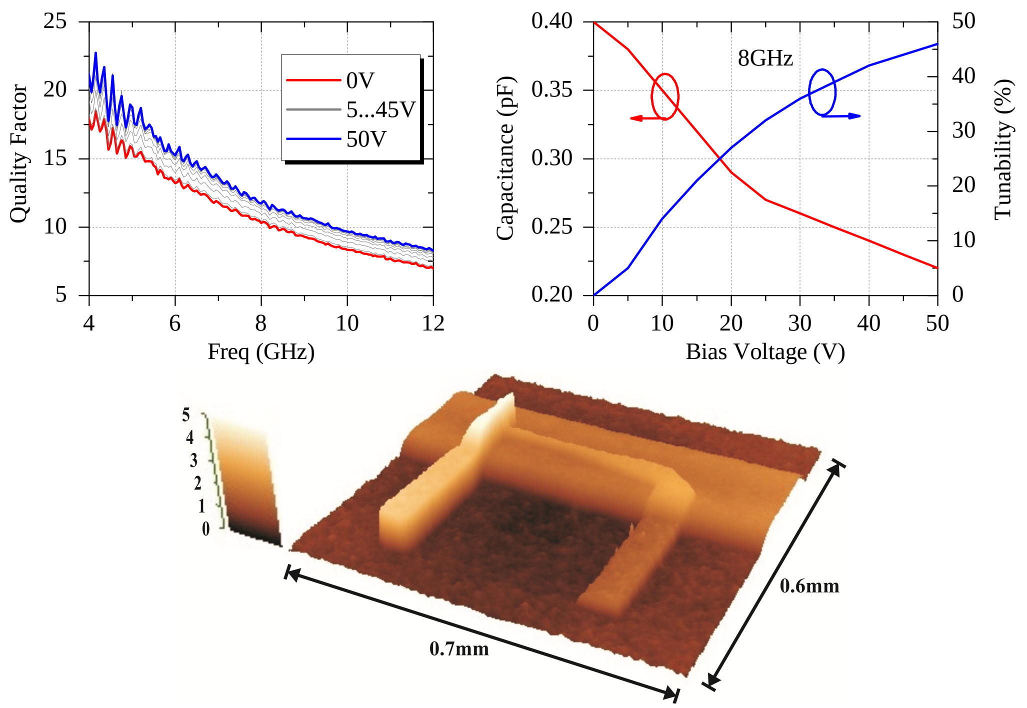

**Figure 3.20:** Characterization results and topography of the fabricated MIM varactor based on inkjet-printed BST line (measured at room temperature).

### C. Fully Inkjet-Printed MIM Varactors

To fabricate a MIM varactor, an optimized double capacitance configuration ($\pi$-topology) is selected. Figure 3.21 shows the layout of the MIM varactor and its equivalent circuit. It consists of three inductive lines and two tunable MIM capacitors in a series. The capacitors are each composed of three layers: a silver bottom electrode, a BST layer in the middle, and a silver electrode on top of the BST. The overlapped area between the top and bottom electrodes forms the capacitor. All layers are printed on an alumina carrier substrate. The main advantage of this structure is a lower sensitivity to the alignment error. The error range of the varactor capacitance and tunability are important for tunable microwave components, which can cause a mismatch and increase the insertion loss in the final results. For this reason, the alignment of the different layers on top of each other is essential. The use of this structure gives the possibility of a maximum error of $\varDelta x$ and $\varDelta y$, see Figure 3.21. Furthermore, the top electrode is only printed on top of the BST layer, therefore, the silver ink is printed on a smooth surface. The top silver layer line can be deformed, which increases fabrication tolerance, if it is printed on the step from the BST layer to the carrier substrate, as was shown in figure 3.21.

Figure 3.22 shows the photograph and the SEM cross-section view of the fabricated MIM varactor with 9 µm thickness for the BST layer and approximately 2 µm thickness of the silver electrodes (conductivity $\sigma \approx 9 \times 10^6$ S/m). The SEM cross-section shows a

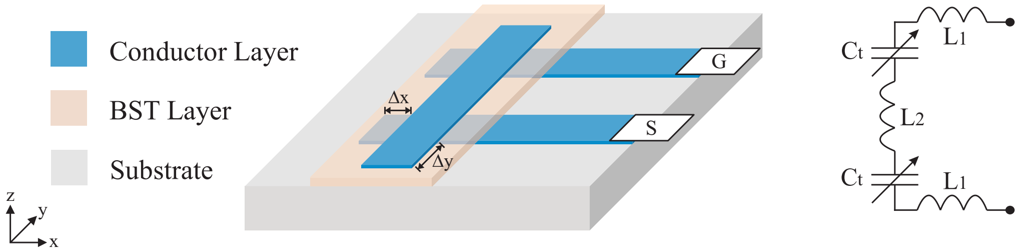

**Figure 3.21:** The equivalent circuit model and schematic order of the two series MIM varactors in $\pi$-topology based on BST composites.

homogeneous film topography of the printed BST dielectric. The electrode layers are less uniform in comparison to the BST layer. This can be explained by the smaller initial particle size and the sintering activity of the silver at 850 °C. Currently, there is no silver ink developed for sintering in this temperature range. Nonetheless, it is inferred that larger initial particle sizes can increase the uniformity of the conductor layers [43].

The MIM varactors were measured in a 50 Ω network by a 350 µm pitch GS probe. Table 3.2 summarizes the measurement and simulation results of the MIM varactor fabricated with different BST film thicknesses. The thickness of the BST layer was varied through the repeated printing and drying (50 °C) of the printed layers, resulting in heights of 3 to 9 µm. The minimum capacitance value that can be fabricated with this method is defined by the maximum BST thickness and permittivity of the material along with the width of the electrodes which are limited by the used nozzle of the print head (here 70 µm). The printing process constrains the lower limit of the line width to 100 µm. The capacitances are varied from 4.3 to 1.6 pF by using the same dimensions, however a different BST thickness. The measured quality factors at 0.5 GHz are comparable with measured quality factor for low voltage tune MIM varactor (figure 3.18(d)). The tunability of the varactors are in the range of 29 to 36%.

The simulation has been run for ideal capacitance configuration $C_i$ and fabricated configuration $C_f$ to determine the fringing effect by CST software (table 3.2). The line widths for the top and bottom electrodes are 110 µm and 130 µm. The excess length of the electrodes is 200 µm ($\varDelta x$ and $\varDelta y$ in figure 3.21). In the simulation, the BST relative permittivity $\varepsilon_r$ was set to 130. The simulation result shows an increase in the effective area of the capacitor caused by the fringing effect from increasing the thickness of the BST layer ($A_{\text{effective}}$=$A_{\text{overlap}} + A_{\text{fringing}}$). The fringing capacitor $C_{\text{fringing}}$ sees a longer distance between electrodes in comparison to an overlap capacitor $C_{\text{overlap}}$. The higher fringing effect reduces the tunability of the total capacitor ($C_{\text{effective}} = C_{\text{overlap}} + C_{\text{fringing}}$). Nevertheless, the extension length compensates for the printing error, therefore it is necessary to minimize it.

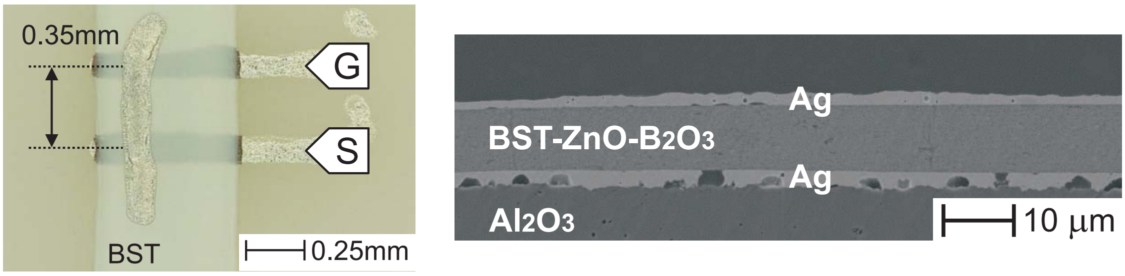

**Figure 3.22:** Topography and SEM cross-section of an inkjet-printed MIM capacitor in $\pi$ configuration.

**Table 3.2:** The measurement results of the inkjet-printed MIM varactors.

| Printing Repetition | $Q$ (0.5 GHz) | $C$ (pF) | $\tau\%$ | $h_{\text{BST}}$ (µm) | Sim $C_f$ (pF) | Sim $C_i$ (pF) |
|---|---|---|---|---|---|---|
| 1 | 35.5±1 | 4.3±0.6 | $36\pm1(50\,V)$ | 2.9±0.1 | 4.15 | 3.56 |
| 2 | 37±0.7 | 2.8±0.3 | $35\pm1(100\,V)$ | 5.6±0.1 | 2.26 | 1.9 |
| 3 | 38.5±1 | 1.6±0.2 | $29\pm1(200\,V)$ | 9±0.3 | 1.3 | 1 |

## 3.6 Fully Screen-Printed MIM Varactor

This section proposes different screen-printed BST composites developed for low-temperature sintering, which are based on recent investigations of Kohler [49] from KIT. The SEM photograph of the 900 °C sintered BST-5ZB, BST-20ZB, CuF-BST-5ZB, and CuF-BST-20ZB thick films are shown in figure 3.23. The BST-5ZB composite porosity (45%) is higher than the CuF-BST-5ZB composite porosity (33.3%). Therefore, CuF-BST-5ZB is more suitable for multi layer structures. Since the possibility of metal interconnection through the ferroelectric layer reduces. The porosity of BST-20ZB and CuF-BST-20ZB are in the same range of about 35%. When compared to BST-5ZB, the CuF-BST-5ZB has distinct sintering necks and a denser network of particles. The doped composites show higher grain sizes in comparison to the undoped composites. The formation of a low temperature melting amorphous phase results in a clustering of particles for BST-20ZB and CuF-BST-20ZB thick films, which affect the dielectric properties.

Figure 3.24 shows the SEM photograph of the 80BST-20$Mg_3B_2O_6$, and 50BST-50$Mg_3B_2$-$O_6$ sintered at 900 °C. High porosity is observed for both composites (≈45%). Due to the higher porosity and content of the dielectric phases, a reduction of the permittivity is expected in comparison to composites with a ZnO-$H_3BO_3$ additive.

The composites dielectric properties are measured by the CPW line and conformal mapping methods which were described in section 3.2. The dielectric properties' results are summarized in table 3.3 and figure 3.25. The grain sizes, porosity, and amount of ad-

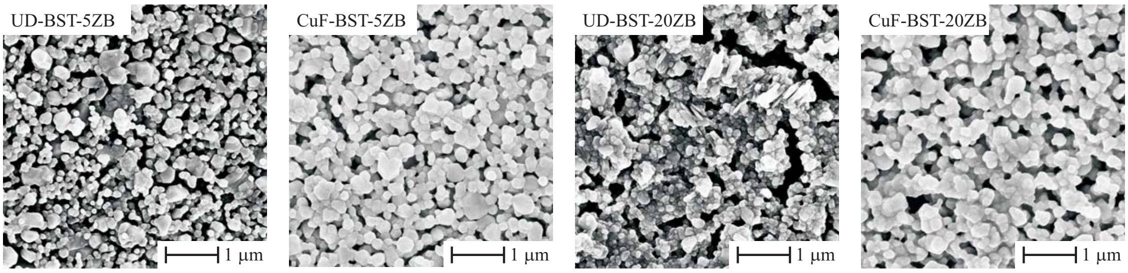

**Figure 3.23:** SEM micrographs of the 900 °C sintered BST-5ZB, BST-20ZB, CuF-BST-5ZB, and CuF-BST- 20ZB thick films, Kohler et al. [46].

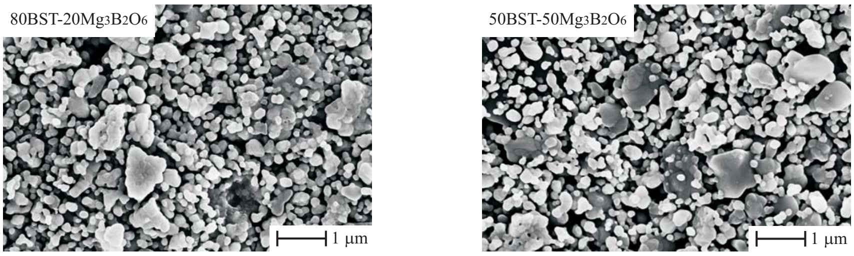

**Figure 3.24:** SEM micrographs of the 900 °C sintered BST thick films composites with addition of $Mg_3B_2O_6$, Kohler [49].

ditives influence the effective relative permittivity. On the one hand, the dissolution of barium into the amorphous phase reduces permittivity in composites with higher additive. On the other hand, due to the higher grain size, the doped BST shows a higher permittivity compared to the undoped BST composites and lower dielectric loss caused by the effect of doping.

The reduction of the insertion loss and tunability have been observed by increasing the additive to the BST powder. The ratio of grain and sintering neck size influences the tunability of BST thick film [46]. The reduction of the sintering necks and growth of the grain sizes increases the tuning field around the sintering necks, Kohler et al. [46, 47]. Therefore, the permittivity of the sintering neck becomes lower than the center of the grains. This phenomena can be explained by comparing these structures with series capacitors where the lowest capacitance has the main influence on the total capacitance.

As shown in figure 3.25(b), the Cu-F co-doped and undoped composites show similar tunability values at 10 GHz for 20% $ZnO$-$H_3BO_3$ additive. However, characterization results indicate higher tunablity for lower additive amounts in BST composites. An increase of the additive volume leads to a clustering of particles for doped as well as undoped BST thick films. This phenomena results in a lower ratio between grain and sintering neck size [46]. Based on the higher tunability and lower insertion loss of the doped composites, they are mostly used for the varactor and phase shifter processing. These composites possess adequate dielectric properties (reaching the highest tunability) and a good compromise between low porosity, homogeneous microstructure, and high sintering activity without chemical change of BST.

The 80BST-20Mg, and 50BST-50Mg composites show low permittivity and low insertion loss, which are suitable for high frequency application. Similar to the dielectric losses of BST-ZB composites, the measured losses of 80BST-20Mg thick films are increased by frequency. However, the 50BST-50Mg thick film shows a slight reduction of the dielectric loss versus frequency, which is not practically correct. This is presumably due to the low permittivity and very high porosity, which also increases the roughness of the thick film, which is increasing the characterization results error. Moreover, the tunability of the 80BST-20Mg composite is higher in comparison to the CuF-BST-20ZB composite. However, increasing the MBO additive to 50% reduces the tunability.

**Table 3.3:** Dielectric properties of low temperature sintered BST composites.

| BST Composite | Thickness (µm) | Porosity | $\tan\delta$ (10 GHz) | $\varepsilon_r$ | $\tau$ % (10 V/µm) |
|---|---|---|---|---|---|
| BST-5ZB | 6.9 | 45 | 0.065 | 155 | 26.6 |
| BST-20ZB | 5.2 | 34.8 | 0.047 | 116 | 16.4 |
| CuF-BST-5ZB | 5.6 | 33.3 | 0.062 | 206 | 28 |
| CuF-BST-20ZB | 4.8 | 35 | 0.032 | 136 | 16 |
| 80BST-20$Mg_3B_2O_6$ | 6.2 | 46.8 | 0.04 | 50 | 18 |
| 50BST-50$Mg_3B_2O_6$ | 6 | 44.3 | 0.02 | 36 | 11 |

### A. Fully Screen-Printed MIM Varactors

Based on prior analysis for the fabrication of a varactor by inkjet printing methods, $\pi$ configuration is used for screen printing, as shown in section 3.5. Within the prototyping process, three different screen meshes are developed for the three layers. The fabrication is done by the subsequent screen-printing and drying of each layer on the alumina substrate through a 325 screen mesh. As the electrode material, an LTCC compatible commercial silver paste (TC 7306 A, Heraeus GmbH, Hanau, Germany) was selected. Samples are co-fired in purified dried air at a temperature of 850 °C for one hour using a heating rate of 2 K/min.

Figure 3.26 shows the SEM cross section and top view of the fully screen-printed varactor consisting of three layers. The silver lines are thicker in comparison to the BST-5ZB layer (silver 13 µm and BST 5.9 µm). The top layer shape was changed in the cross section area due to surface roughness. The overlap area is $\approx 100\times80\,\mu m^2$. The limited wetting and a different sintering shrinkage between layers caused the holes in interfaces of the silver layers after the sintering process. Nevertheless, this phenomena prevents migration of the silver layer through the BST composites.

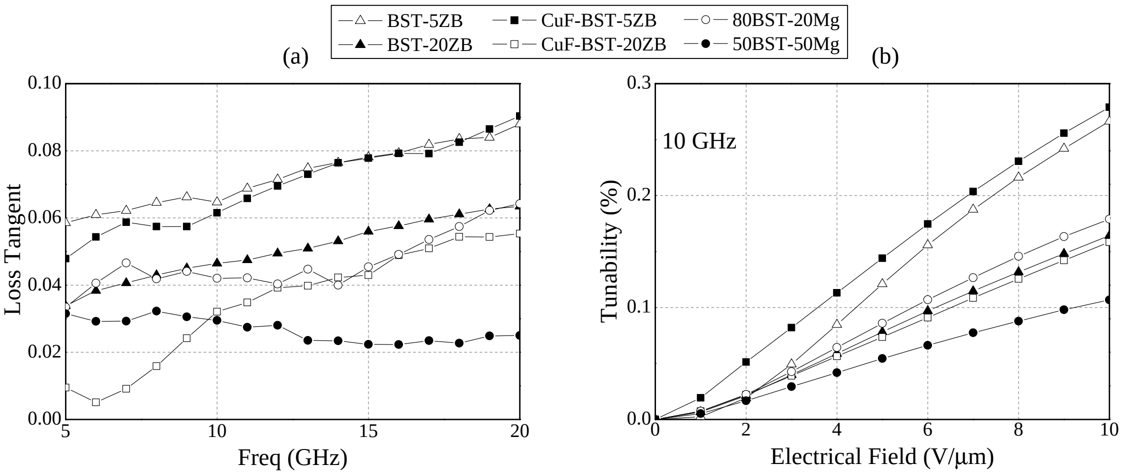

**Figure 3.25:** Characterization results of composites named BST-5ZB, BST-20ZB, CuF-BST-5ZB, CuF-BST-20ZB, 80BST-20$Mg_3B_2O_6$, and 50BST-50$Mg_3B_2O_6$: (a) Dielectric loss of untuned dielectric and (b) Tunability of the thick films versus electrical field at 10 GHz.

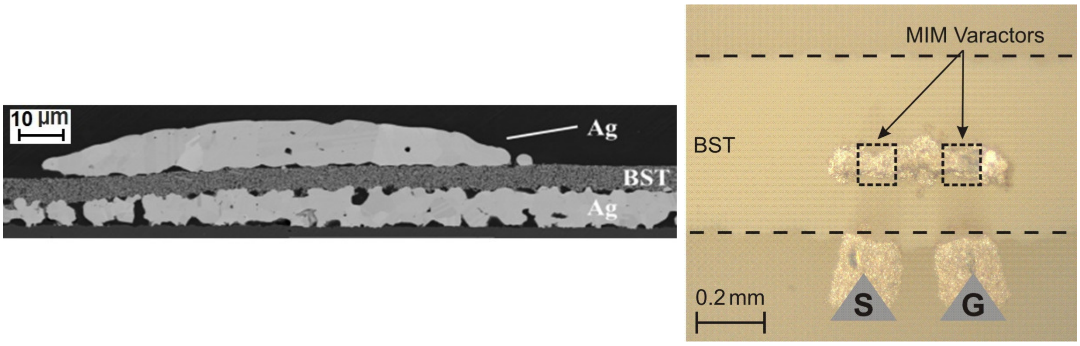

**Figure 3.26:** Topography of an screen-printed MIM capacitor in $\pi$ configuration.

The fully screen-printed varactors were contacted by GS probes and a network analyzer measured the reflection coefficient of the varactors. Table 3.4 summarizes the measurement results. The capacitances are varied from 2 to 0.15 pF by using the same mesh and dimensions but different BST composites with different relative permittivity. As is described and presented in the next chapter, the variation to small capacitance values allows a broad operation frequency range for tunable phase shifters. However, the low quality factor in higher frequencies is another parameter that limits the operation band.

A maximum applied tuning voltage of 200 V was used for tuning of the series varactors (leakage current $< 0.01$ µA). However, due to the serial connection of both capacitors the applied bias voltage of 200 V reduces the effective tuning voltage to 100 V at each varactor. The achieved capacitance tunabilities have a direct relationship with the amount of the additive in BST composites and are reduced by increasing the additive percentage.

The fully screen-printed MIM varactor based on CuF-BST-20ZB composite achieved a quality factor of 60±2 at 0.5 GHz. In comparison to the presented fully inkjet-printed

MIM varactor with a similar permittivity value (table 3.2), the quality factor of the screen-printed varactor is higher, due in part to the lower loss tangent of the BST composite and higher silver layer thickness in fully screen-printed varactors.

**Table 3.4:** Screen-printed MIM varactor measurement results.

| BST Composite | $C$ (pF) | $Q$ (5 GHz) | $\tau\%(200\,V)$ | $h_{\mathrm{BST}}$ (µm) |
|---|---|---|---|---|
| CuF-BST-5ZB | $2\pm0.2$ | $17\pm1$ | $55\pm3$ | $5.9\pm0.2$ |
| CuF-BST-20ZB | $0.9\pm0.15$ | $18\pm2$ | $33\pm2$ | $5\pm0.2$ |
| 80BST-20$Mg_3B_2O_6$ | $0.4\pm0.05$ | $33\pm3$ | $35\pm2$ | $6.2\pm0.2$ |
| 50BST-50$Mg_3B_2O_6$ | $0.15\pm0.02$ | $23\pm2$ | $11\pm1$ | $6\pm0.3$ |

# Chapter 4

# Printed and Low Voltage Tunable Phase Shifters

## 4.1 Phase Shifters in Phased Array Antenna

In this section, the performance of the phase shifters in the phased array antenna is briefly reviewed for the beam steering purpose. Figure 4.1 shows a uniform linear array equipped with phase shifters, where the antennas are equally spaced and excited with a uniform current by means of a constant phase shift between adjacent antenna elements. The phase shift $\varDelta\varphi$ for a certain value of beam steering is given by:

$$\varDelta\varphi = \frac{360\cdot s}{\lambda} \quad , \quad s = d\cdot \sin(\theta) \tag{4.1}$$

where $d$ is the distance between antenna elements, $s$ is the path difference between elements, $\theta$ is the beam steering degree and $\lambda$ is the wavelength in free space.

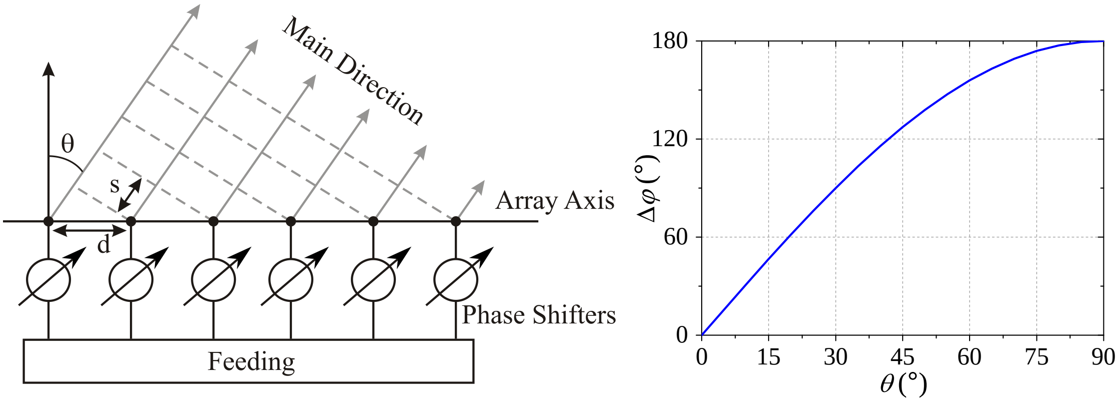

**Figure 4.1:** The schematic view of a uniform linear array (left). The beam steering degree $\theta$ versus the progressive phase shift $\varDelta\varphi$ when the distance between antenna elements $d$ is $\lambda/2$ (right).

Figure 4.1 illustrates the beam steering degree $\theta$ versus the progressive phase shift $\varDelta\varphi$ when the distance between antenna elements $d$ is $\lambda/2$. For instance, the phase shift between adjacent elements is $\varDelta\varphi = 90\,°$ for the beam steering of $\theta = 30\,°$.

In addition to the linear phased array, it is possible to place the elements in a rectangular configuration [57]. The advantage of this structure is the beam scanning in two dimensions which, in ideal scenarios without mutual coupling between radiating elements, can provide a full hemisphere area coverage. This type of antenna has a wide range of applications such as tracking and searching radars, satellite communications, etc. The far-field pattern of the phased array can be described as:

$$E_{\text{total}}(\theta,\phi) = E_{\text{single}}(\theta,\phi) \cdot AF(\theta,\phi) \tag{4.2}$$

where $E_{\text{single}}(\theta,\phi)$ is the far-field pattern of the single element and $AF(\theta,\phi)$ is the array factor of the array. The array factor is defined by different parameters such as the number of elements, phase differences, relative inter-element spacing, geometrical orientation of the elements, and relative magnitude of currents in each element. This equation can be used in any phased array with identical radiating elements, which do not necessarily have to possess the same amplitude, phase, and distances. The array factor of the planar phased array antenna can be explained as in figure 4.2. Here, a phased array has $M \times N$ numbers of cells along the $x$ and $y$ directions, respectively [57]. Based on this figure, the array factor of the planar phased array antenna can be expressed by:

$$AF(\theta,\phi) = S_x \cdot S_y \tag{4.3}$$

$$S_x = \sum_{m=1}^{M} A_m \cdot e^{j\cdot(m-1)\cdot(kd_x \sin\theta\cos\phi + \varDelta\varphi_x)} \quad , \quad S_y = \sum_{n=1}^{N} A_n \cdot e^{j\cdot(n-1)\cdot(kd_y \sin\theta\sin\phi + \varDelta\varphi_y)} \tag{4.4}$$

$$k = \frac{2\pi}{\lambda} \tag{4.5}$$

where $d_x$ and $d_y$ are the distances between elements along the x- and y-axis, $A_m$ and $A_n$ denote the elements excitation in $(M,N)$, $\varDelta\varphi_x$ and $\varDelta\varphi_y$ represent the constant phase shift between the elements in both directions, $k$ denotes the wave number and $\lambda$ is the wavelength at which the array operates. In case of a phased array with one main beam in the direction of $\theta_0$ and $\phi_0$, the phase shifts are defined as:

$$\varDelta\varphi_x = -kd_x \sin\theta_0 \cos\phi_0 \quad , \quad \varDelta\varphi_y = -kd_y \sin\theta_0 \sin\phi_0 \tag{4.6}$$

To show the beam scanning of the phased array as an example, a calculation has been formulated for a 4×4 elements planar phased array. Figure 4.2 shows the array factor of the antenna for five different phase shift values. The appearance of grating lobes in the visible range is controlled by the distance between the antenna elements. To provide

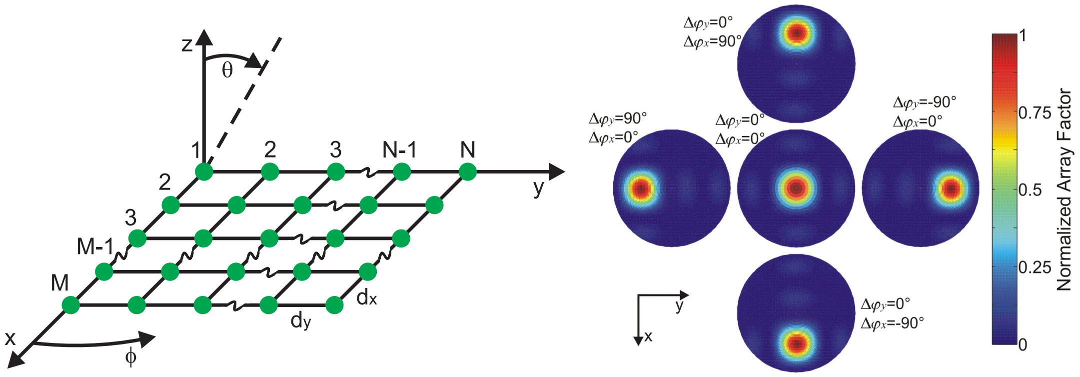

**Figure 4.2:** The planar array geometries with $M \times N$ number of cells along $x$ and $y$ directions (left). The array factor of a 4×4 elements planar phased array for five different $\varDelta\varphi_x$ and $\varDelta\varphi_y$ (right).

electronic beam scanning in any desired direction over the hemisphere and prevent grating lobes [57, 58], the distance between the antenna elements typically are between $0.5\lambda$ to $0.7\lambda$. The element excitations are exemplary $A_m$ and $A_n = 1$ and $d_x$ and $d_y$ are half of the wavelength ($0.5\lambda$). The calculation shows the beam scanning of $\pm 30\,^\circ$ in four directions for a phase difference of $90\,^\circ$ between the elements. Therefore, by implementing a phase control component in the feed of each antenna element, it is possible to control the direction of the main beam.

## 4.2 Phase Shifter Requirements

As it is explained in chapter 1, tunable phase shifters play a pivotal role in the functionality of the entire system [6, 9, 57]. The main parameters and requirements of the tunable phase shifters can be summarized as:

- 2 phase shift: To reach the maximum scanning range of the main beam, it is necessary to have a maximum phase shift of 2 for each antenna element [57, 59]. The maximum scanning range is limited by mutual coupling between radial elements, an increase in the side lobe level, and the occurrence of grating lobes [57]. The mutual coupling effects between the radiating elements increase the side lobe level, main beam squint, shifted nulls, and the array blindness points. This effect can be compensated for by increasing the distance between the radiating elements and using different types of antenna elements.

- Bandwidth and constant signal level in tuning range: The bandwidth of the entire structure (the phased array) is limited by the component with the lowest bandwidth [9]. Thus, the phase shift and insertion loss of the phase shifter over the operation frequency should be considered, which can limit the operation frequency range of the system. One main phenomenon in a phase shifter based on BST material is the reduction of the insertion loss by applying biasing voltage [6]. This phenomenon can be analyzed by the equations 4.2 and 4.3 in consideration of its consequences on the antenna radiation pattern. Figure 4.3 shows the calculated normalized power pattern of the $1\times8$ omnidirectional elements array with a $90\,^\circ$ progressive phase shift between the antenna elements for four different elements excited: Uniform, $50\%$, $75\%$, and $87\%$ linear reduction of elements excitation factor $A$ in the equation 4.4. A high variation of the elements excitation causes an increase of the main beam width and hence a reduction of the array directivity. Therefore, it is important for a phase shifter to have low variation of the insertion loss in the operation frequency range.

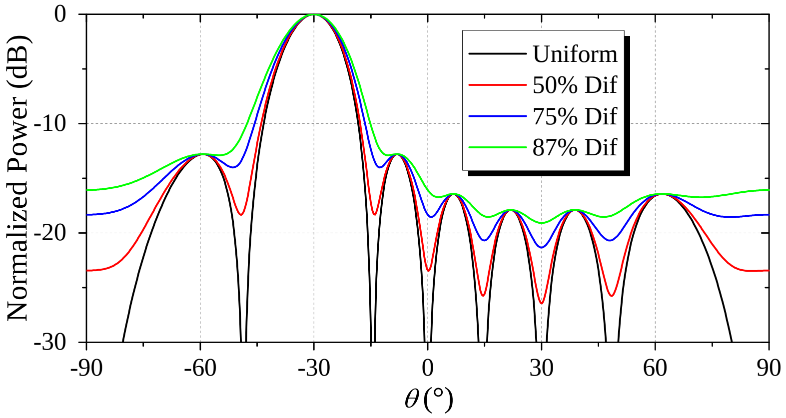

**Figure 4.3:** Normalized power pattern of a $1\times8$ omnidirectional elements array with $90\,^\circ$ progressive phase shift between antenna elements for different excited elements.

- Flexible power handling: The linearity and maximum input power of the phase shifter is a key parameter in transmit arrays, which limits the power handling capabilities of an array.
- Compactness: In a phased array antenna, the phase shifter is usually placed near the antenna. The size of the phase shifter is a critical parameter, particularly if a large number of elements is utilized, for example in a two-dimensional phased array, where the available space for the phase shifters is limited by the distance of the radiating elements (approximately $d_{x/y}$=0.5$\lambda$ to 0.7$\lambda$). Therefore the size of the phase shifter should be minimized in order to integrate it in the system. Moreover, due to the coupling and parasitic effects between radiation elements and phase shifters, it is important for the phase shifter to be compact.
- Power consumption: This is important in phased array antennas with a large number of elements. The fabrication technology of the tunable components and efficiency of the tunable varactors play a significant role in this case.
- Production cost: In a phased array antenna, tunable phase shifters affect the production cost of the entire system. The cost factor of the final product is dominated

by the phase shifters' complexity and applied technologies of the tunable components [6]. Since phase shifters are estimated to cause a great part of the total phased array cost, the large number of necessary elements can lead to unacceptable system costs for commercial applications.

The integration of the phase shifter with other components of the phased array antenna has to be considered, which can significantly reduce the final product size, complexity, and cost. Integration reduces the fabrication steps, such as soldering and mounting SMD elements or ICs to the system. The mounting of elements needs pads for connection to the circuit, which increase the size of the entire system. Moreover, the integrated circuit reduces the parasitic effects and makes it possible for the entire system to be designed at once.

- Control speed: The speed of the antenna beam scanning is a crucial parameter in on-the-move or tracking applications. The implementation technology of the tunable phase shifter defines the maximum switching time. In ferroelectric materials, the switching time is in the range of µs [10].
- Phase shift stability: The influence of the environmental parameters on the phase shifter has to be considered. Such a dependence is an integral point, particularly in harsh environments like space applications, where the temperature fluctuates dramatically.
- Insertion loss (IL): The loss of the phase shifter can be compensated by additional amplifiers in the up- and down-link, yet these will increase the power consumption, noise, and thermal loss of the entire system. Moreover, phase shifter insertion loss decreases the gain of the phased array antenna. Therefore, it is preferred to have low loss for the phase shifter elements.

**Figure of Merit (FoM)**

To evaluate the overall performance of the phase shifter, the parameter FoM, which is defined as:

$$\text{FoM} = \frac{\mathit{\Delta}\varphi_{\text{max}}}{IL_{\text{max}}} \tag{4.7}$$

$$\mathit{\Delta}\varphi_{\text{max}} = \angle S_{21}(E_2) - \angle S_{21}(E_1) \tag{4.8}$$

is used [2, 60]. $\mathit{\Delta}\varphi_{\text{max}}$ is the maximum differential phase shift and $IL_{\text{max}}$ is the maximum insertion loss of the phase shifter. It is ideal to have a maximum FoM in the operation frequency range [35]. For the phase shifters based on ferroelectric material with lossless non-tunable elements, the FoM of the phase shifter depends on the FoM of the varactor and can be defined below the transmission line cut-off frequency:

$$\text{FoM} = m(\mathit{\Delta}\phi_{\text{max}}) \cdot \sqrt{K} \tag{4.9}$$

where $m(\varDelta\phi_{\max})$ represents a coefficient dependent on the phase shift ($m(\varDelta\phi_{\max}) = 6.6$ for $\varDelta\phi_{\max} = 180°$) [60], $K$ is the varactor commutation quality factor and is defined as [61]:

$$K = \frac{C(0)}{C(V_{\max})} \cdot Q(0) \cdot Q(V_{\max}) \cdot \tau^2 \tag{4.10}$$

where $C(V)$ is the capacitance and $Q(V)$ is the quality factor of the varactor under the biasing voltage of $V$.

Figure 4.4 shows the FoM versus tunability of the phase shifter with ferroelectric varactors. The quality factor of the varactor varies from 10 to 50 for an exemplary phase shift of 180°. This result shows the FoM of 63 °/dB for a quality factor of 10 and 60% varactor tunability. The FoM remains the same when the quality factor is increased to 20 with a decreased varactor tunability of 37%. On the one hand, a tunability of more than 50% makes it difficult to match the impedance of the phase shifter over the operation frequency range. Contrarily, the number of the unit cells need to be increased to achieve a high phase shift with low varactor tunability and, as a result, affects the size of the phase shifter. Therefore, depending on the application, these parameters (tunability and quality factor) need to be adjusted. In practice, the high-tunability varactors have low quality factor in comparison to the low-tunability varactors based on BST composites [6, 62].

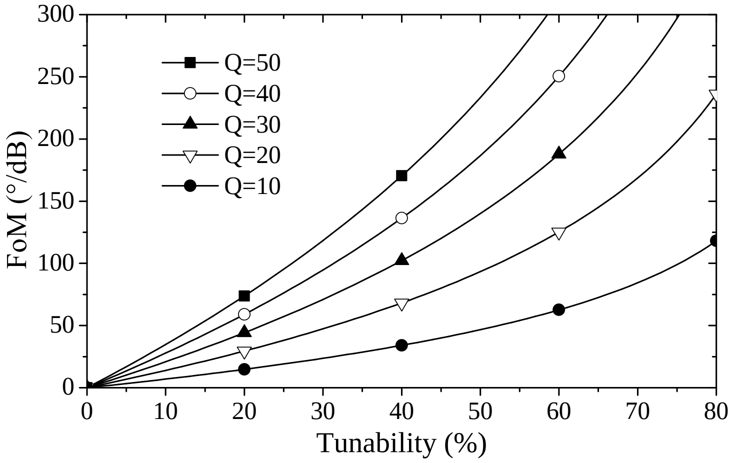

**Figure 4.4:** The FoM versus tunability of the phase shifter based on ferroelectric varactor with different quality factor for exemplary phase shift of 180 °.

## 4.3 Properties of Right- and Left-Handed Line Phase Shifters

There are different design approaches for tunable phase shifters based on BST material: loaded line, reflection type, and all pass filter topology. The loaded line or traveling wave tunable phase shifter is one of the most interesting structures which is investigated based on ferroelectric materials [6, 10]. In these structures, the transmission line is loaded with BST material and the phase constant is varied by changing the permittivity of the tunable dielectric [35]. However, due to the high permittivity of the material, matching of the phase shifters is difficult. A solution to this problem is a transmission line periodically loaded with varactors, which has a linear phase frequency dependence with a substantial change in the differential phase shift in the operation frequency range [10]. In such a structure, the varactors are controlled by a biasing voltage. As a signal propagates through the transmission line, each new section acts electrically as a small lumped circuit element. In comparison to the other structures, the loaded line phase shifters offer a compact size and the phase shift can be easily extended by increasing the number of unit cells [35].

The delay time or phase shift, insertion loss, and size are key parameters of the loaded line phase shifters. Considerable efforts have been made to investigate phase shifter concepts that can benefit from the advantages of the screen printing technology [10, 35]. There are two main categories of circuitry concepts: conventional right hand transmission line (RH-TL) and composite right-/left-handed transmission line (CRLH-TL). In the following section, the equivalent circuit and phase shift calculation of both transmission lines are presented and discussed.

### A. Basic Theory of a Right-handed Transmission Line

The conventional RH-TL is represented by a series inductor and a shunt capacitance, implying the use of a low pass topology. The equivalent circuit of a transmission line has just an inductance per unit length $L$ and a capacitance per unit length $C$ for a lossless circuit. As depicted figure 4.5, these elements are distributed uniformly along the line for a single unit cell with the period of the unit cell $\kappa$.

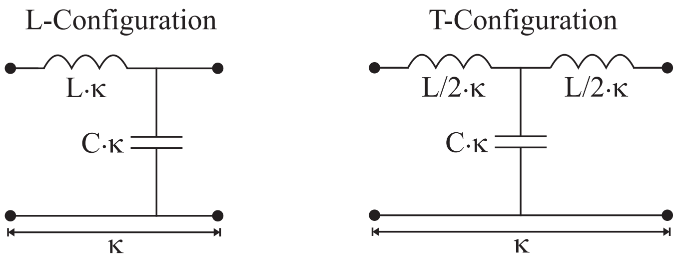

**Figure 4.5:** L- and T-configurations equivalent circuit model of a lossless right-handed transmission line.

These two circuit elements, normalized per unit length, can be used to describe the high frequency properties of a transmission line. When the equivalent circuit equation is solved, the characteristic impedance $Z$ and propagation constant $\gamma$ for L-configurations are modified to:

$$Z = \sqrt{\frac{L}{C}} \quad , \quad \gamma = \alpha + j\beta \tag{4.11}$$

where is the attenuation constant and $\beta$ is the phase constant. For a lossless transmission ($\alpha = 0$), the phase velocity and propagation constant are defined by:

$$\nu = \frac{\omega}{\beta} = \frac{1}{\sqrt{LC}} \quad , \quad \gamma = j\omega\sqrt{LC} \tag{4.12}$$

Altering the capacitance of the transmission line from $C_1$ to $C_2$ ($\Delta\beta = \beta(C_1) - \beta(C_2)$) changes the phase constant. The phase shift $\Delta\varphi$ is defined by:

$$\Delta\varphi = \frac{180\,^\circ}{\pi}\Delta\beta \cdot \kappa \cdot n \quad , \quad \Delta\beta = \omega\sqrt{LC_1} \cdot (1 - \sqrt{1-\tau}) \tag{4.13}$$

where $n$ represents the number of transmission line unit cells and $\tau$ is the capacitance tunability ($\tau = (C_1$-$C_2)/C_1$). Considering the T-configuration of the right-handed transmission line, the phase velocity and cut-off or corner frequency can be calculated as follows [63]:

$$\nu = \frac{\omega\kappa}{\cos^{-1}(1 - \frac{LC(\omega\kappa)^2}{2})} \quad , \quad f_c = \frac{1}{\pi\sqrt{LC}} \tag{4.14}$$

The maximum phase shift is at the first cut-off frequency ($f_{c1}$). Because of the high insertion and return losses near $f_{c1}$, the FoM reduces at this frequency (equation 4.7) and therefore, it is not possible to operate at cut-off frequency. Typically, the operation frequency is lower than the cut-off frequency, where the FoM is higher, which is a trade-off between maximum phase shift and insertion loss. The operation frequency is usually around 25 to 50% lower than the cut-off frequency [35], which shows better port matching for the phase shifter.

Conventional networks use $50\,\Omega$ as the matching impedance. By calculating the line impedance $Z$ and cut-off frequency $f_c$, it is possible to draw a relationship between line impedance and capacitor values. Figure 4.6 shows the values of the capacitance and inductance for the $50\,\Omega$ transmission line versus cut-off frequency. These values can be used for the design of the tunable phase shifter based on a right-handed transmission line.

The line impedance is changed by different values of the capacitance and a fixed value for the inductance. This variation affects the return loss of the phase shifter. Therefore, for a phase shifter based on a varactor, it is not possible to be matched with a constant impedance over the entire tuning state. In order to achieve acceptable return loss, the phase shifter is designed to have the best matching in the center tuning point of the varactors ($[C(E_1)$+$C(E_2)]$/2).

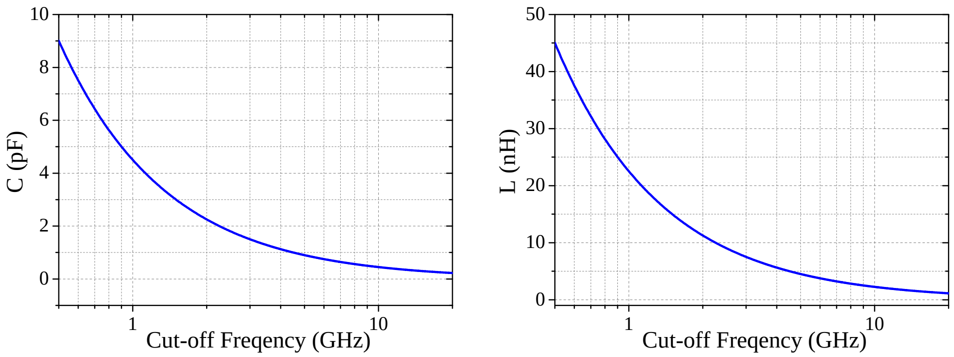

**Figure 4.6:** Calculated inductance and capacitance for T-configuration in 50 Ω transmission line.

To demonstrate the functionality of the loaded line structure as a phase shifter, a 3-unit cell right-handed transmission line is simulated with 50% tunability of $C$ by selecting a cut-off frequency at 8 GHz. The parameters of the 50 Ω transmission line are obtained: $C = 0.56$ pF, $L = 2.8$ nH. To have low return loss in tuning states, the obtained capacitance value is placed in the middle of the capacitance tuning range ($C = 0.74 \sim 0.37$ pF). Figure 4.7 shows the S-parameter and propagation constant in different tuning states. The transmission line shows the behavior of a low pass filter. The highest achievable return loss is at $C = 0.56$ pF. It can be observed that, by reducing the value of the capacitance, the band pass shifts to higher frequencies and the phase constant is reduced. By employing this feature, the loaded transmission line can be used as a tunable phase shifter with adapting the value of the capacitor $C$.

### B. Basic Theory of a Composite Right-/Left-Handed (CRLH)

By interchanging the position of the inductor and capacitor in the RH-TL, the resulting structure is referred to as a left-handed transmission line (LH-TL), or one-dimensional version of the meta materials with a high pass configuration. The direction of the phase velocity and group velocity are opposite each other in a LH-TL. The ideal LH-TL is not possible to be implemented because of the parasitic effect of the transmission line. Therefore, CRLH-TL has to be used, which substitutes the parasitic inductors and capacitors. The CRHL-TL is a chain of cascaded band pass unit cells. It can achieve an equivalently zero or negative propagation constant. The ideal equivalent circuit for a lossless CRLH-TL is shown in figure 4.8 in L- and -configurations with the period of the unit cell $\kappa$. These components describe the left-handed waveguide with $C_L$ and $L_R$ connected to the two gates in the series and $L_L$ in parallel to $C_R$ connected to the ground.

These four circuit elements, normalized per unit length, can be used to describe the high frequency properties of a CRLH transmission line. When the equivalent circuit equation is solved in the frequency domain, the characteristic impedance for L-configurations is modified to:

$$Z_{TL} = \sqrt{\frac{Z(\omega)}{Y(\omega)}} \quad , \quad \gamma = \alpha + j\beta = \sqrt{Z(\omega) \cdot Y(\omega)} \tag{4.15}$$

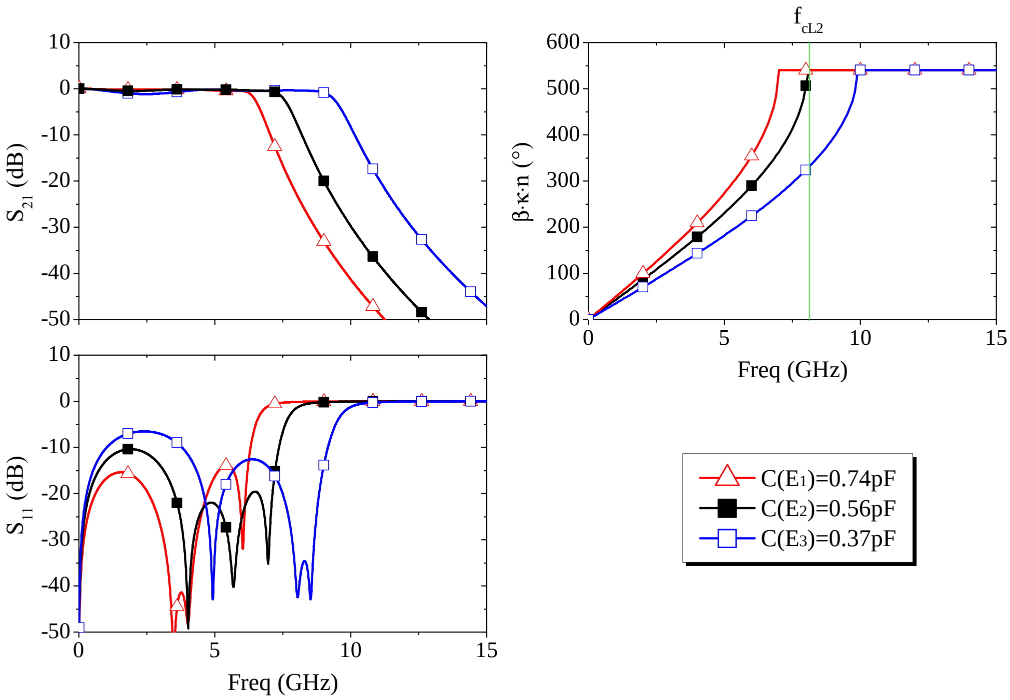

**Figure 4.7:** S-parameters and propagation constants for 3-unit cell discrete transmission line for RH-TL for different parallel capacitance values.

where:

$$Z(\omega) = j \cdot (\omega L_R - \frac{1}{\omega C_L}) \quad , \quad Y(\omega) = j \cdot (\omega C_R - \frac{1}{\omega L_L}) \tag{4.16}$$

and the series and shunt resonance frequencies:

$$\omega_{se} = \frac{1}{\sqrt{L_R C_L}} \quad , \quad \omega_{sh} = \frac{1}{\sqrt{L_L C_R}} \tag{4.17}$$

Therefore $\beta$ is:

$$\beta = s(\omega) \cdot \sqrt{\omega^2 L_R C_R + \frac{1}{\omega^2 C_L L_L} - (\frac{L_R}{L_L} + \frac{C_R}{C_L})} \tag{4.18}$$

$$s(\omega) = \begin{cases} -1, & if \quad \omega < \min(\omega_{se}, \omega_{sh}) \\ +1, & if \quad \omega > \max(\omega_{se}, \omega_{sh}) \end{cases} \tag{4.19}$$

Figure 4.9 shows the phase constant of the CRLH-TL. In an unbalanced circuit, there is a stop-band between the resonance frequencies. The phase constant is an imaginary number and causes the real propagation constant in the stop-band. As a result, the signal on the line is attenuated. For a balanced circuit or no stop-band transmission line, the transition frequency is identical to $\omega_0 = \omega_{se} = \omega_{sh}$, if: $L_L C_R = L_R C_L$.

The characteristic impedance for a CRLH-TL in a balanced circuit is obtained by:

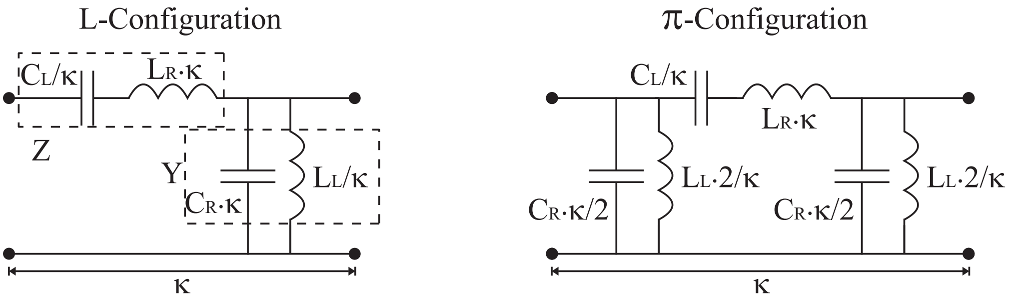

**Figure 4.8:** Equivalent circuit model of a lossless conventional CRLH transmission line unit cell in L- and -configurations.

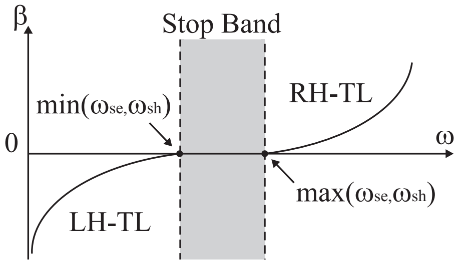

**Figure 4.9:** Graphic representation of the dispersion equations for a CRLH-TL.

$$Z = \sqrt{\frac{L_R}{C_R}} = \sqrt{\frac{L_L}{C_L}} \tag{4.20}$$

For a lossless transmission, the phase velocity is define by $\beta$:

$$\nu = \frac{\omega}{\beta} = \frac{1}{s(\omega) \cdot \sqrt{(L_R - \frac{1}{\omega^2 C_L})(C_R - \frac{1}{\omega^2 L_L})}} \tag{4.21}$$

Considering the -configuration of the composite right hand transmission line, the phase velocity can be calculated as follows [63]:

$$\nu = \frac{\omega\kappa}{\cos^{-1}(1 - \frac{1}{2}(\frac{\kappa^2}{\omega^2 L_L C_L} + \kappa^2 \omega^2 L_R C_R - (\frac{L_R}{L_L} + \frac{C_R}{C_L})))} \tag{4.22}$$

Moreover, the cut-off frequencies limit the bandwidth of the transmission line. The right- and left-handed cut-off frequencies can be calculated as:

$$f_{cL} = \frac{\sqrt{a_1 - \sqrt{a_1^2 - a_2}}}{2\pi} \quad , \quad f_{cR} = \frac{\sqrt{a_1 + \sqrt{a_1^2 - a_2}}}{2\pi} \tag{4.23}$$

$$a_1 = \frac{1}{2L_RC_L} + \frac{1}{2L_LC_R} + \frac{2}{L_RC_R} \quad , \quad a_2 = \frac{1}{L_RC_RL_LC_L} \tag{4.24}$$

For the design of the phase shifter with the defined cut-off frequencies ($f_{cL}$ and $f_{cR}$) and line impedance $Z$ [64], the $C_R$, $L_R$, $C_L$, and $L_L$ values are given by:

$$C_R = \frac{1}{\pi Z(f_{cR} - f_{cL})} \quad , \quad L_R = C_RZ^2 \tag{4.25}$$

$$C_L = \frac{C_R}{(\pi ZC_R(f_{cR} + f_{cL}))^2 - 1} \quad , \quad L_L = C_LZ^2 \tag{4.26}$$

To demonstrate the functionality of the left-handed line structure, a 3-unit cell CRLH transmission line in -configuration is simulated with 50% tunability of $C_L$. By selecting cut-off frequencies of 4 and 11 GHz, the parameters of the 50 Ω transmission line are obtained: $C_L = 0.25$ pF, $L_L = 0.63$ nH, $C_R = 0.9$ pF, $L_R = 2.27$ nH. If $C_L$ is tuned, the transmission line impedance changes affect the return loss of the phase shifter. Therefore, to minimize variation of the line impedance from 50 Ω, the obtained capacitor is placed in the middle of the capacitance tuning range ($C_L = 0.33 \sim 0.16$ pF). Figure 4.10 shows the S-parameter and propagation constant in different tuning stages, with the highest achievable return loss of $C_L = 0.25$ pF. Moreover, it shows that, by replacing the varactor instead of $C_L$, the propagation constant can be changed and the phase shift is achieved.

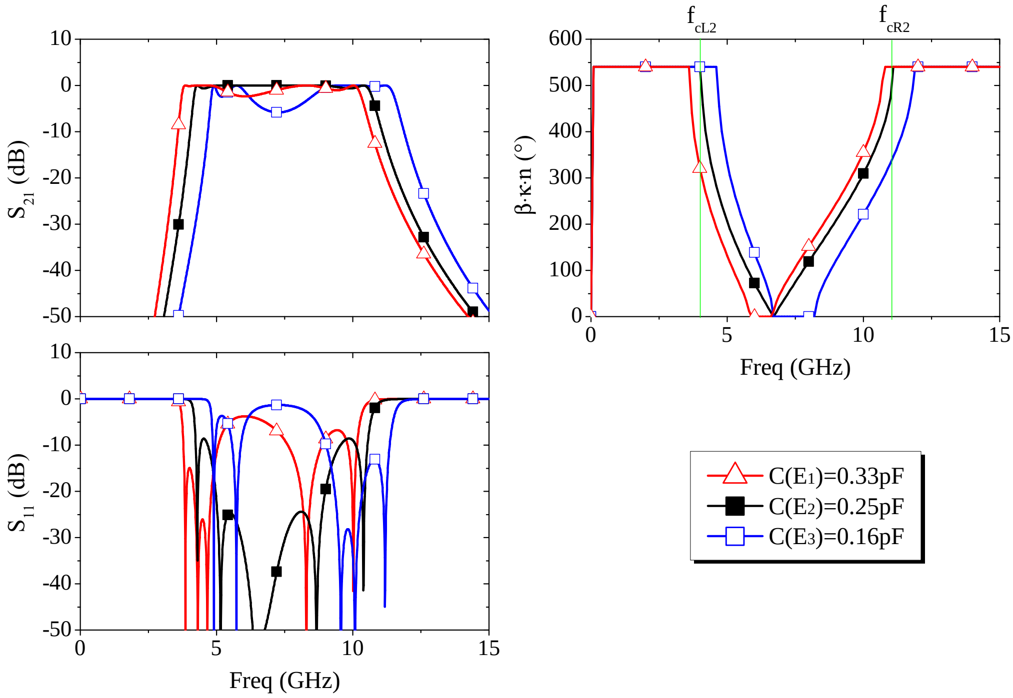

**Figure 4.10:** S-parameters and propagation constants for a 3-unit cell discrete CRLH-TL for different series capacitor values.

## 4.4 Prototype of a Left-Handed Phase Shifter in a Microstrip Line Environment

One of the options to reduce the size of the phase shifter is to use a left-handed line concept [24, 65, 66]. Artificial electromagnetic materials, with negative permittivity and permeability in the defined frequency range, have gained considerable attention in recent years. Artificially synthesized left-handed waveguides (metamaterial) can be used as compact tunable phase shifters. They have two main advantages in comparison to conventional right-handed transmission lines:

- In the left-handed circuit, the value of the capacitors are reduced in tuning states. The cut-off frequency shifts to higher operation frequencies and therefore insertion loss increases. Also, in the BST thick film material, the lowest quality factor occurs in an untuned state, as shown in chapter 3. These two phenomena compensate for one another and, as a result, the insertion loss is constant throughout the operation frequency in different tuning states [6].
- The tunable varactors form a series in the left-handed transmission lines. Therefore, in comparison to a right-handed transmission line which has series inductors, LH-TL is shorter and have high phase shift per unit area [66], which is resulting in more compactness in size.

There is different advantages and disadvantages between the RH-TL and CRLH-TL configurations, which depend on the application, frequency range, and implementation technology. The RH-TL configuration has simple structure, broad operation bandwidth, low insertion Loss, and high frequency operation range (Ku-band and above). But it shows relatively large footprint. On the other hand, The CRLH-TL configuration has compact structure with high phase shift and FoM per unit area under low insertion loss variations. but it has limited operation bandwidth and is sensitive to parameter variation

In this section, developed structure of the left-handed phase shifters, in microstrip environment, based on screen printed BST thick film in the recent investigation of Sazegar [6] is used. It shows a compact phase shifter at 10 GHz which was implemented in linear array. Based on the principle design of Sazegar [6], the topology and several key parameters, such as unit cell order and IDC varactors, have been further specifically investigated and optimized for inkjet printing technology. This work presenting the developed design, by Nikfalazar et al. [67], based on inkjet printed BST lines for integration in to the planar array at 12 GHz. As it will be shown in the next chapter, the use of the selective printing such as inkjet printing reduces extra loss for non-tunable components in the phased array antenna.

The left-handed circuit can be artificially implemented with special topologies on dielectric materials. Figure 4.11(a) shows the schematic of the proposed 7-unit cell left-handed phase shifter based on a unit cell configuration (figure 4.8). It consists of series varactors and parallel inductance lines. The parasitic inductance line, with the width $W_3$ and length $L_3$, connect parallel inductance lines to the ground in both sides (figure 4.11). These lines have an influence on the bandwidth of the transmission line, which should be minimized.

To apply a control voltage to the varactors simply, the phase shifter ports have to be RF isolated DC feeds, which is impossible to implement in a unit cell configuration (figure 4.11(a)). Thus, to simplify the biasing concept, a second structure is presented in figure 4.11(b). In this case, the grounds on both sides of the phase shifter are RF isolated DC feeds and can be used for the biasing of the varactors.

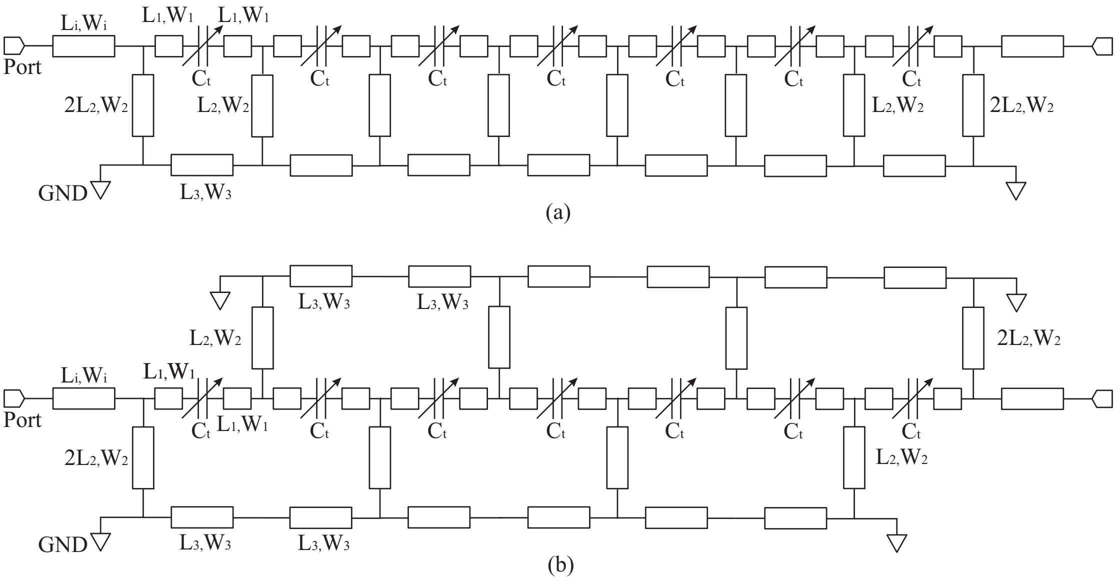

**Figure 4.11:** (a) Layout of the 7-unit cell left-handed transmission line. (b) Modified circuit to simplify the biasing concepts.

The proposed left-handed phase shifter was designed for a bandwidth with a center frequency of 12 GHz. The agilent ADS simulation tool was used for the lumped element circuit and the method of moment simulations. In the first step of the design process, the equation 4.25, equation 4.26, and a lumped element simulation were used to find the initial values for the series capacitor and shunt inductors to be matched to 50 Ω and have a center operation frequency of 12 GHz. In the next step, the momentum solvers were used to define IDC (the series capacitor) and inductive strip lines. To increase the accuracy of the simulation, the varactors were first designed on a substrate consisting of a 1.7 µm thick BST layer on top of an aluminum oxide substrate with 635 µm thickness. Later, the other sections of the phase shifter were simulated directly on top of the aluminum oxide substrate. The phase shifter layout and optimized design parameters are given in figure 4.12, which consist of tunable IDCs, inductive strip lines, and radial stubs as virtual grounds on a single metallization layer. The phase shifter consists of 15-unit cells, each containing a series IDC and two shunt inductive strip lines.

In order to apply the biasing voltage, the inductive lines are alternately connected to two different RF-ground lines. This concept allows for the simultaneous biasing of all IDCs by applying a DC-voltage at the input and output ports. In addition, this concept decreases mutual coupling between inductive lines. According to the unit cell concept, the first and last inductive shunt lines are two times longer than the other lines (figure 4.11(b)). The dimension of these lines was used to optimize the phase shifter input and output matching.

To reduce fabrication complexity, radial stubs were used as virtual RF-grounds for a via-free structure. The realization of holes (ground vias) in ceramic substrates demand a relatively large technological effort, for example with regard to laser drilling. Moreover, it will be difficult to define a biasing concept for phase shifters in a phased array realization. Since phase shifters need to be driven by different voltages, virtual RF ground is needed. In this case, radial stubs are used to generate virtual RF grounds and, furthermore, provide the DC control electrodes (biasing) of the phased array. Hence, MoM simulations show that they have a negligible effect on the phase shifter performance for a center frequency of 12 GHz. It should be mentioned that the use of radial stubs has the disadvantage that they increase the overall dimension of the phase shifter due to their size. Furthermore, radial stubs cause a band limiting effect, since they have a fixed length and therefore a frequency dependent behavior. However, the band limitation of the phase shifter is not critical for a phased array application. The phase shifters typically have a wider bandwidth than the radiating elements with a limited frequency range in a phased array antenna [10].

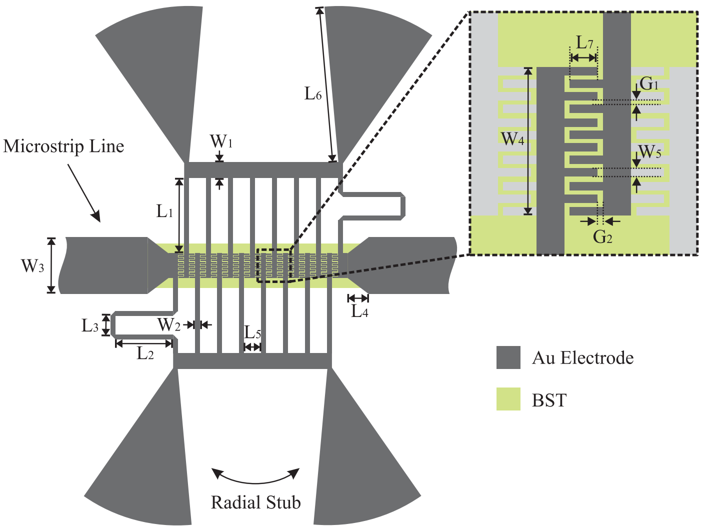

| | (mm) | | (mm) |
|---|---|---|---|
| $L_1$ | 0.82 | $W_1$ | 0.17 |
| $L_2$ | 0.82 | $W_2$ | 0.05 |
| $L_3$ | 0.82 | $W_3$ | 0.62 |
| $L_4$ | 0.82 | $W_4$ | 0.27 |
| $L_5$ | 0.82 | $W_5$ | 0.015 |
| $L_6$ | 0.82 | $G_1$ | 0.008 |
| $L_7$ | 0.82 | $G_2$ | 0.01 |

**Figure 4.12:** Layout of the left-handed phase shifter composed of a single metallization layer including series IDCs and a parallel inductive line section.

### The Phase Shifter Implementation

In the primary step of the left-handed phase shifter fabrication process, a BST thick-film is printed on an alumina substrate using a piezoelectric drop-on-demand inkjet printer, as proposed in section 3.1.2. The final BST layer has a thickness of 1.7 µm and a width of 550 µm after sintering. The top electrode has been patterned by a single photolithography process. The thickness of the gold layer was reached to 3 µm through electroplating. Figure 4.13 shows the prototype of the manufactured left-handed phase shifter. To reach the maximum tunability and increase the electrical field in the BST layer, the gap width of the capacitors is designed to be 8 µm. In order to protect the VNA ports from the applied bias voltages, two bias-tees are connected to the ports.

The simulation and measurement S-parameter results are depicted in the figure 4.14(a) and (b). On the one hand, the insertion loss measurements of the phase shifter in tuned and untuned states have an almost constant value at 12 GHz (around 9 dB), which shows the compensation of the inherent material loss of BST with the characteristic of the left-handed lines. On the other hand, the characteristic line impedance changes with capacitor tuning and affects the measured return loss of the left-handed phase shifter. The maximum return loss throughout the covered bandwidth is -13 dB.

The maximum differential phase shift and corresponding FoM are shown in figure 4.14(c). In this simulation, the permittivity of the untuned BST layer is 200. By changing the permittivity to 110, the capacitance of the IDCs changes and a phase shift of 390 ° at 12 GHz is achieved.

By changing the bias voltage from 0 V to 200 V, a maximum phase shift of 382 ° at 12 GHz is achieved in the measurement. According to the measurement results at 12 GHz, the maximum insertion loss is 10 dB, resulting in an FoM of 38 °/dB. Due to the characteristics of BST varactors, the curve can be tuned continuously between the two states, thus the complete range between them can be covered. As shown in figure 4.14(d), the achieved phase shift (PS) versus tuning voltage (TV) at different frequencies shows almost a linear relation in the coverage bandwidth from 10 GHz to 13 GHz ($\mathrm{PS} \approx 2 \cdot \mathrm{TV}$ at 12 GHz).

Figure 4.15 depicts the comparison of the presented and reported phase shifters based on BST thin and thick film at X-band, revealing that the achieved phase shift/FoM per length is among the highest reported phase shifts at this frequency range. The reported higher phase shift/FoM per lengths were for the phase shifters in CPW and coplanar strip environments, Sazegar [6], which is not easily integrable in the phased array antenna in comparison to the presented left-handed phase shifter with microstrip ports. The total size of the presented left-handed phase shifter including the radial stubs is $4{\times}6\,\mathrm{mm}^2$, which corresponds to $0.16\lambda{\times}0.24\lambda$ at 12 GHz and is suitably compact for implementation in a two-dimensional array.

Moreover, the selective inkjet printing of the BST thick film in the presented phase shifter is an advantage with regard to the operational bandwidth of the phased array. In the conventional screen printing process, which is implemented in reported phase shifters, the carrier substrate is covered by BST film [24]. The IDC varactors and non-tunable components, including the antenna and feeding network, are subsequently patterned on top of BST thick film [24]. Due to the high permittivity of the substrate, this prototype

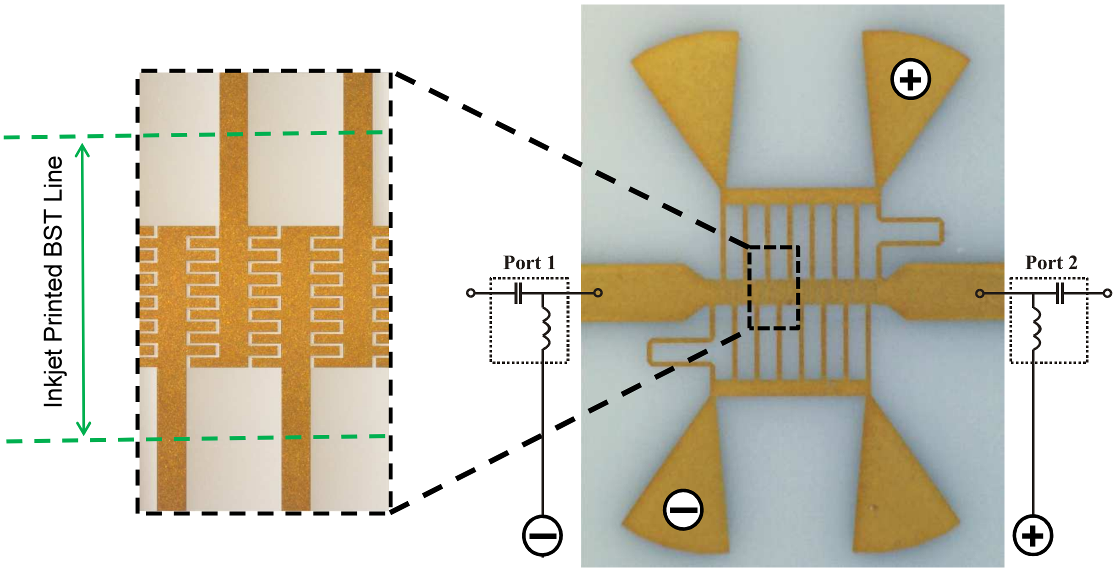

**Figure 4.13:** The prototype of the manufactured left-handed phase shifter. The tunable IDCs are delineated by the dashed lines. The BST line is printed in the IDCs region.

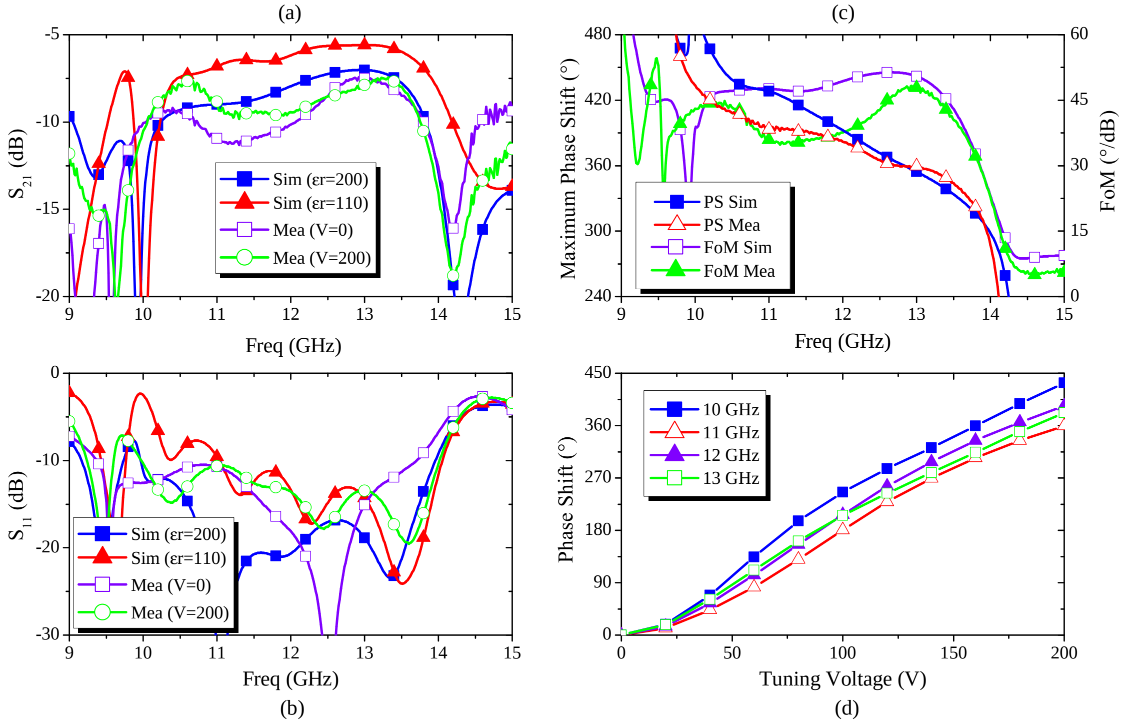

**Figure 4.14:** (a) and (b) Simulated and measured S-parameter of the phase shifter. (c) Maximum phase shift and FoM of the phase shifter. (d) Phase shift versus tuning voltage at different frequencies.

reduces the efficiency of the microstrip antennas and as result increases the surface mode and effectively reducing the bandwidth of the antenna [10]. In the flexible and selective printing process, such as inkjet printing [10, 24], the BST film is printed only in the area, which will be covered by tunable elements. It, thus, prevents extra loss for the non-tunable components.

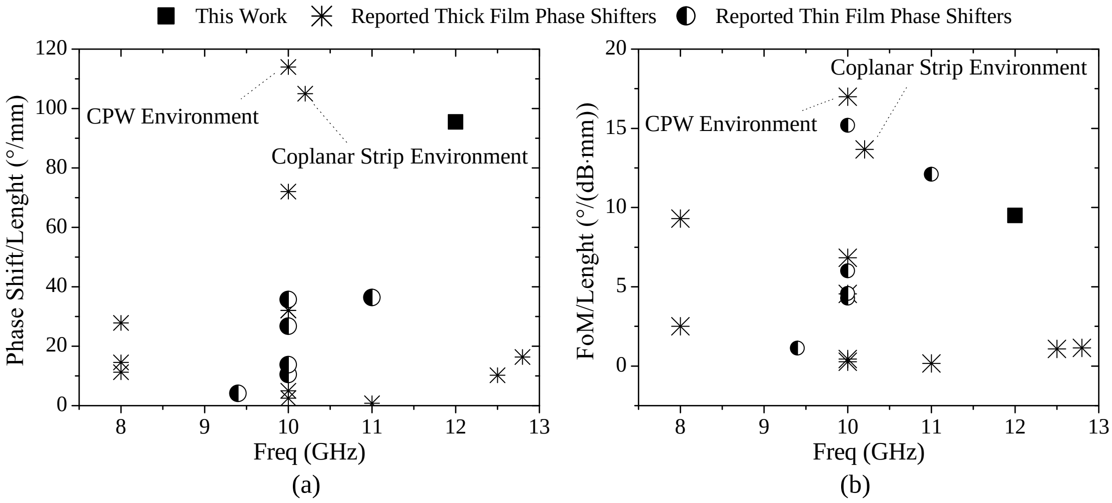

**Figure 4.15:** Comparison of the reported phase shifters based on BST thin and thick films [6, 10, 35, 53, 68] and presented left-handed phase shifter: (a) phase shift/length and (b) FoM/Length.

## 4.5 Prototype of a Right-Handed Phase Shifters

In the previous section, a compact phase shifter for implementation in a planar phased array antenna was presented. In the following, the method to implement fully printed phase shifters is presented. Because of the fabrication process, the fully printed varactors have a higher fabrication tolerance in comparison to the conventional IDC varactors patterned by photolithography and electroplating (chapter 3). Thus, the right-handed structure will be used for the realization of the fully printed phase shifters, since they have a simple structure and lower sensitivity to the parameter variation in comparison to the left-handed structures. Figure 4.16 shows the ideal equivalent circuit of the right-handed transmission line loaded with tunable capacitors $C_t(V)$.

The impedance and the phase constant of the transmission line unit cell can be determined by:

$$Z = \sqrt{\frac{L'}{C'\cdot(1+\sigma)}} \quad , \quad \beta = \omega\sqrt{L'\cdot C'\cdot(1+\sigma)} \tag{4.27}$$

in which the loading factor $\sigma$ and capacitance ratio $\eta$ are defined as follows:

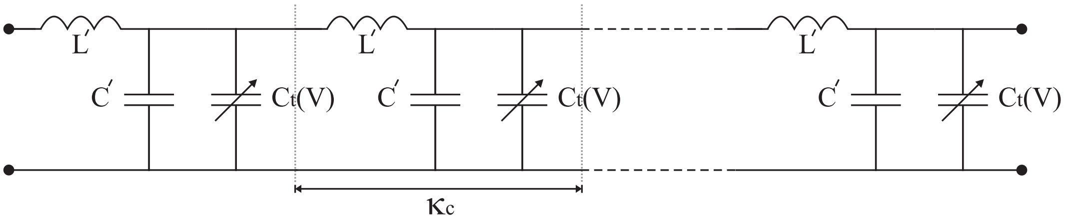

**Figure 4.16:** Equivalent circuit model of the periodically loaded transmission line.

$$\sigma = \frac{C_t(V)}{C' \cdot \kappa_c} \quad , \quad \eta = \frac{C_t(V_1)}{C_t(V_2)} \tag{4.28}$$

$C(V_1)$ and $C(V_2)$ represent the capacitance for different biasing voltages ($V_1$ and $V_2$). The transmission line cut-off frequency (bragg frequency) can be calculated in the following [60]:

$$f_c = \frac{1}{\pi \cdot \kappa_c \cdot \sqrt{L' \cdot C' \cdot (1+\sigma)}} \tag{4.29}$$

The tunable capacitance of the transmission line changes the phase constant. The phase shift of a single unit cell is obtained to be:

$$\Delta\phi = \omega \cdot \kappa_c \cdot \sqrt{L'C'} \cdot (\sqrt{1+\sigma} - \sqrt{1+\sigma \cdot \eta}) \tag{4.30}$$

By increasing the loading factor $\sigma$ and capacitance ratio $\eta$, the phase constant variation increases, which leads to a higher phase shift per unit cell. As a result, the higher loading factor reduces the total number of unit cells required to achieve 360 ° phase shift. The total loss per unit cell $IL_{\text{Total}}$ of the phase shifter has two parts [69, 70], varactor loss $IL_C$ and transmission line loss $IL_t$:

$$IL_{\text{Total}} = IL_C + IL_t \tag{4.31}$$

$$IL_C = \pi \cdot \frac{f^2}{f_c} \cdot C_t(V_1) \cdot Z \quad , \quad IL_t = \alpha \cdot \kappa_c \cdot \frac{1}{Z} \cdot \sqrt{\frac{L'}{C'}} \tag{4.32}$$

$\alpha$ is presenting the attenuation factor per unit length of the unloaded line. $f_c$ is the varactor cut-off frequency and is defined by the capacitance and loss in the varactor. The FoM of the periodically loaded transmission line can be obtained as [35]:

$$\text{F}oM = \frac{\omega \cdot (\sqrt{1+\sigma} - \sqrt{1+\sigma \cdot \eta})}{8.686 \cdot (\frac{\sigma}{2\sqrt{1+\sigma}} \cdot \frac{\omega^2}{\omega_c} + \alpha \cdot \sqrt{\frac{1+\sigma}{L'C'}})} \qquad (°/\text{dB}) \tag{4.33}$$

By replacing variables in the aforementioned equations, the FoM increases with the loading factor $\sigma$. A high loading factor increases the variation of the impedance of the loaded transmission line. Therefore, in order to have good impedance matching around 50 Ω with a high loading factor, the impedance of an unloaded transmission line needs to be high [35].

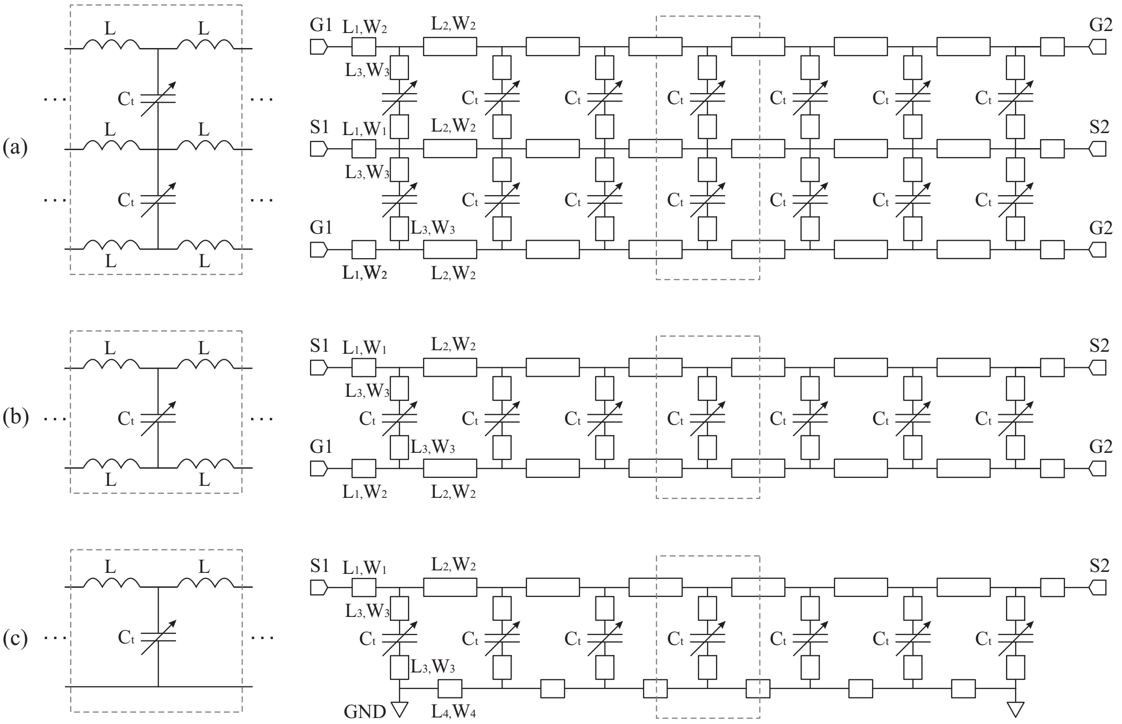

**Figure 4.17:** Equivalent circuits and advanced circuit models were designed for the realization of a right-handed loaded line phase shifter. The unit cells are marked with dashed lines.

Based on the presented right-handed loaded line, three configurations were designed for loaded line phase shifters. The simplified equivalent circuit diagram are shown in figure 4.17. The extended circuit model can implement these equivalent circuits consisting of conductive strips and discrete varactors. As shown in figure 4.17(a), the first design is based on a coplanar waveguide (CPW) transmission line, which is loaded with varactors. Based on this structure, a load line phase shifter is designed for the frequency range from 8 GHz to 10 GHz. The Agilent ADS simulation tool is used for the lumped element circuit and the method of moment simulations. To increase the accuracy of the simulation, the tunable capacitors are first designed on a substrate consisting of a 2.2 µm thick BST layer on top of an aluminum oxide substrate, and the other section of phase shifter directly on top of the aluminum oxide substrate. The phase shifter prototype consisting 9-unit cell is shown in figure 4.18(a), Nikfalazar et al. [22]. Two BST strips were inkjet printed on top of the substrate and the capacitors were placed on top of them. The BST strips have a thickness of 2.1 µm and width of 300 µm. The total size of phase shifter is $8 \times 6\,\text{mm}^2$.

The phase shifter simulation and measurement results illustrated in figure 4.18(b), (c) and (d). The permittivity of the untuned BST layer is 220. By changing the permittivity of the BST layer to 140, a phase shift of 170° at 10 GHz can be achieved. To reach the maximum tunability, the gap width of the capacitors is designed to be 10 µm. The return loss of the phase shifter is below -15 dB in the coverage bandwidth. Because of the BST material properties, the insertion loss decreases with the change in permittivity. The maximum insertion loss is for the permittivity of 220 in the untuned state. By changing the bias voltage from 0 V to 200 V, a phase shift of 175° at 10 GHz is achieved. Simulation and measurement results show a good agreement. The reason of the difference in the insertion loss is the fact that the tangent loss of the BST is higher than expected. At 10 GHz the insertion loss is 8.5 dB that gives FoM of 20°/dB. Based on this results and reported literature [35], the main disadvantages of this structure are:

- The loss of the phase shifter increasing for a high loading factor, due to the limited CPW line impedance range.
- The circuit has a low FoM and a large footprint, which indicated its unsuitability as a phase shifter.

The second design is optimized to account for the aforementioned problems. It uses a coplanar stripline (CPS) and can be assumed to have a high impedance for the unloaded transmission line and relatively low loss, which increases the FoM [35]. Moreover, in comparison to the CPW structures, the CPS is more compact. In order to obtain a CPS transmission line, the equivalent circuit diagram of the basic design is transformed into the second design (figure 4.17(b)). This circuit has the same properties as the basic design (figure 4.16). However, half of the inductance line values are in both ports of each unit cell. This circuit can be created by a physically symmetric circuit. Moreover, there is no need for the RF ground (such as radial stubs) in this structure. Thus, it operates over a wide frequency-band and is suitable for the study of the different BST composites functionality (table 3.4).

The third design features an unbalanced structure to be integrable in a phased array antenna (figure 4.17(c)). The in- and out-port are implemented in microstrip technology. Doubling the capacitance values is required to obtain the same total capacitance in each unit cell compared with the basic design. In the ideal case, this circuit also has the same properties as the equivalent circuit diagrams of the basic design (figure 4.16) and first design (figure 4.17(a)).

### 4.5.1 Fully Printed Tunable Phase Shifters

In recent studies, the concept and fabrication of a fully screen-printed tunable phase shifter based on low temperature sintered BST thick-film were described [3, 27]. Due to low printing accuracy and low tunability of the capacitors in these studies, the FoM did not exceed 15°/dB at 3 GHz, making these devices inapplicable for beam scanning

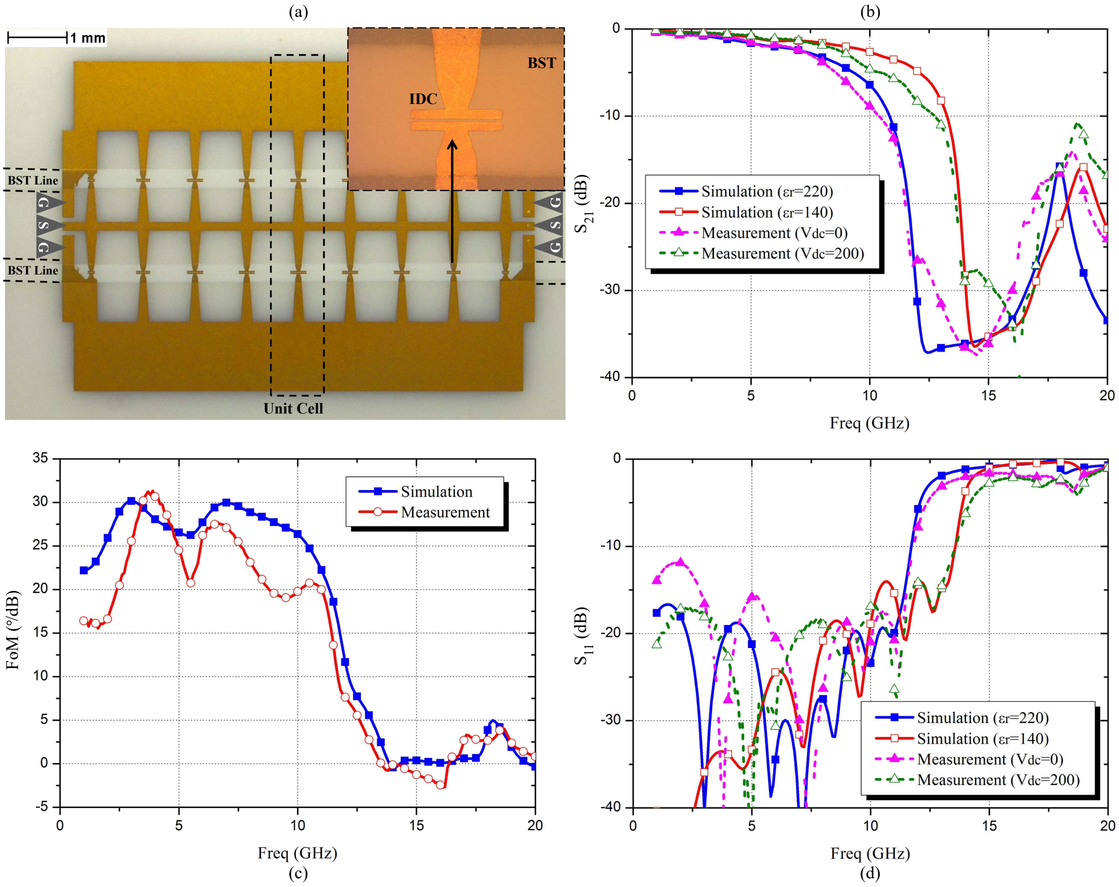

**Figure 4.18:** (a) The photography of the 9-unit cell loaded line phase shifter in a CPW line environment. (b) and (d) the S-parameters, (c) phase shift and FoM of the phase shifter by applying maximum 200 V tuning voltage.

applications. Therefore, in this section, a new process and designs are proposed for the fabrication of fully printed tunable components. With these proposals, the printing accuracy and thus the maximum achievable phase shift could be increased. To show the application of this technology, tunable phase shifters were implemented and measured for phased array antenna application. These structures were fabricated by two different printing technologies: screen and inkjet printing.

### A. Fully Inkjet-Printed Phase shifter

The fully inkjet-printed phase shifter was designed to operate at 3 GHz. Based on the equations presented in section 4.3 for matching the tunable phase shifter with a 50 Ω transmission line at 3 GHz, the required capacitance of each unit cell is approximately 1.6 pF. Therefore, the fully inkjet-printed MIM varactors with three repeatedly printed BST layers (9 µm thickness) and a capacitance of 1.6±0.2 pF were used (table 3.2). The equivalent circuit and layout of a unit cell of the phase shifter based on a CPS transmission line model is illustrated in figure 4.19. Each unit cell consists of inductive lines and two tunable series capacitors.

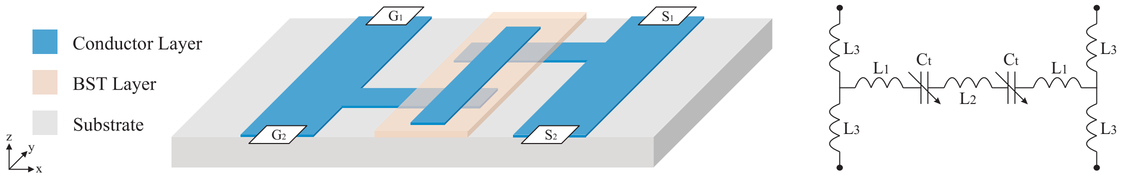

**Figure 4.19:** The structure and unit cell equivalent circuit model of the load line phase shifter.

The phase shifter was inkjet printed and sintered in accordance to the procedure utilized for the fabrication of the MIM varactors (section 3.3). The photograph of the fabricated phase shifter is shown in figure 4.20. It consists of 7-unit cells. The silver lines have a thickness of 3 µm, while the BST layer has a thickness of 9.8 µm. The total size of the phase shifter is 3.6×0.145 cm$^2$. Each MIM varactor is formed by the intersection area of the top and bottom silver electrodes, which is 130×110 µm$^2$.

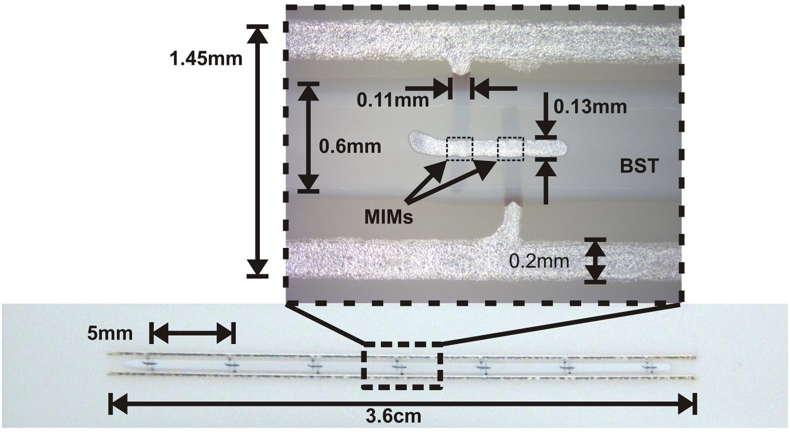

**Figure 4.20:** The photograph of a 7-unit cell fully inkjet-printed loaded line phase shifter.

To contact the phase shifter, two GS 1250 µm pitch probes were used at both ports of the component, which were connected to bias-tees in order to provide the DC tuning voltage. The component was measured in a two-port setup with a VNA. The maximum applied tuning voltage of 200 V was used for the work carried out. However, due to the series connection of both capacitors, the applied bias voltage of 200 V reduced the effective tuning voltage to 100 V at each varactor. The simulated and measured S-parameters of the 7-unit cells phase shifter are depicted in figure 4.21.

In the simulation, the relative permittivity of the BST thick-film is assumed to be 120 in the untuned state and 85 in the maximum tuned state, which corresponds to a tunability of $\tau = 29\%$. At the maximum tuning voltage (200 V), a phase shift of 156° is achieved at 2.8 GHz. The tuning voltage divided between two varactors causes a maximum electric field of 10 V/µm in each varactor. The return loss of the phase shifter decreases when increasing the tuning voltage, which is a consequence of the capacitance change, leading to an impedance change of the phase shifter. The maximum return loss is below -20 dB at 2.8 GHz in the untuned state. The FoM is shown in figure 4.21(d). The maximum measured insertion loss at 2.8 GHz is 7.2 dB, which gives a FoM of 22 °/dB.

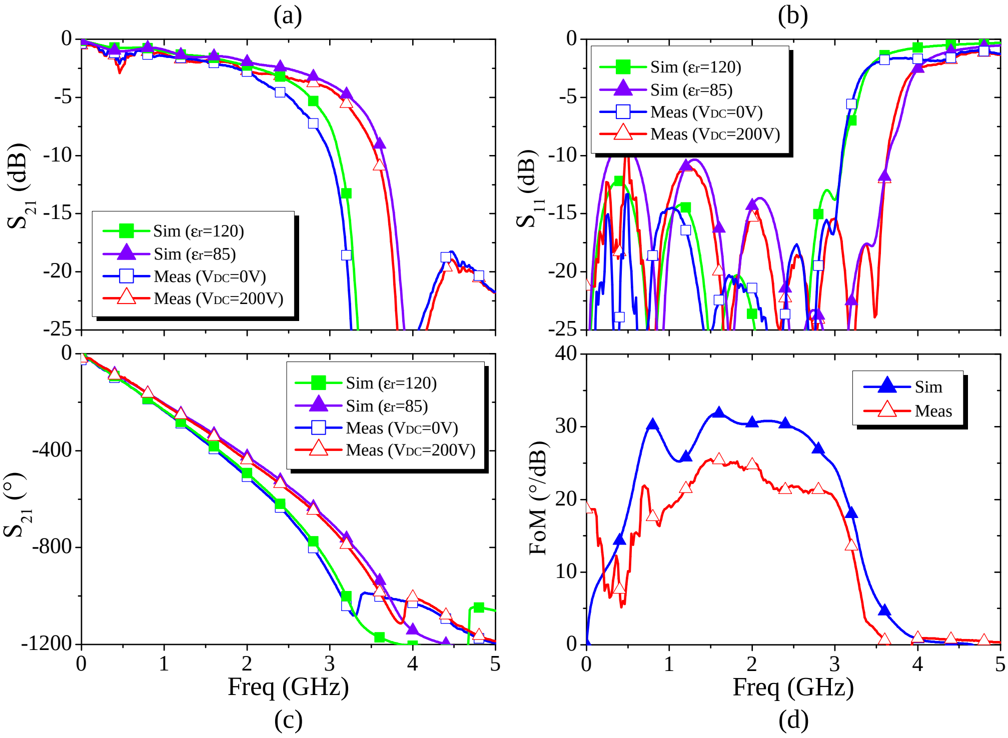

**Figure 4.21:** (a) The magnitude of $S_{21}$ in dB, (b) the magnitude of $S_{11}$ in dB, (c) the phase angle, in degrees, of $S_{21}$ in Deg and (d) the FoM of the simulated and measured inkjet-printed loaded line phase shifter.

Because of the fabrication tolerance of the BST film thickness and parasitic microstrip propagation mode, the insertion loss in untuned and maximum tuned states is not completely identical to the simulation results. This is due to the inaccuracy of the printed lines and hence, the capacitance tolerance of each varactor causes deformation of the filter spectrum shape.

### B. Fully Screen-Printed Phase Shifters

This part is aiming to evaluate different low-temperature sintered BST composites (table 3.4), which are developed for the screen printing process in order to achieve frequency extension of the fully printed phase shifter. For the operation of the phase shifter in a higher frequency range, it is crucial to reduce the value of the tunable capacitor (figure 4.6). Through the use of the presented structure for the inkjet-printed phase shifter and implementation of four different low sintered BST composites, the application frequency of the phase shifters is changed in this approach. Since, the minimum line width of the silver line is 100 µm in screen printing technology. The values of the tunable capacitors were varied from 2.2 to 0.14 pF by using the same dimensions however a different BST composite, with different relative permittivity.

The phase shifters were printed and sintered similarly to the fabrication of MIM varactors on top of the alumina substrate (section 3.6). The prototype of the fabricated phase shifter based on CuF-BST-5ZB composite is depicted in figure 4.22. The silver lines have a thickness of 13 µm, while the BST layer has a thickness of 5.9 µm.

The phase shifters were measured in the same setup as explained before. The simulated and measured insertion loss in untuned and maximum tuned status, phase shift, and FoM of the phase shifters, consisting of 7-unit cells, are shown in figure 4.23. The presented results show that, by using different low temperature sintered BST composites, a C-band is achievable for fully printed components based on screen printing technology. A FoM of 70 °/dB at 1.7 GHz is achieved by using the CuF-BST-5ZB composite, which is the highest reported FoM for a phase shifter based on BST thick film [3, 6, 27]. Furthermore, the phase shifters based on CuF-BST-20ZB and 80BST-20Mg3B2O6 composites show high performance at S- and C-band. The presented phase shifter based on BST-50Mg3B2O6 composite achieved a FoM of 22 °/dB at 7.6 GHz, which is the highest reported operation frequency for a fully printed phase shifter. However, because of low tunability of the BST composite, the phase shift is low. This can be further improved by increasing the capability of the BST composite.

These new approaches show a reasonable application field for new BST composites. In addition, these materials can be used in LTCC technology as a tunable dielectric that has a low sintering temperature, adequate tunability and reduced permittivity. In fully screen-printed phase shifters, the FoM is higher compared to the phase shifters when fully inkjet printed. This can be rationalized by a conductor loss. In screen printing, the thickness of the silver layer reaches up to 13 µm, which is six times higher than thickness of the inkjet-printed silver line.

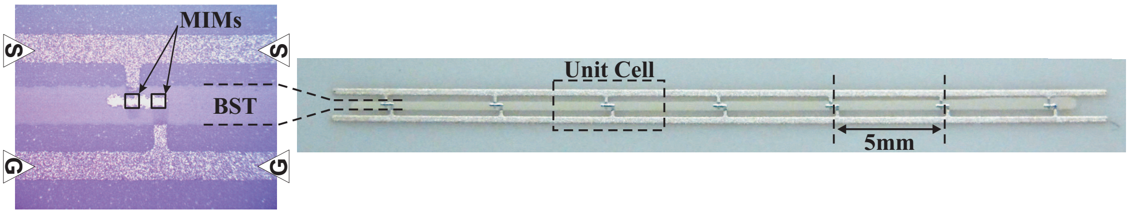

**Figure 4.22:** Top view of the 7-unit cells screen-printed loaded line phase shifter. The tunable MIMs are marked by the dashed lines.

### C. LTCC Phase Shifters Based on Tunable Ferroelectric Composite Thick Films

Based on the design presented in the previous section, a phase shifter is demonstrated, which is implemented in LTCC technology. In this work, the phase shifter design, measurement and modeling have been done by Nikfalazar [71]. The fabrication process has

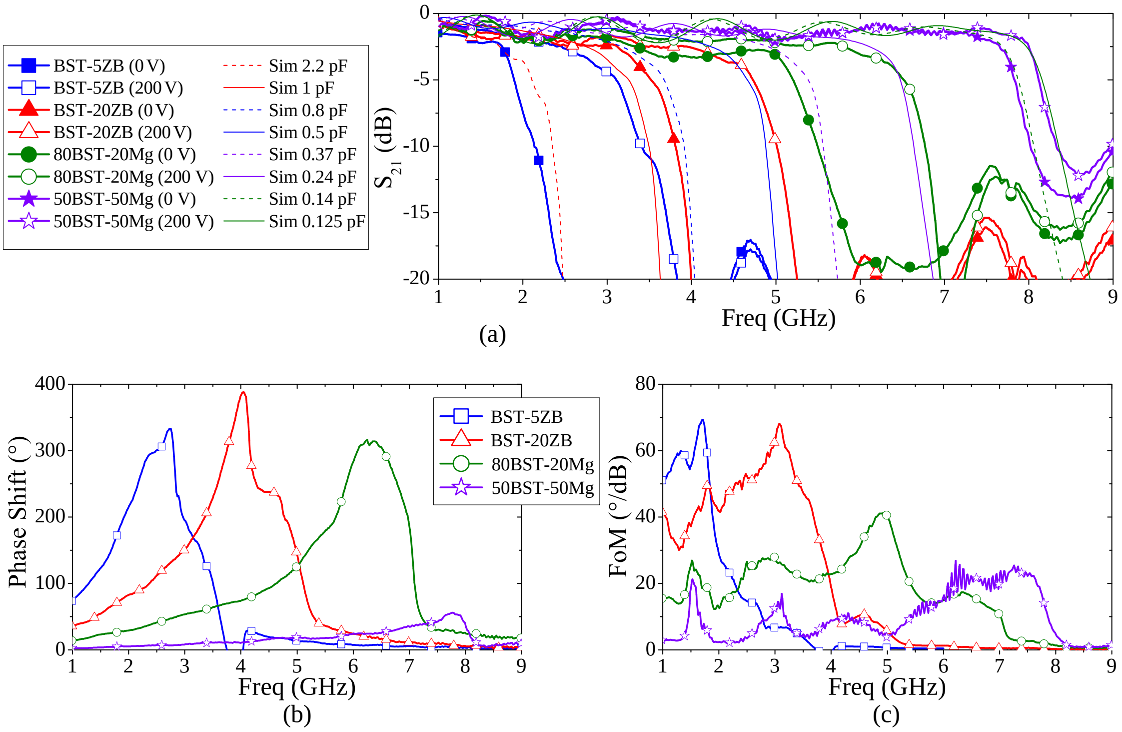

(a)

(b)

(c)

**Figure 4.23:** (a) Simulated and measured insertion losses (untuned and maximum tuned state), (b) measured phase shifts and (c) measured FoMs of the screen-printed phase shifters.

been done in the Federal Institute for Materials Research and Testing (BAM) with the BST paste developed by Kohler in KIT [49].

Figure 4.24 shows the layout of the single unit cell phase shifter implementation in LTCC technology and a top view of the fabricated sample. As LTCC material, a commercial product from DuPont (DP951 with a relative permittivity of 7.8 and loss-tangent of 0.006 at 3 GHz) was used with an unfired tape thickness of 254 µm. DuPont silver pastes 6141 (for via filling) and 6145 (conductor) were applied as electrode material. The phase shifter design consists of four layers of LTCC. The actual phase shifters were positioned between the second and third layer. The buried structures were connected to the surface by silver vias (0.2 mm diameter).

Screen printing of BST paste and inner conductors was performed with 400 screen meshes. In the first approach, the BST paste (copper-fluorine codoped BST and 5 vol. % ZnO-$B_2O_3$) was printed twice to achieve a homogeneous layer due to the low solid content (sample 1). In the second route, BST solid content was increased via evaporation of terpineol and printed once (sample 2). The thicknesses of the dried layers are up to 25 µm for the silver structures and between 6 and 15 µm for the BST layers. The DP951 film with the structured phase shifter is covered by additional layers of DP951 film and co-fired at 850 °C.

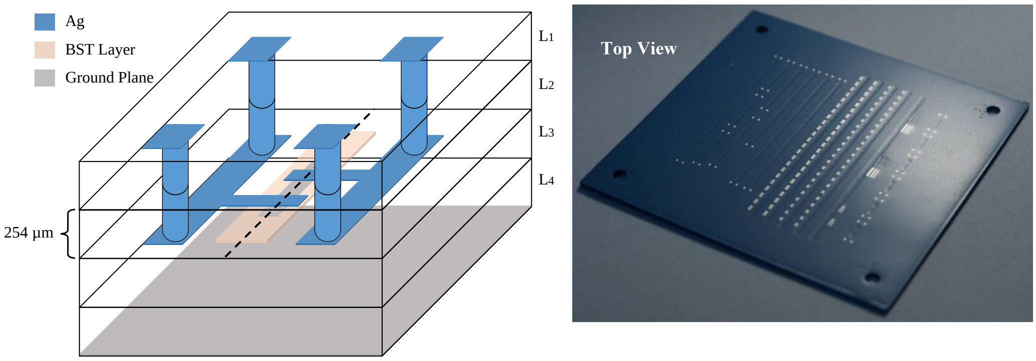

**Figure 4.24:** Structure of the one unit cell phase shifter for LTCC technology (left). Top view of the fabricated sample (right).

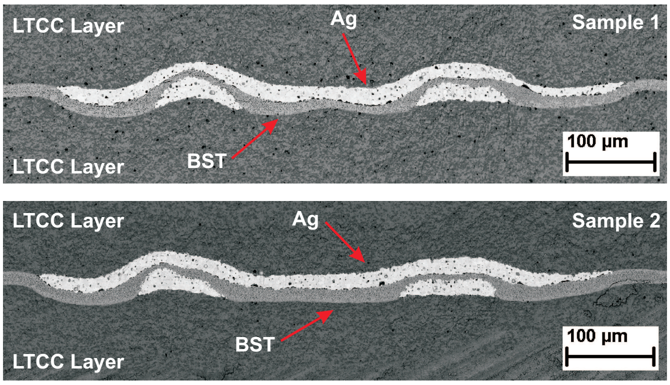

**Figure 4.25:** Field and SEM cross-sectional image of the MIM varactors.

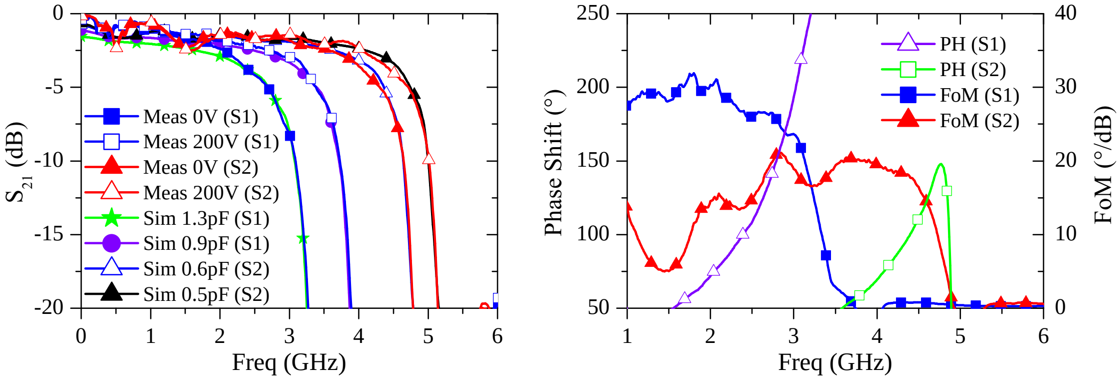

**Figure 4.26:** The simulated and measured insertion loss of the LTCC phase shifters in untuned and maximum tuned states (left) and measured maximum phase shift and FoM of the phase shifters (right).

After printing, the LTCC sheets are cut with a hot knife to $70{\times}70\,\mathrm{mm}^2$ and laminated in an uniaxial press at 70 °C and 22 MPa for 10 minutes. The laminates were afterwards fired in a tube furnace under purified dried air at 850 °C for 20 minutes (figure 4.24). The SEM cross-sectional image of the MIM varactors for sample 1 and sample 2 (dash line in figure 4.24) are shown in figure 4.25. It shows no migration of the silver electrodes to the BST layer. The silver layers have a thickness of 16 µm separated by a 5 µm thick BST film. In the first method, each two series of MIM varactor within a single unit cell has a measured capacitance of 1.3 pF at 3 GHz. A tunability of 31% was achieved by applying 200 V (100 V between the two silver electrodes). In the second process, a capacitance of 0.6 pF at 4.4 GHz and tunability of 17% was measured.

The phase shifters were measured by using GS probes. The probes were contacted to pins that were connected to the phase shifter in the middle layer. The simulated and measured insertion loss of the 7-unit cells phase shifters are depicted in figure 4.26. It shows a pass band shift depending on the applied voltage in untuned (0 V) and maximum tuned states (200 V) in measurement. The comparison of simulated and measured insertion loss shows a very good agreement. It can be concluded that the fully printed varactors by the LTCC method have a lower tolerance of the capacitance value due to the higher fabrication accuracy. This is especially apparent when compared to the phase shifters presented through conventional screen printing, which did not completely correspond to the simulation results (figure 4.23).

Figure 4.26 illustrates the FoM of the phase shifters. The maximum phase shift of 192 ° at 3 GHz is measured by applying 200 V biasing voltage to the first sample. The maximum insertion loss is 8 dB at 3 GHz in the untuned state, resulting in a FoM of 24 °/dB. For the second fabrication method with the thicker BST layer, a phase shift of 98 ° at 4.4 GHz was measured (FoM of 18 °/dB).

When compared to a reported phase shifter with a FoM of 6.6 °/dB at 2.5 GHz [3], these results are a significant improvement in terms of phase shift and frequency range with regard to the applied LTCC technology. This can be explained by a better compatibility of the used BST thick films inside the LTCC module, the lower BST film thickness, as well as the optimized design of the phase shifter. The MIM series configuration reduces the short circuit and misalignment error effect in the fabrication process. By bending the inductive lines, the total length of the loaded line phase shifter can be further reduced. Moreover, a 360 ° phase shift is achievable by increasing the number of unit cells.

### D. Fully Printed Phase Shifter in a Microstrip Line Environment

In the previous section, loaded line coplanar strips were characterized by a high quality phase shifter and demonstrate the concept of fully printed tunable components. In this part, the phase shifter has been modified to be implemented in a phased array antenna and embedded in a microstrip line environment. The microstrip lines are preferred because of their lower losses compared to coplanar lines in phased array antennas [5]. Furthermore, they are based on a asymmetrical line, which can feed patch antennas directly without the need for a balun.

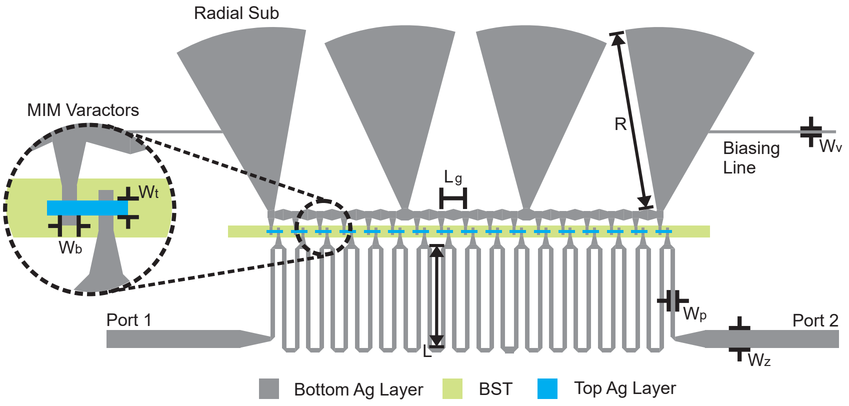

| | (mm) |
|---|---|
| $W_z$ | 0.6 |
| $W_b$ | 0.12 |
| $W_t$ | 0.12 |
| $W_p$ | 0.15 |
| $W_v$ | 0.1 |
| $L$ | 3.5 |
| $L_g$ | 0.6 |
| $R$ | 6.2 |

**Figure 4.27:** The layout of the 17-unit cells phase shifter with microstrip ports, consisting of three layers. The radial stubs have been used as virtual ground, which can be used as a biasing concept of the phase shifter.

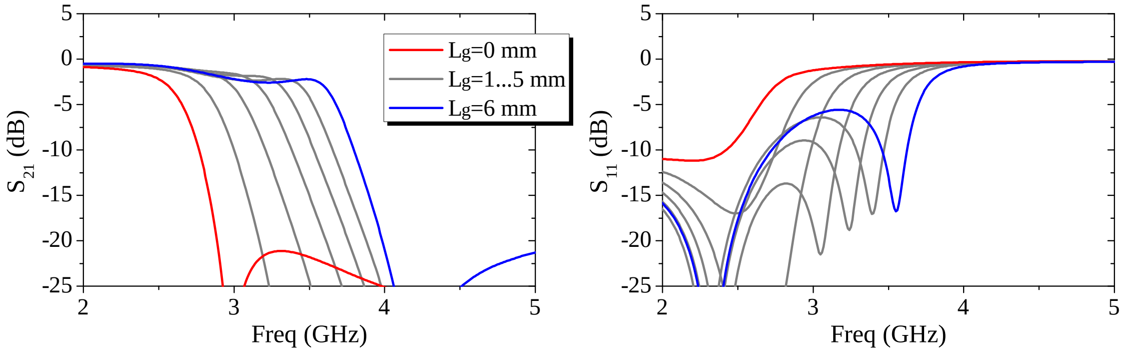

**Figure 4.28:** The simulation result of loaded line phase shifter based on third design. The inductance line $L_g$ varies from 0 to 6 mm.

The third design of a loaded line topology is selected for the tunable phase shifter at S-band (figure 4.17(c)). The layout of the phase shifter, implementing 17-unit cells, is shown in figure 4.27. Each unit cell has two series MIM varactors to allow for tunable capacitive loading of the line. The microstrip lines are connected on both sides over a short impedance transformer with the parallel branch of the MIM varactors. One side of the parallel capacitances needs to connect to virtual ground (radial stub). As presented in section 4.4, the radial stubs not only serve as virtual ground, but are also used for biasing the phase shifters.

The inductance line of $L_g$ (figure 4.17) has proven to be very critical. It can cause a shift of the operation frequency to the lower frequencies. Figure 4.28 shows simulation result of a 3-unit cell phase shifter with a variation of $L_g$ from 0 to 6 mm. In the ideal case, $L_g$ should be zero. This is, however, impossible in practice because of the design limitation to reduce the parasitic effect of $L_g$ lower than discrete number. For the final layout, $L_g$ is accounted for a length of 0.6 mm (figure 4.27).

The 17-unit cell phase shifter was fabricated on top of the alumina substrate as discussed in the MIM varactor section. The CuF-BST-20ZB composites are used for the tunable dielectric layer (table 3.4). The phase shifter including radial stubs has an overall dimension of $11 \times 19\,\mathrm{mm}^2$. The microstrip lines were connected to the SMA connectors for the measurement.

The simulated and measured S-parameters, and photography of the fully printed loaded line phase shifter are shown in figure 4.29. In the simulation, the capacitance of the two series MIM varactors is changed between 1.1 pF to 0.74 pF (33% tunablility). During measurement, a bias voltage between 0 V and 200 V was applied to achieve the required capacitive change and hence allow for the continuous tuning of the phase. There is a good agreement between the measured insertion loss and the simulation. The results show that, due to the resonance of the virtual ground radial stub, the operation bandwidth of the loaded line phase shifter is limited from 2.4 GHz to 3.3 GHz. The disagreement between the measured and simulated return loss is due to the fabrication tolerance of the varactor. In fact, the tolerance in printing the silver electrodes may cause a 10% deviation in the realized capacitance, which ultimately alters the input impedance and return loss of the phase shifter.

Around 3 GHz, an insertion loss lower than 7.3 dB across all tuning states and a maximum phase shift of 274 ° was measured, resulting in a FoM of 37.3 °/dB. The length of the phase shifters is 20% of the wavelength, where its phase shift versus length results in 14.4°/mm, outperforming all previously reported phase shifters based on fully-printed low-temperature sintered BST thick film at S-band [3, 27]. The presented phase shifter achieves a FoM of more than 30 °/dB from 2.5 to 3.2 GHz.

Table 4.1 shows the comparison between the presented fully printed phase shifters and the state-of-the-art variety. The fabricated inkjet- and screen-printed phase shifters (including the LTCC method) have a better functionality (phase shift and FoM) in comparison to the previously reported printed phase shifters, and are suitable for industrial production as a simple and low-cost method. This can be explained by a better compatibility of the used BST thick films, the lower BST film thickness, as well as the optimized design of the phase shifter. Although, not fully printed phase shifters show better functionally at higher frequency range, which is mainly caused by better varactor tunablility. To reach a higher operation frequency range such as X-band based on fully printed phase shifters, the optimization and improvement of the printing resolution and composites of the BST are both necessary.

Moreover, the quality factor of the varactors has the potential to be improved as introduced in the recent investigation of Friederich et al. [41] to further increase the FoM of the phase shifter. For this target, the printing accuracy and conductor loss need to be reduced by improving the silver ink and paste.

**Table 4.1:** Fully printed phase shifters results and comparison with literatures.

| Freq (GHz) | IL (dB) | PS (°) | FoM (°/dB) | Vol (V) | Method | Comp | Elec | Concept | Port | Var | Sin (°C) | Ref | Fully Printed |
|---|---|---|---|---|---|---|---|---|---|---|---|---|---|
| 2.8 | 7.2 | 156 | 22 | 200 | IJ | BST-ZnO-B2O3 | Ag | PLTL | CMSL | MIM | 850 | TW | Yes |
| 1.7 | 2.26 | 158 | 70 | 200 | SP | CuF-BST-5ZB | Ag | PLTL | CMSL | MIM | 850 | TW | Yes |
| 3.1 | 2.4 | 163 | 68 | 200 | SP | CuF-BST-20ZB | Ag | PLTL | CMSL | MIM | 850 | TW | Yes |
| 5 | 3.1 | 125 | 40 | 200 | SP | 80BST-20Mg3B2O6 | Ag | PLTL | CMSL | MIM | 850 | TW | Yes |
| 7.6 | 2.2 | 50 | 22 | 200 | SP | 50BST-50Mg3B2O6 | Ag | PLTL | CMSL | MIM | 850 | TW | Yes |
| 3 | 8 | 192 | 24 | 200 | SP | CuF-BST-5ZB | Ag | PLTL | CMSL | MIM | 850 | TW | Yes |
| 4.4 | 5.4 | 98 | 18 | 200 | SP | CuF-BST-5ZB | Ag | PLTL | CMSL | MIM | 850 | TW | Yes |
| 3 | 7.3 | 274 | 37.3 | 200 | SP | CuF-BST-20ZB | Ag | PLTLM | MSL | MIM | 850 | TW | Yes |
| 30 | 2.6 | 20 | 8 | 100 | SP | BST-MgO | Ag | PLTL | CMSL | CP | 1300 | [26] | Yes |
| 27.5 | 12 | 20 | 1.7 | 100 | SP | BST-MgO | Ag | RT | MSL | CP | 1300 | [26] | Yes |
| 30 | 10 | 40 | 4 | 100 | SP | BST-MgO | Ag | PLTL | MSL | CP | 1300 | [72] | Yes |
| 2.5 | 2.4 | 49 | 20 | 100 | SP | BST-MgO | Ag | RT | MSL | CP | 1300 | [73] | Yes |
| 2.5 | 3 | 63 | 21 | 100 | SP | BST-MgO | Pt, Ag | RT | MSL | MIM | 1260 | [74] | Yes |
| 3 | 1.4 | 20 | 15 | 200 | SP | BST-Li2O | Ag | PLTL | CPW | MIM | 900 | [27] | Yes |
| 2.5 | 0.8 | 4.5 | 6.6 | 200 | SP | BST-Li2O | Ag | RT | MSL | MIM | 900 | [3] | Yes |
| 2.5 | 1.9 | 12 | 6.3 | 200 | SP | BST-Li2O | Ag | DL | MSL | MIM | 900 | [3] | Yes |
| 2.8 | 2.25 | 65 | 29 | 100 | SP | BST | Au | DL | CPW | IDC | 1200 | [75] | No |
| 8 | 1.2 | 25 | 20.6 | 100 | SP | BST | Au | DL | CPW | CP | 1200 | [68] | No |
| 10 | 4.7 | 122 | 26 | 140 | SP | BST | Au | DL | CPW | CP | 1150 | [6] | No |
| 10 | 9 | 342 | 38 | 200 | IJ | BST | Au | DL | CPW | IDC | 1150 | [6] | No |

SP = Screen printing, IJ = Inkjet printing, RT = Reflection type, PLTL = Periodically loaded transmission line, CP = Coplanar capacitor, CPW = Coplanar waveguide, DL = Delay line, MSL = Microstrip line, CMSL = Coupled microstrip line, MIM = Metal-insulator-metal, IDC = Interdigital capacitor, TW = This work

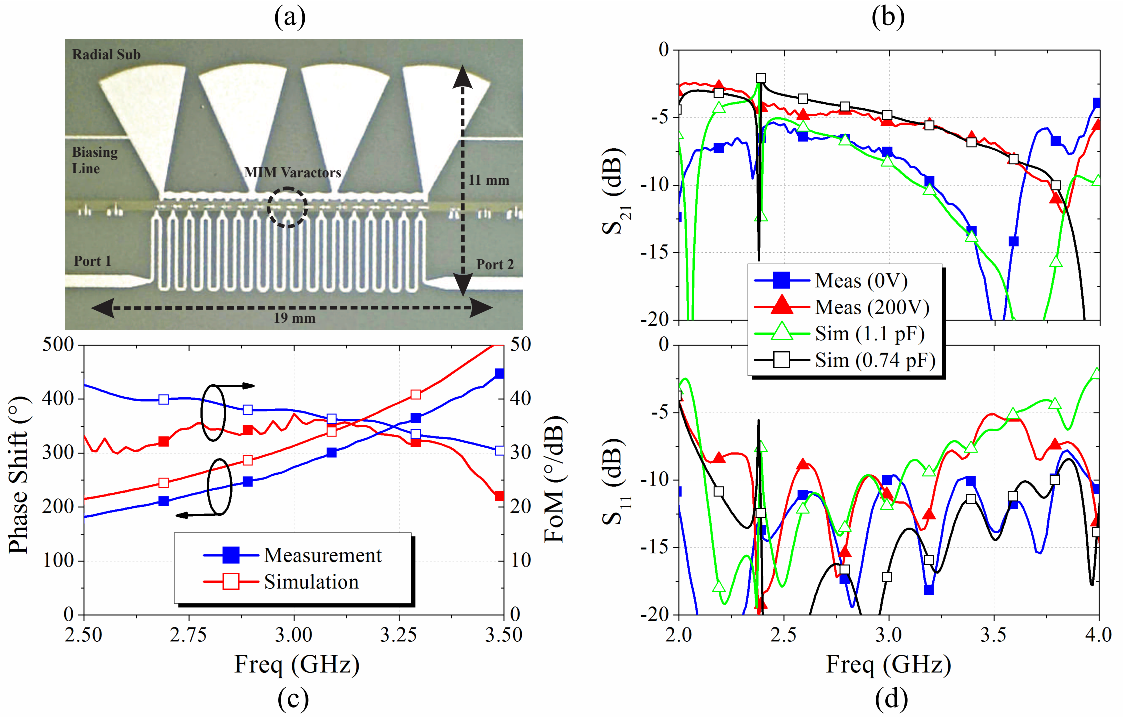

**Figure 4.29:** (a) The photography of the 17-unit cell fully printed loaded line phase shifter in a microstrip line environment. (b) and (d) the S-parameters, (c) phase shift and FoM of the phase shifter by applying maximum 200 V tuning voltage.

### 4.5.2 Tunable Phase Shifter Based on Low Voltage Tuned MIM Varactor

This section presents a method for the implementation of the tunable phase shifter based on inkjet-printed BST thick film by utilizing the low bias voltage MIM varactors (section 3.5). In the first attempt, a phase shifter based on the coplanar stripline structure (figure 4.17(b)) at 8 GHz was presented in the recent investigation of Nikfalazar et al. [76]. The low bias voltage MIM varactors were embedded in this phase shifter, which shows a reduction of the maximum biasing voltage to 50 V. As will be discussed in this section, a second phase shifter will be presented, optimized for integration in a phased array antenna and based on the microstrip structure. The third design of a loaded line topology is selected for the design of tunable phase shifter (figure 4.17(c)). Figure 4.30 shows the layout and dimensions of the designed loaded line phase shifter targeting a 8 GHz operation frequency and consisting of two conductor layers and one dielectric layer. For the realization of series inductors, simple conductive strips were used and connected to parallel capacitors. The terminal of the capacitors are connected to ground planes.

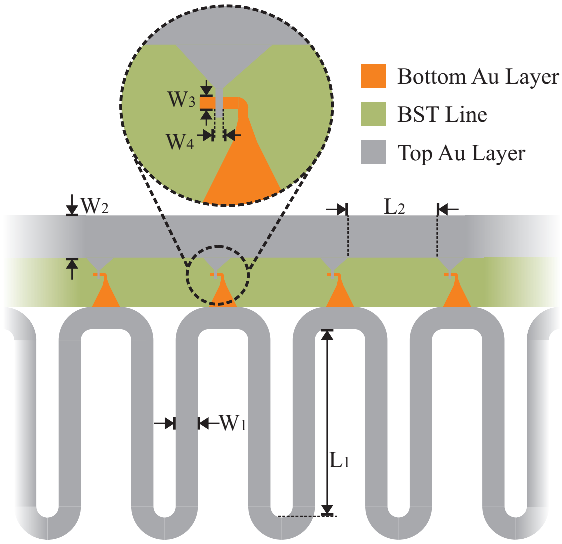

| | (mm) |
|---|---|
| $W_1$ | 0.16 |
| $W_2$ | 0.3 |
| $W_3$ | 0.024 |
| $W_4$ | 0.015 |
| $L_1$ | 1.4 |
| $L_2$ | 0.64 |

**Figure 4.30:** Layout of the loaded line phase shifter composed of multilayer varactors (MIM).

The phase shifter is fabricated in a similar process as explained in section 3.5. The total size of the presented right-handed phase shifter including the radial stubs is $9 \times 4\,\text{mm}^2$ The fabricated structure consisting of 11-unit cells is shown in figure 4.31(a). The characterization was done with a VNA which was connected to the phase shifter by ground-signal probes with a pitch of 350 µm. The ground port is connected to the MIM varactors by the 20 µm width biasing lines. To reduce the influence of the biasing line on the RF signal, it is connected to the connection point of the virtual ground (radial stub) and ground line.

The phase shifters' insertion and return loss results are depicted in figure 4.31(b) and (d). These figures show a comparison between the simulation and measurement results. In the MoM simulation, relative permittivity changes between 133 (untuned) to 70 (maximum tuned) state were assumed. In the measurement, the biasing voltage changes between 0 V to 50 V, which shows comparable results to the simulation. The maximum measured phase shift of 260 ° is achieved by applying maximum biasing voltage of 50 V, which is suitable for the phased-array application. The maximum insertion loss of the phase shifter in an untuned state is 5.9 dB, which gives a FoM of 44 °/dB at 8 GHz. Figure 4.31(c) gives the maximum simulated and measured phase shift and FoM of the phase shifter. It shows a FoM above 40 °/dB across 7 to 8.5 GHz.

In the presented phase shifter, the maximum biasing voltage was reduced to only 50 V, which is much below the typical biasing voltage for BST thick film devices in the range of 200 V [6]. Figure 4.32 the comparison of the presented phase shifter based on inkjet-printed MIM varactors and reported phase shifters based on BST thin and thick films. In Figure 4.32(a), achieved FoMs were divided by maximum applied voltages versus operation frequency. It shows the better functionality of the presented phase shifter,

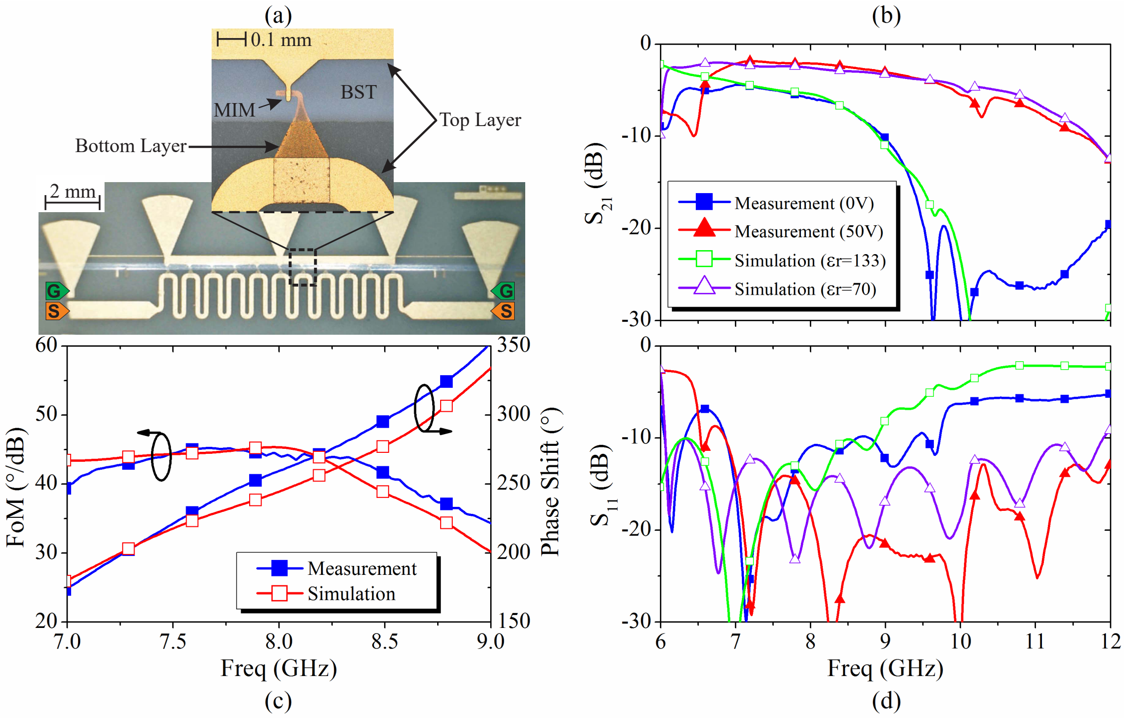

**Figure 4.31:** (a) The photograph of the 11-unit cell loaded line phase shifter. The ground-signal probes with 350 µm pitch are used for measurement. (b) and (d) the S-parameters, (c) phase shift and FoM of the phase shifter by applying maximum 50 V tuning voltage.

which can achieve a high FoM with a lower biasing voltage in comparison to the reported phase shifters based on thick film BST. The conventional phase shifters based on BST thin film operate under a lower tuning voltage in comparison to the phase shifters based on BST thick film [10]. But, the presented phase shifter reaches the functionality of thin-film phase shifters by implementing simple thick film technology. Consequently, to increase the FoM, the loss factor of the BST has to be reduced and the quality factor of the MIM varactors increased. In Figure 4.32(b), achieved phase shift were divided by phase shifter length and maximum applied voltages versus operation frequency. It shows quiet good functionally of the presented phase shifter. The two reported higher values are measured under biasing voltage of 150 V by using left-handed concept for the phase shifter, Sazegar [6]. It can be concluded that, to reach higher phase shifter per length by presented low voltage MIM varactor, the phase shifter can be implemented by the left-handed transmission line concept as a compact structure.

### Phase Shifter Temperature Dependency

As is discussed in chapter 2, the BST properties show a temperature-dependent behavior. This dependence also influences the tunable components, since a change of the permittivity and material losses result in a change of the component or circuit characteristics, such as the capacity and the quality factor. Although, the temperature dependence in BST

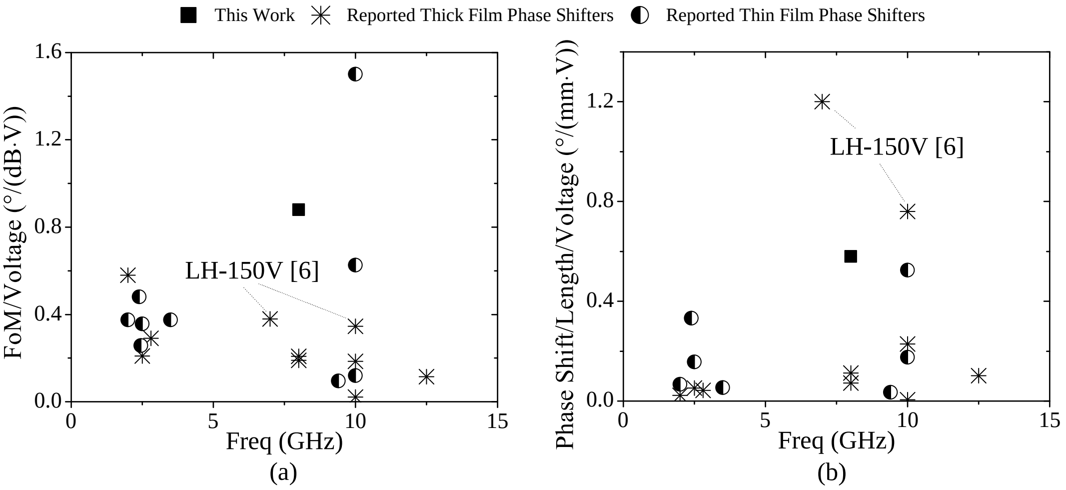

**Figure 4.32:** Comparison of the reported phase shifter based on BST thin and thick films and the presented low bias voltage phase shifter based on inkjet-printed MIM varacotrs: (a) FoM/Voltage and (b) phase shift/length/voltage, [6, 10, 35, 53, 75]

thin and thick film is highly attenuated compared to full ceramics, this property plays an important role in the development of components and circuits, as practical applications inevitably deal with major temperature fluctuations.

The temperature dependency of the presented phase shifter was measured by changing the operating temperature from 20 °C to 100 °C in an untuned state (0 V). In figure 4.33 the measured scattering parameters of the phase shifter with 11-unit cells are depicted for various temperatures, which shows the permittivity of the BST layer reducing when increasing the temperature. The increase in temperature has the same effect as the application of a control voltage since, in both cases, the permittivity and consequently the capacitance of the varactors are reduced. Therefore, the characteristics of the phase shifter changes with increasing temperature to higher frequencies, causing a strong change in the phase. When increasing the operating temperature, a reduction of the loss tangent in the BST layer is observed, which is why the insertion loss greatly decreases. However, because of the continuous tuning of the phase shifter, it is possible to calibrate or adjust the phase to different temperatures in order to have a stable phase shift with tuning voltage. Based on this method, the influence of the temperature changes are compensated in the phase shift.

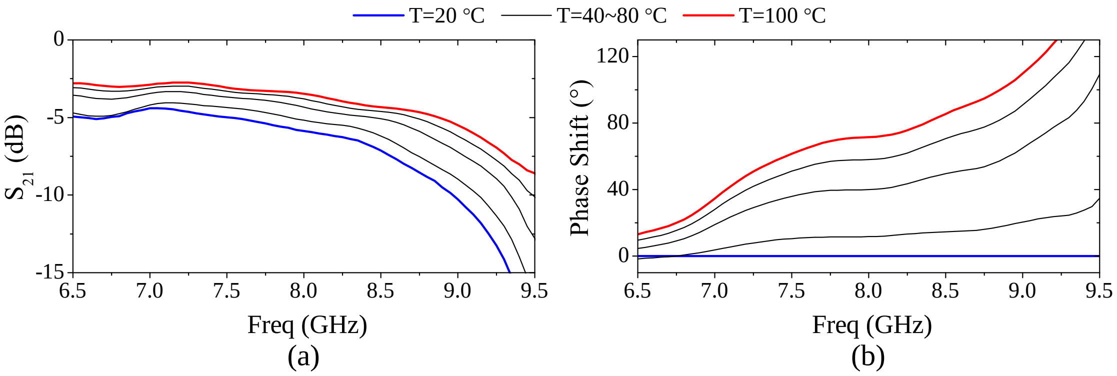

**Figure 4.33:** Measured scattering parameters of the loaded line phase shifter for different temperatures in an untuned state (0 V): (a) insertion loss and (b) phase shift.

# Chapter 5

# Beam Steering Phased Array Antennas

## 5.1 Phased Array Antenna Feeding Network

A feeding network distributes the RF signal to individual radiating elements in a phased array antenna. The feeding can be executed through different methods such as space feed, wave guide, or strip line wiring. Figure 5.1 shows four different feeding methods for a 1×4 element linear array [9, 57]: series and parallel types as waveguide feeding, transmission, and reflection types as free space feeding.

- Series feed: The radiating elements are arranged in a series and progressively receive signals from a feeding line. According to the amount of the phase shift, the beam is directed towards the desired angle. By also adjusting the frequency, the phase of the receiving signal in the radiating element changes. The downsides of this method include limited bandwidth (BW), frequency sensitivity, tolerance of the impedance matching, and beam direction variation at different frequencies. The path difference between the radiating elements needs to be considered for the phase shift as a function of the frequency. At the same time, this configuration can be used for frequency scanning arrays and, when compared to corporate feeding, this method reduces feeding line loss [9].
- Corporate (parallel) feed: The signal is divided in every divider section and later transferred to the radiating element. Thus, all radiating elements receiving a signal with the same phase and change in frequency do not affect the phase difference. The length can be ignored in phase controlling calculations. Such a method is advantageous in terms of frequency independence.
- Transmission type of space feeding: The feeding horn antenna is placed in the back of the radiating elements and transmits a wave towards them such as frequency selective surfaces (FSS). The radiating elements receive the signal by an individual antenna and retransmit it after modifying the signal by phase shifters. In this feed type, the feed antenna does not have any shadow on the transmitted field. For a long focal distance, this configuration is equivalent to corporate feeding and for a short distance, to series feeding with a center feed. By cascading several FSS, the beam scanning range of the array can be expanded [6].

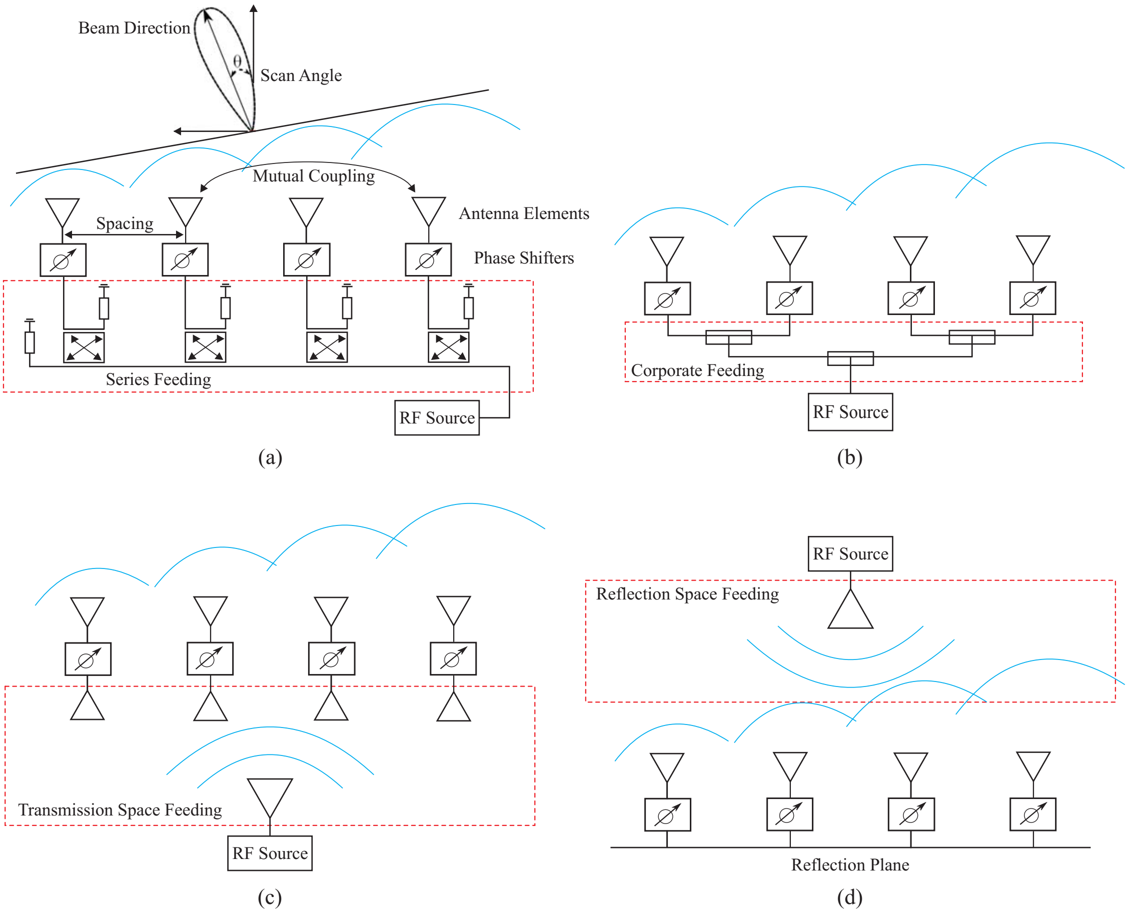

(a) (b) (c) (d)

**Figure 5.1:** (a) The configuration of series feeding, (b) corporate feeding, (c) transmission type of space feeding and (d) reflection type of space feeding for a 1 × 4 linear phased array antenna.

- Reflection type of space feeding: In this configuration, the RF source and feeding antenna are placed in front of the radiating elements. The radiating elements receive the signal from the horn antenna, modify it with the phase shifters and reradiate the wave in the desired direction. The limitation of this method is the absorption of the reflected signal by the feeding antenna (feeding antenna shadow), which can cause a standing wave for a small area of radiating elements in comparison to the feeding antenna. This method shows higher loss in comparison to other concepts [6].

In conclusion of these techniques, the corporate feed shows a simple configuration as the feeding line can be ignored in the calculation for the beam scanning. Moreover, the phase shifters can be placed in different positions such as before power dividers or directly before a single antenna element. In this thesis, microstrip power dividers by quarter wave transformer are used for the implementation of the feeding network. Figure 5.2 shows the power divider structure with an input impedance of 50 Ω. In order to divide power evenly and without reflection, we needed two parallel 100 Ω lines. To match the feeding to 50 Ω, λ/4 transformer lines were placed between them. The line impedance of the quarter wave length can be calculated by:

$$Z_0 = \sqrt{Z_i \times Z_L} \tag{5.1}$$

where $Z_i$ is input impedance and $Z_L$ is load impedance. In our case, $Z_0$ is 70 Ω. There is no restricted length for the 100 Ω line. Thus, it can be virtually minimized to zero.

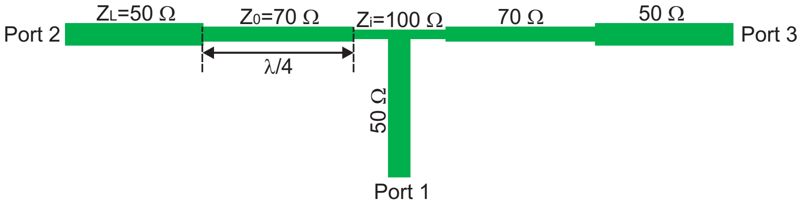

**Figure 5.2:** Microstrip power divider by quarter wave transformer

## 5.2 Two-Dimensional Phased Array Antenna

In this section, the two-dimensional phased array antenna is presented, which consists of sixteen radiating elements $(4 \times 4)$. The prototype has been designed and built to operate at 12 GHz. Each radiating element consists of a phase shifter and an aperture coupled microstrip patch antenna. The left-handed phase shifter presented in section 4.4 is used for controlling the phase. The corporate microstrip feed network using quarter-wave transformers distributes the power equally to the sixteen branches. The phase shifters are placed in the corporate feed network after the power dividers. The circuit of the phased array antenna consists of a RF feeding, a DC biasing network, phase shifters, and antenna elements. Figure 5.3 shows the layout and layer order of the array. The distance between antenna elements is 1.75 cm $(0.7\lambda)$ in order to achieve high directivity and low half power beam width. The phased array antenna consists of three conductor layers. In the following section, each layer is explained in greater detail:

- The bottom layer is patterned on the top of a $(70 \times 70\,\text{mm}^2)$ alumina substrate and consists of three components: the feed network, phase shifters, and the control network. The DC biasing network is connected to the phase shifters to offer the necessary voltage and to control their phase independently for beam steering. The biasing network is connected by 20 µm lines. The narrow line width serves to increase the resistivity and inductance of the biasing lines ensuring that the influence on the functionality of the phase shifters is reduced. Implementing the DC network in the same photolithography process as the phase shifters and the feeding network is an advantage to avoid another board layer for DC routing, which would have made the manufacturing more complex.

- The middle and top conductor layers consist of the apertures for coupling and the patch antennas, respectively. The left-handed phase shifters have radiations which couple to the patch antennas, if they are implemented in the same plane. Thus, an aperture coupled microstrip patch antenna technique is used to implement the patch antennas and phase shifters in two different planes. Moreover, this type of antenna can reach a wide bandwidth and has a small variation of the radiation pattern over the operating frequencies.

  The antenna element requirement for a phased array antenna should have a adequate gain, wide bandwidth, and smaller size. Since the phase shifter is not a resonant structure, it usually is wide band. Therefore, using a wide band antenna element would give the possibility of an overall wide band phased array. A conventional patch antenna has a narrow bandwidth, which can be enhanced through different techniques [57]. In a multilayer configuration, the patch is placed over different dielectric substrates which are stacked atop each other as in the aperture-coupled technique. Figure 5.4 shows an aperture coupled microstrip patch antenna as an indirect technique for exciting the patch. The feed line is on the bottom side of the first substrate and the other side involves a ground plane consisting of the apertures for coupling. In this case, radiation losses can be reduced by using a high permittivity dielectric for layer one. The second substrate, which is thicker with lower dielectric constant, consists of the patch antenna. This multilayer configuration can reach a wide bandwidth and has a small variation of the radiation pattern over operating frequencies [77]. On the other hand, there are two limitations for this method: increased structure height and aperture coupling backward radiation, which should be considered in the system design.

  Figure 5.4 shows the dimension of the microstrip slot antenna at 12 GHz. The first substrate is alumina ($\varepsilon_{r1}$=10) and the second one is roger 4003 ($\varepsilon_{r2}$=3.55). By adjusting the open stub past the slot to a length of $\lambda$/4, the maximum H field in the slot is achieved at the center operation frequency (12 GHz). In the CST full wave simulation, the patch antenna antenna shows -10 dB impedance bandwidth of 10% and a broadside radiation pattern with realized gain of 6.2 dBi at 12 GHz.

### Realization of the Proposed Phased Array Antenna

The bottom electrode was patterned as shown in section 4.4 for a left-handed phase shifter by a single photolithography process on top of the alumina substrate which was covered by the inkjet-printed BST film on the area of the IDC varactors. In an extra photolithography step, the middle layer was later realized on the other side of the alumina substrate, which consists of the slots for the antenna feeding and serves as a ground plane of the microstrip lines and patch antennas.

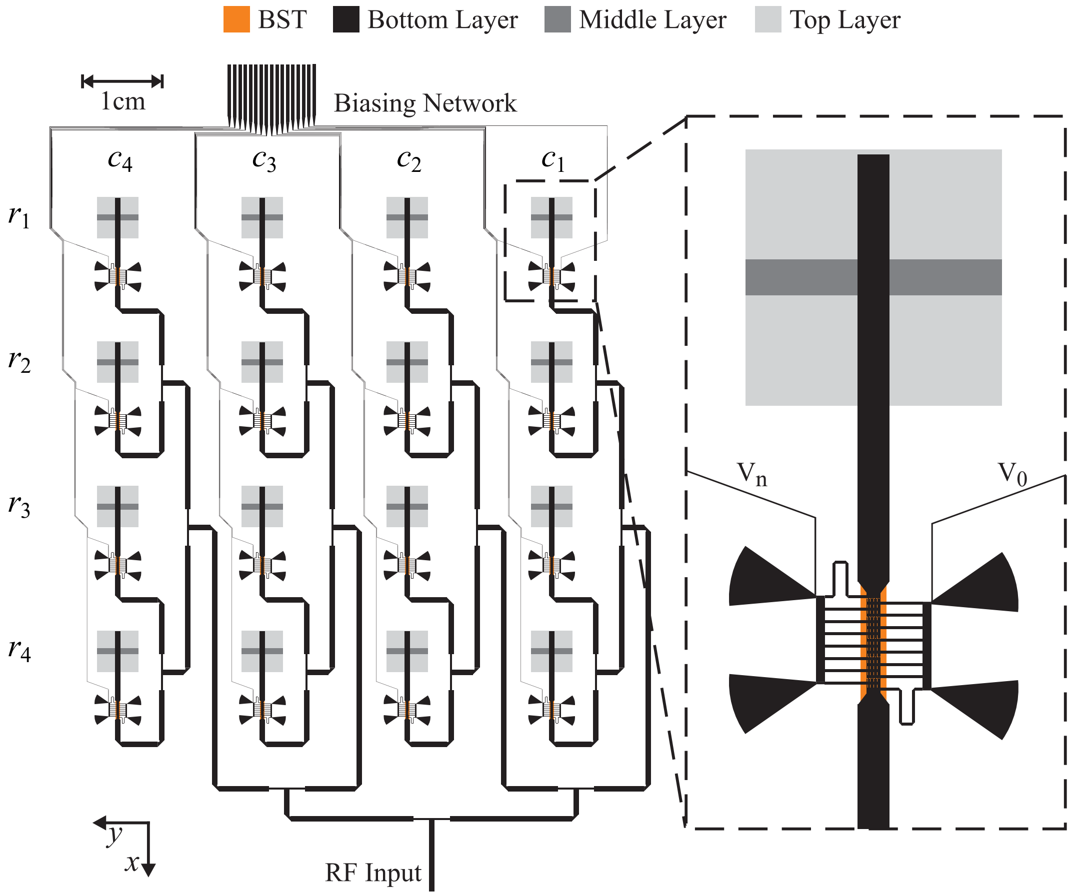

**Figure 5.3:** The layout of the two-dimensional phased array antenna consisting of sixteen elements. It implemented in three conductive layers. $r_i/c_i$ ($i \in \{1,2,3,4\}$) are referred as elements where the bias voltage is applied (rows and columns).

In a separate photolithography process, the top layer consisting of the patch antennas was created on top of the roger substrate. In the next step, two substrates were stacked onto one other by using a fixture. Throughout this entire process, the alignment of the different layers was fundamental in the reduction of positioning tolerances. In each step, alignment marks were used to position the second layer. Finally, two substrates were stacked by an aluminum fixture. Figure 5.5 shows the front and back of the completed phased array antenna panel. The 50 Ω SMA male connector was used for feeding the microwave power to the tip of the microstrip line feed and a 21-pin DC connector was used for the supply of the control voltages.

## Measurement Results

Figure 5.6 illustrates the measured performance (reflection coefficient and gain) of the antenna, which shows the bandwidth of the array. The response shows a good match with VSWR below 2:1 across 1.2 GHz from 11.8 to 13 GHz in the untuned state (0 V). The gain of the phased array antenna reaches above 8 dBi at the frequency band ranging

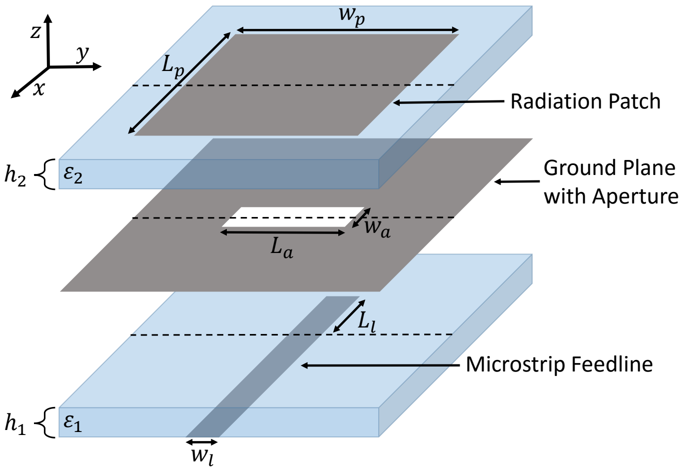

| | (mm) |
|---|---|
| $W_p$ | 5 |
| $L_p$ | 5 |
| $W_a$ | 1 |
| $L_a$ | 4 |
| $W_l$ | 0.615 |
| $L_l$ | 2.4 |
| $h_1$ | 0.635 |
| $h_2$ | 1.524 |

**Figure 5.4:** An aperture coupled microstrip patch antenna designed to operate at 12 GHz.

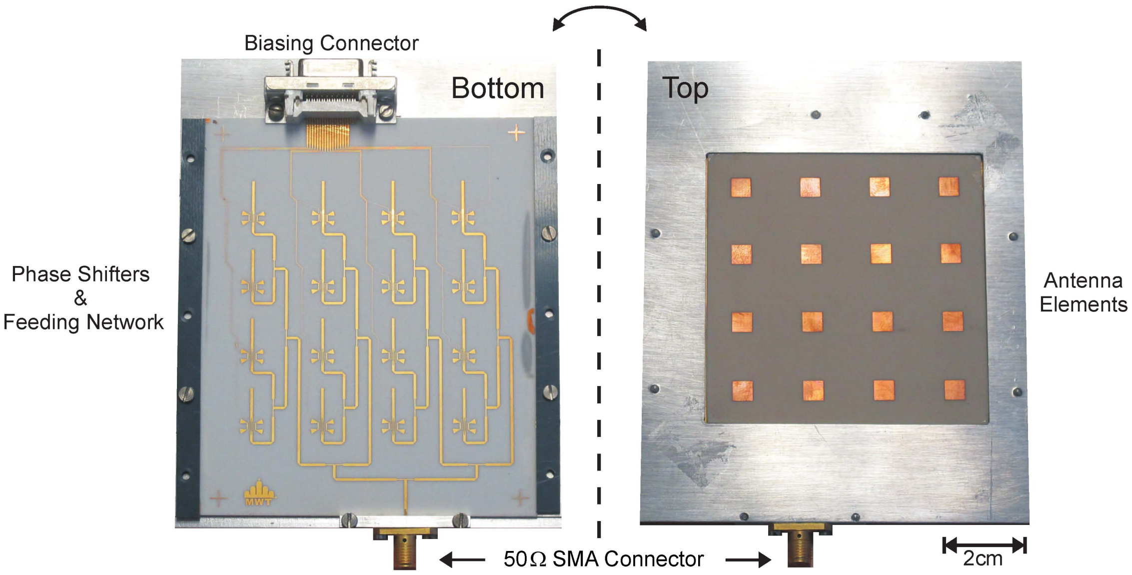

**Figure 5.5:** Photographs of the two-dimensional beam-scanning phased array antenna.

from 11.9 GHz to 12.8 GHz. The measurement results shows a realized gain of 8.1 dBi at 12 GHz. In comparison to the simulation results of the far-field pattern, where losses of the feeding network are not included, measurements show a difference of 11.1 dB for realized gain due to the power loss in the feeding network and phase shifters. In the maximum tuned state for E-plane (zx-cut)/H-plane (zy-cut), the biasing voltages are applied as following: $r_1/c_1$=0 V, $r_2/c_2$=60 V, $r_3/c_3$=120 V, and $r_4/c_4$=180 V (figure 5.3

and figure 5.4). The array responses show increase of the reflection coefficients because of the scanned angle and mutual coupling between the radiating elements.

The fabricated phased array antenna far-field pattern was measured in an anechoic chamber. The simulated and measured pattern on E- and H-plane are presented in figure 5.7 at 12 GHz. To simulate beam scanning a fix differential phase between radiating elements is assumed, which is achieved in measurement by applying bias voltage to the phase shifters. The simulation has been carried out for the $\Delta\varphi = 0\,°$ and ± 116 ° phase difference between the antenna elements in rows/columns. The array shows 19.2 dB directivity and a half power beamwidth of 18 ° in the untuned state (0 V).

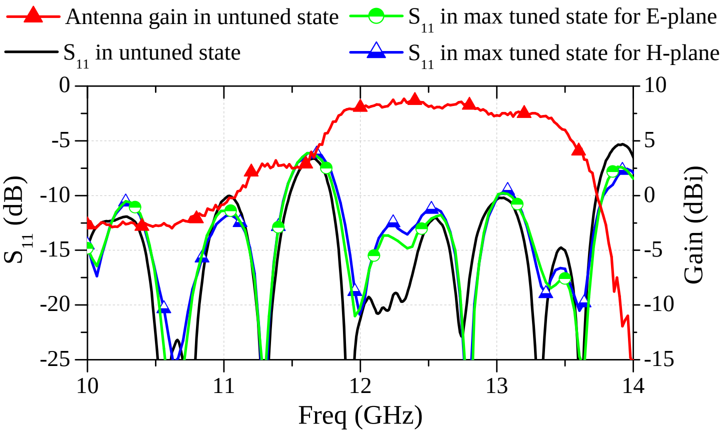

**Figure 5.6:** The reflection coefficients and gain of the two-dimensional array. Note that the phased array antenna was closely matched to 50 Ω at the design frequency (12 GHz).

The achieved maximum phase shift for 180 V biasing voltage is expected to be 350 ° by comparing with steered main beam in simulation (figure 5.7), which is in the range of the measured phase shift of the single phase shifter in figure 4.14(d). The measurement result shows continuous beam scanning in the E- and H-planes. The antenna gain is reduced by increasing the beam scanning angle. Based on the half-power beamwidth (HPBW) direction of the array main beam, the beam-scanning range reaches up to ± 25 ° in both planes. Because of the array factor and mutual coupling between antenna elements, the side lobe level (SLL) increases to the maximum values of ≈-3 dB for E-plane and ≈-5 dB for H-plane, when raising the bias voltage (phase shift).

The result of the presented planar array based on left-handed tunable phase shifters can be summarized as follows:

- The presented array shows the functionality of the inkjet-printed BST thick film for implementation of the planar phased array antenna. The array steers the main beam up to ± 25 ° in both E- and H-planes. The utilized tunable phase shifter has a high FoM and a compact structure, which is suitable for 2D planar array.

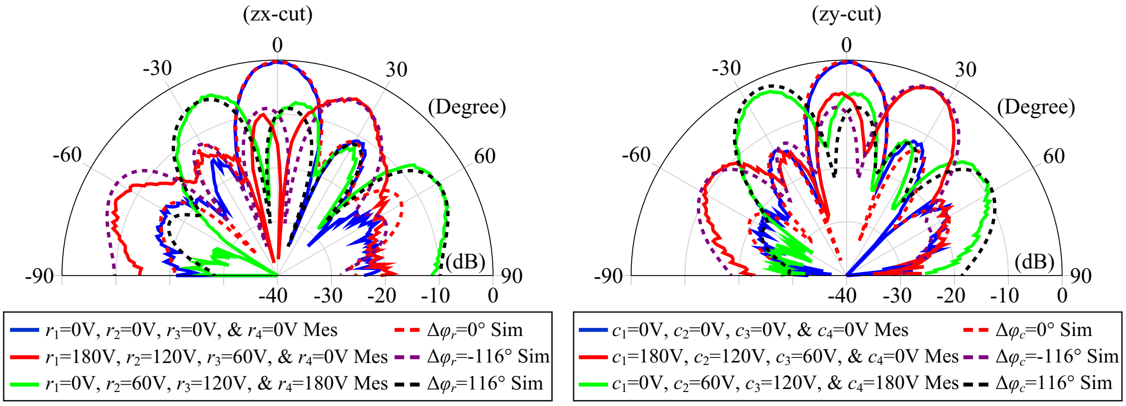

(a) (b)

**Figure 5.7:** Simulated and measured normalized far-field pattern of the two-dimensional phase array antenna at 12 GHz in the (a) E- and (b) H-plane.

- Using the selective inkjet printing method reduces the extra loss for the non-tunable elements in the feeding network and phase shifters, since the BST layer is just printed below the IDC varactors.
- The biasing network is implemented in the same photolithography process as the phase shifter, which reduces the fabrication steps.

## 5.3 Phased Array Antenna Based on Fully Printed Phase Shifters

This section presents a novel approach for electronically steering the beam of a phased array antenna by utilizing fully print phase shifters at S-band. The phased array consists of four microstrip patch antenna elements and phase shifters, as well as a four-to-one corporate feed network. For the phase shifters, as key components in the circuit, a microstrip loaded-line topology was chosen by employing fully-printed MIM varactors (section 4.5.1). A simple biasing concept was implemented for controlling the phase shifter. Figure 5.8 presents the layout of the proposed one-dimensional phased array antenna. It consists of three sections:

- Feeding network: The feeding network divides power equally between branches. For distributing the input signal, a common microstrip power divider is used. The feeding network is optimized for 3 GHz on top of the rogers 4003 with a thickness of $0.8\,\mathrm{mm}$.
- Phase shifters: Each branch was equipped with a phase shifter to individually modify the phase for each antenna. The fully printed loaded line phase shifter with microstrip ports, as presented in section 4.5.1, was used for phase tuning. It has a phase shift of $274°$ and a maximum insertion loss of 7.3 dB at 3 GHz.

- Antenna elements: The antenna elements used in this study are slot-fed microstrip patch antennas designed to operate at 3 GHz. They consist of three conductive layers, which are fabricated on two rogers 5880 substrates. The first substrate is 0.5 mm thick and, in order to increase the bandwidth of the antenna, a thick substrate has been used between the slot and circular patch with 6.4 mm thickness. Moreover, the H-shaped slot is more broadband than a normal rectangular slot with regard to coupling. Table 5.1 shows the dimension of the design. The broadside radiation pattern of the single patch antenna shows a gain of 6.5 dBi and a bandwidth of 14% in simulation.

**Table 5.1:** Dimensions of the single patch antenna designed in mm.

| Patch Diameter | Slot length | Slot width | H-Slot length | H-Slot width | Open Stub length | Open Stub width |
|---|---|---|---|---|---|---|
| 29 | 13 | 0.5 | 2 | 2.5 | 8.5 | 1.15 |

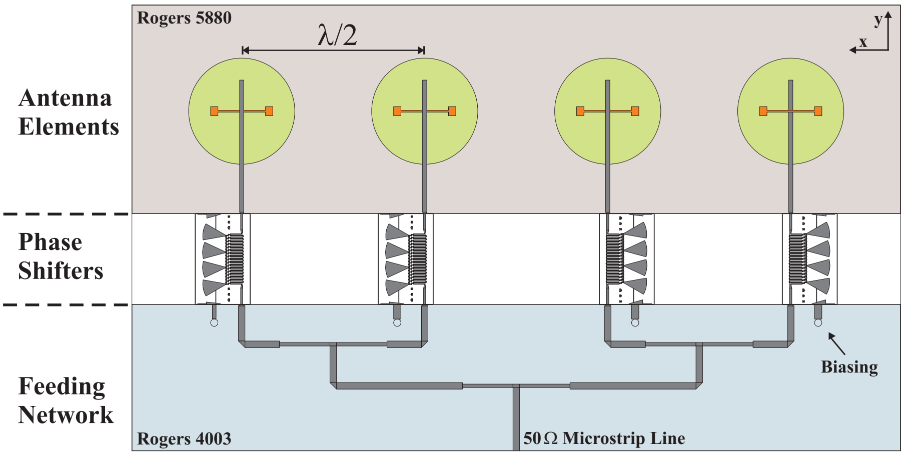

**Figure 5.8:** Layout of the proposed one-dimensional phased array antenna.

The insertion loss variation of the phase shifters in both tuned and untuned states changes the maximum array factor value in different beam steering states. For instance, if there is a 3 dB difference between the maximum tuned and untuned states of the phase shifter for 270 ° phase shift, it increases the maximum gain of the antenna by 3 dB in comparison to the untuned state (without phase shift). Therefore, it needs to compensate for this variation in order to have constant gain for steered beam in different angles. This can be achieved by applying the same voltage value to the phase shifters for 0 ° beam direction. With this method, the insertion loss of the phase shifter can be controlled and a constant gain in beam steering is achieved.

### Simulation and Measurement Results

Figure 5.9 illustrates the photograph of the complete phased array antenna. The distance between the antenna elements is 5 cm ($\lambda$/2). Overall, the array was 12×21 cm$^2$. All layers are fixed on the holder and the fully printed phase shifters are connected to the antenna element and feeding network by silver glue. The array clearly had some manual wire jumpers that needed to be installed by the end user. These were necessary for DC routing in order to avoid another board layer, which would have made manufacturing more complex.

The reflection coefficient of the array in an unbiased state (0 V) is illustrated in figure 5.9. It shows a return loss of 16 dB at 3 GHz and a -10 dB impedance bandwidth of 1.6 GHz. The simulated and measured normalized far-field patterns at 3 GHz are shown in figure 5.10 at 3 GHz. The array is simulated and measured in three different tuning configurations with a relative phase difference of 0 ° and ± 90 ° between the antenna elements. This relative phase shift results in a beam tilt of ± 30 °. The main lobe of the four-element phased array antenna shows a good agreement with the simulation. However, the fabrication tolerances of the phase shifters and mutual coupling leads to increased side lobe levels in comparison to the simulation. For a 0 ° phase difference between the elements, a gain of 3.5 dBi was measured at 3 GHz, which includes the phase shifter and feeding network losses. The simulated directivity of the four-element array is 12 dBi and the half power beam width is 23.5 ° with 0 ° phase difference in the EM simulation software, indicating that the total insertion loss of the phase shifters and feed network is 8.5 dB. The presented phased array successfully demonstrates the capability of the thick-film BST technology for a low-cost phased array antenna application.

## 5.4 Phased Array Antenna Based on Low Tuning Voltage MIM Varactors

This section presents a steerable phased array antenna at C/X-band, which is a proper frequency range for satellite communication. The tunable phase shifters used in the design were implementing inkjet-printed BST thick-films with BST MIM varactors and achieved a maximum phase shift of 260 °dB at 8 GHz (section 4.5.2). A dielectric resonator antenna (DRA), fabricated from bulk-glass ceramic, was implemented as a radiating element with a stacked architecture for wide bandwidth and high gain.

### 5.4.1 The Rectangular Dielectric Resonator Antenna

The patch antennas suffer from high loss in the gain when scanned away from the broadside direction and serve as frequency limiting components (in terms of frequency behavior). A stacked DRA has therefore been investigated as the phased array element in this

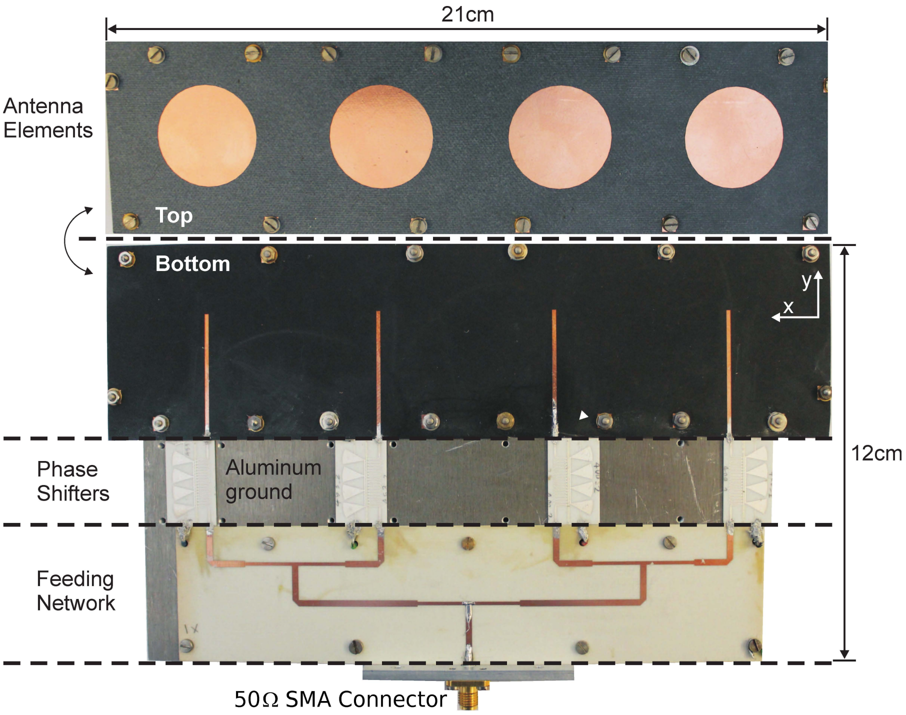

**Figure 5.9:** Photograph of the phased array antenna based on printed phase shifters.

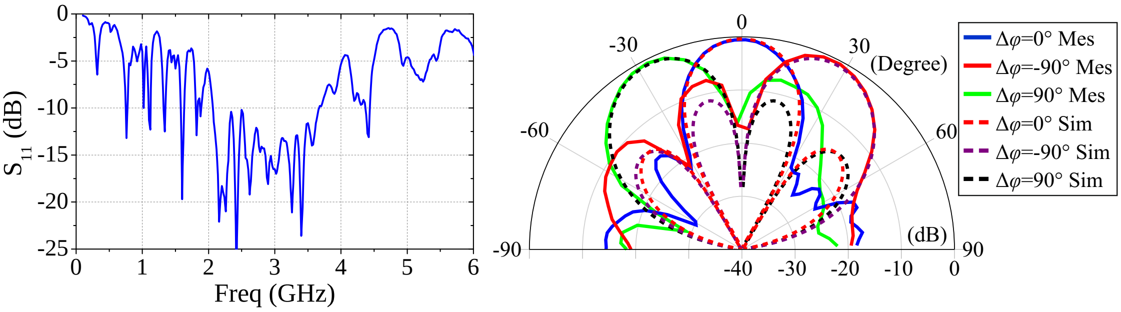

**Figure 5.10:** The reflection coefficient of the phased array in the unbiased state 0 V (Left). The simulated and measured radiation pattern of the four-element phased array antenna normalized to broadside at 3 GHz (Right).

design to achieve a wider bandwidth. DRAs are a kind of antenna, where high permittivity materials are used as the resonant element and can be designed to operate over a wide range of frequencies. The DRA antennas are known for having better bandwidth, low surface waves, low loss (high-radiation efficiency), and are smaller in size when high permittivity materials are used [78, 79]. Moreover, different feeding mechanisms can be used for a DRA. The DRA resonant frequency is defined according to the resonator dimensions at the constant relative permittivity $\varepsilon_r$.

For the design and fabrication of the DRAs as radiating elements for array, the recent investigation of Mehmood et al. [80] in the scope of the project Glass Ceramics with ferroelectric and Paraelectric Phases for Microwave Antennas (GLACER) is used. These elements employs DRAs made from bulk-glass ceramic material in contrast to the usually available sintered ceramics. This material has been developed by Schott-AG as a low loss and high permittivity dielectric. The intrinsic zero porosity, high quality surface finish, and homogenous end product after ceramization are advantages of this new material in comparison to the conventional sintered ceramics [81]. A relative permittivity of 33.4 and loss tangent of 0.0016 at 7.3 GHz were measured with the Hakki-coleman method for the glass-ceramic material. The feasibility of bulk-glass ceramic material has already been proven in single and array configuration for antenna applications [82].

The main dimension of a DRA is related to $\lambda_0/\sqrt{\varepsilon_r \cdot \mu_r}$, where $\varepsilon_r$ and $\mu_r$ are the relative permittivity and relative permeability of the DR material, respectively. $\lambda_0$ is the wavelength in free space at the resonant frequency. The main dimension of a DRA is proportional to $\lambda_0/\sqrt{\varepsilon_r}$ for a dielectric material ($\mu_r$=1). DRA can be fabricated in various shapes. In this research, rectangular shape DR is chosen. To analyze the rectangular DR, the dielectric waveguide model is used [83]. For an isolated rectangular dielectric resonator, the TE and TM modes are considered. However, only TE modes are excited for a DRA mounted on a ground plane. The TE modes can occur along three directions (x, y, and z). For a rectangular DR with dimensions order of $\delta x > \delta y > \delta z$, the $\mathrm{TE}^{\mathrm{z}}$, $\mathrm{TE}^{\mathrm{y}}$, and $\mathrm{TE}^{\mathrm{x}}$ are modes in the order of decreasing resonant frequency [83]. The fundamental mode is the $\mathrm{TE}_{111}$. Exemplary for the $\mathrm{TE}^{\mathrm{z}}_{111}$, the DRA resonance frequency $f_z$ is defined by:

$$f_z = \frac{c}{2\pi\sqrt{\varepsilon_r}} \sqrt{a_x^2 + a_y^2 + a_z^2} \tag{5.2}$$

where $c$ is the speed of light in vacuum. $a_x$, $a_y$, and $a_z$ are wavenumbers [83], which are calculated by:

$$a_x = \frac{\pi}{\delta x}, \quad a_y = \frac{\pi}{\delta y}, \quad a_z \tan(a_z \delta z/2) = \sqrt{(\varepsilon_r - 1)a_0^2 - a_z^2} \tag{5.3}$$

where $a_0$ denotes the free-space wavenumber related to the resonance frequency and is given by:

$$a_0 = \frac{2\pi}{\lambda_0} = \frac{2\pi f_r}{c} \quad , \quad a_x^2 + a_y^2 + a_z^2 = \varepsilon_r a_0^2 \tag{5.4}$$

### 5.4.2 Phased Array based on Dielectric Resonator Antennas

The proposed phased array antenna consists of a feeding network, which is connected to the four branches of the 1×4 array. Each branch has a phase shifter as a controlling element and an antenna element. The configuration of the 1×4 array is shown in figure 5.11. As discussed above, the four stacked DRAs reside on the top substrate, which is rogers 4003. The distance between each element is $0.45\lambda$. The ground with H-shaped slots is on the bottom of the top substrate. The BST lines (pink color) were printed in the middle layer of the phase shifters. The microstrip and bias lines were patterned by photolithography on the bottom alumina substrate. The 20 µm thin bias lines were connected to the four phase shifters through radial stubs as a RF block which reduces the influence of the biasing lines on the RF propagation.

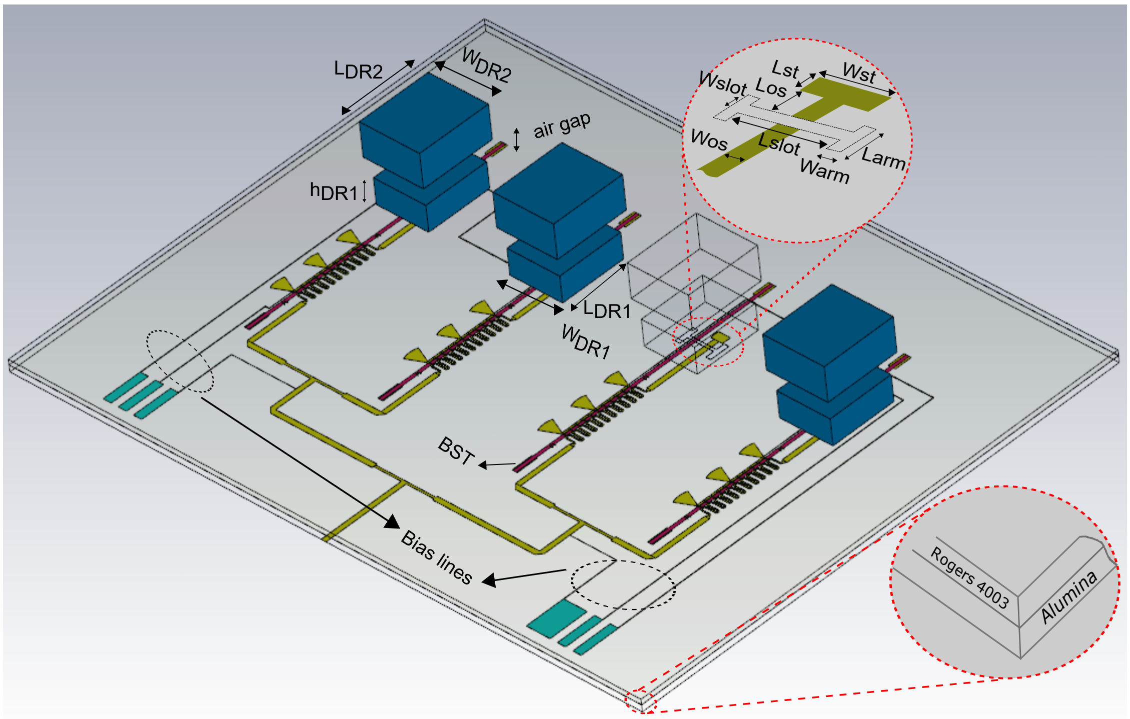

**Figure 5.11:** Layout of the four-element DRA phased array.

The size of rogers 4003 substrate is 6×10 cm$^2$ and it's thickness is 0.508 mm. By choosing the thicker substrate, the coupling is decreased. Using alumina (0.635 mm thick) as the lower substrate with microstrip line is also beneficial, as it will reduce the radiations from the line itself in the lower half space or back radiations. Four stacked DRA elements were placed on top of the slots. The two dielectric resonators (DR) were placed on top of the slot. The top DR length is 8.7 mm, the width 7.7 mm, and the height 3.3 mm. The two DRs are separated by a rohacell foam with a thickness of 2 mm and a relative permittivity of $\varepsilon_r \approx 1$. A gap between the DRs enhances the impedance bandwidth. The lower DR has a length of 7.7 mm, a width of 6.7 mm, and a height of 2.5 mm. The H-slot and open stub dimensions are obtained by optimization during the simulation in CST. The bandwidth of the antenna is increased by adding the stub at the end of microstrip line ($L_{st}$ and $W_{st}$). Table 5.2 shows the dimensions of the above design for the DRA's feeding.

**Table 5.2:** Dimension of final designed aperture slot and feeding stub in mm.

| $L_{\text{slot}}$ | $W_{\text{slot}}$ | $L_{\text{st}}$ | $W_{\text{st}}$ | $L_{os}$ | $W_{os}$ | $L_{\text{arm}}$ | $W_{\text{arm}}$ |
|---|---|---|---|---|---|---|---|
| 3.3 | 0.35 | 1 | 1.5 | 1.6 | 0.613 | 0.6 | 2.3 |

### Dielectric Resonator Antenna Simulation and Measurement Results

The optimized design of the rectangular DRAs was fabricated and implemented on a smaller ground plane as it was presented by Mehmood et al. [80]. The dielectric resonators were glued into each other and the substrate. Instead of the air gap, a rohacell substrate was glued between two dielectric resonators. The antenna reflection coefficient was measured with a VNA. The validation of the wide band performance is illustrated in figure 5.12. The measured reflection coefficient is compared with the simulation result using CST at a frequency range of 6 to 12 GHz. In the simulation, three resonant frequencies at 8 GHz, 8.7 GHz and 9.2 GHz can be recognized. These resonances appear because of the two DRs and the slot. The -10 dB impedance bandwidth of the proposed antenna is 23.5% in the simulation and around 20% ranging from 7.4 to 9 GHz in the measurement. The measurement reflection coefficient exhibits a lower bandwidth and a shift towards lower frequencies. The fabrication tolerances such as alignment error of the dielectric resonators, gluing them on the substrate, and an imperfect resonator could cause a difference between two curves.

The normalized radiation pattern with a fairly wide beamwidth single main lobe is shown in figure 5.12. The simulated and measured radiation pattern fit quite well to one other. The single DRA element was measured to have a gain of 7.23 dBi at 8 GHz, with a simulated radiation efficiency of 96%. This indicates that the $1\times4$ array configuration of such DRA elements should theoretically allow for a gain of almost 12 dBi.

### Phased Array Antenna Fabrication and Measurements

The fabricated prototype is shown in figure 5.13. As a fixture of the structure, an aluminum plate was placed on top of the structure. It has no influence in the final result as is proved by simulation. The impedance bandwidths for the prototype were measured between 5 to 11 GHz by a network analyzer in an untuned state (0 V). The variation of the reflection coefficient versus frequency is illustrated in figure 5.14. As expected, the array impedance is matched around the target frequency band. The -10 dB impedance bandwidth is observed from 7 to 8.4 GHz.

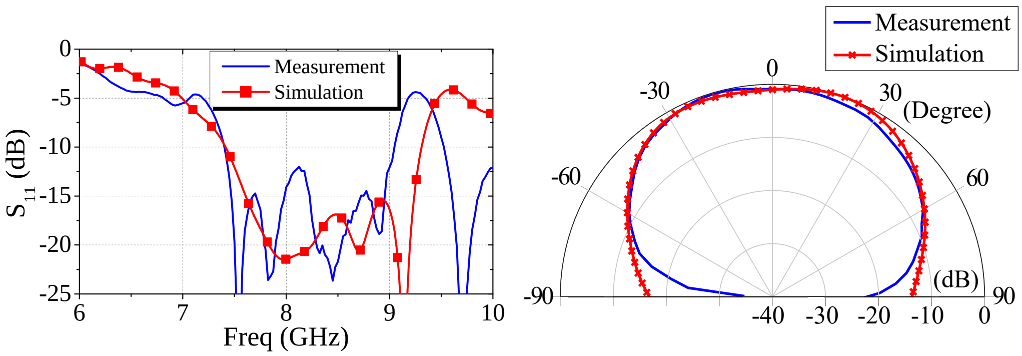

**Figure 5.12:** The simulated and measured reflection coefficient (left) and normalized far-field pattern (right) of the rectangular DRA.

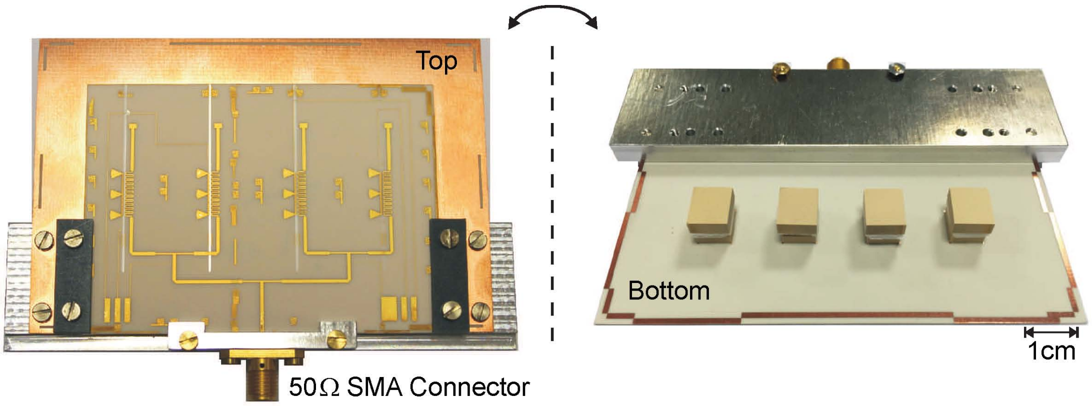

**Figure 5.13:** The photograph of the manufactured prototype of the four-element phased array antenna at C/X-band.

The far-field pattern measurements were performed in an anechoic chamber to evaluate the beam steering. Figure 5.14 depicts the measured and simulated far-field pattern at 8 GHz. In the measurement, the broadside beam is obtained when no voltage across the phase shifters was applied. The main beam was steered to ± 30 °, when a differential phase shift of ± 86 ° was applied between each element (simulation and measurement).

The reduction in gain as measured from the power level between the broadside and ± 30 ° beams is less than 1 dB. The measurement results show a realized gain of 4 dBi for the phased array antenna at 8 GHz due to the power loss in the feeding network and phase shifters. In comparison to the array simulation and single element measured gain, the feeding network, phase shifters, and fabrication tolerances cause a 8 dB insertion loss. In figure 5.14, it can be observed that there is a good agreement between the simulated and measured patterns with respect to the main beam and nulls. Due to an unsymmetrical measurement setup, the side lobe level is different in simulation and measurement. As a result of low mutual coupling between DRAs, the side lobe level increases to the maximum values of ≈ -10 dB by beam steering. This value is lower in comparison to the presented arrays based on patch antennas. Hence, DRAs achieve a better scanning range performance. Although, it has been shown in some investigation [84], that the mutual coupling between patch antennas and DRAs are not too different. It means they should show similar side lobe value. Therefore further investigation needs to be done.

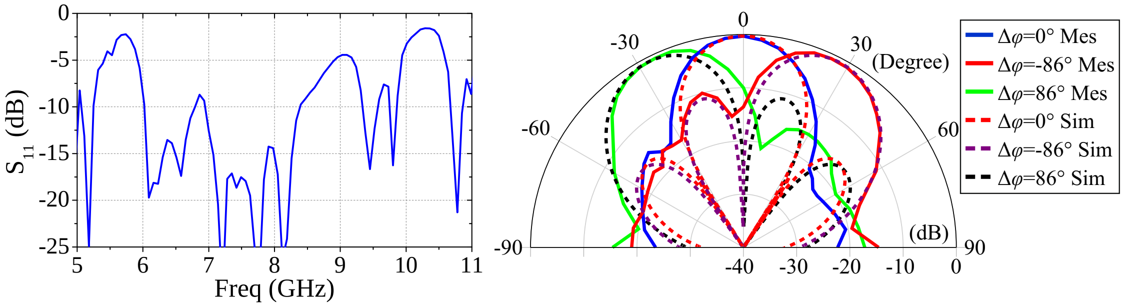

**Figure 5.14:** (left) The measured reflection coefficient of the phased array antenna in an untuned state (0 V). (right) The simulated and measured radiation pattern of the four-element phased array antenna normalized to broadside at 8 GHz

# Chapter 6

# Conclusion and Outlook

Having its main focus on phases shifters, this work encompasses the material synthesis, component fabrication, circuitry design and analysis, as well as the component integration in BST thick-film technologies. In particular, the investigation of the thick film technology as an integrable method for the realization of reconfigurable front ends is presented. The performance of the proposed phase shifters across S-, C-, and X- bands have been analyzed. The feasibility of using these phase shifters in cost-effective phased arrays has been examined. The demonstrated phased array antennas were designed to simplify and accelerate the utilization of one- and two-dimensional beam steering.

One major contribution of this work is a novel approach based on thick film technology , different loaded line phase shifter concepts and left-handed transmission lines were systematically investigated and presented, which show significant improvement in the phase shifter functionality. In addition to the phase shift and losses, other aspects such as the integration and dimension of the phase shifter have been considered with respect to the integration in the planar antenna structures.

In another approach, the selective inkjet printing technique has been investigated. The inkjet printing, as a flexible and fast method, shows a high potential for the fabrication of tunable components. The potential of this technology has been shown by a two-dimensional phased array antenna at 12 GHz equipped with left-handed microstrip phase shifters as a compact structure for beam steering in both azimuth and elevation planes. For the first time, the two-dimensional beam scanning of $\pm 25\,^{\circ}$ based on the BST thick film has been achieved. To reduce the fabrication complexity of phased array antennas, the phase shifters, RF feeding network, and control power network were realized on a single carrier substrate.

Sintering temperatures below 900 °C for screen- and inkjet-printed layers have been investigated in cooperation with the Material Process Technology group at Karlsruhe Institute of Technology (KIT). The reduction in sintering temperature makes it possible to implement MIM varactors with low-defect bottom metallic electrodes and the integration of controllable thick-film dielectrics in LTCC multilayer systems. The fully printed tunable components have introduced for beam steering of the antenna at 3 GHz as a simple and low-cost method. The fully printed phase shifters show a FoM of more than

70 °/dB, which is significantly higher than the FoM of previously reported components. As a proof of concept, this structure was successfully integrated in LTCC method, which is an established technology for the implementation of the low-cost and highly integrated multilayer modules.

Given the fact that the available DC voltage is very limited in many real-world applications, one target of this work was to lower the necessary biasing voltage of tunable components. This goal is accomplished by means of our inkjet printing technique. The aforementioned methods for the reduction of sintering temperature and the development of inkjet printing method yield a MIM varactor, which aims to reduce biasing voltage and improve the quality factor. A tunability of 46% for MIM varactor was achieved by applying a DC voltage of 50 V. This varactor was implemented in a loaded line phase shifter. The properties of the phase-shifter with a FoM/V of 0.88 °/(dB·V) at 8 GHz have achieved the best performance so far for the ferroelectric thick-film varactors. The performance of the phase shifter has been shown for a linear array antenna at 8 GHz. Additionally, the proposed array is equipped with dielectric resonator antennas as compact and high-efficiency radiating elements with low mutual coupling. The realized array covers scanning range of ± 30 °.

On the basis of the findings of this work, the following outlook is foreseeable:

- The one- and two-dimensional demonstrated phased array antennas can be extended due to the compact dimensions of the phase shifters in a simple approach. Higher gain and directivity (narrow main lobe antenna) is demanded for satellite communications. This is easily feasible through the use of a number of smaller sub-arrays such as those presented in this work.

- The phase shifter based on LTCC technology as well as the phase array antenna utilizing fully printed phase shifters have been demonstrated at 3 GHz. A promising prospect for these developments would be the realization of phased array antennas through LTCC technology.

- The quality factor of the proposed MIM varactors based on screen and inkjet printings can be improved, since the IDC varactors reported quality factor is higher [6]. By increasing the varactor quality factor, there is a potential to increase the FoM of the phase shifters. This should be done by improving the film quality and reducing the conductor loss, which can be significantly enhanced with additional materials and process optimizations in close collaboration with materials scientists. This will be the subject of future research projects.

- By printing high resolution silver lines, it is possible to reduce capacitance and reach higher frequencies for fully printed components (less than 100 µm line width). For long-term reliability, one has to consider the metal-oxide interface, to prevent interdiffusion.

- Miniaturization and reduction of power consumption are the two dominant trends in a number of industrial research areas such as in telecommunication. The vacators based on BST thin film technology offer a viable solution for realization of the both mentioned criteria. In comparison to the thick film technology, the thin film can potentially be tuned by low voltages. In collaboration with the Advanced Thin Film Technology (ATFT) group at TU Darmstadt, thin film approach has been used to fabricate ferroelectric varactors based on highly conducting oxide bottom electrode. The unprecedented epitaxial growth of the thin film heterostructure has the potential for developing of miniaturized BST thin film varactors for low-voltage applications. As it is detailed in Appendix. A, based on the novel approach for BST thin film, epitaxial MIM varactor heterostructures with low defect density show high commutation quality factor $K$ at low tuning voltages ($< 8\,\mathrm{V}$). Such varactors are suitable for a variety of applications including the on-the-go applications. In particular, they can be utilized in the reconfigurable front-ends. For integration of such MIM varacotrs into microwave circuits, the design and structuring of varactors need to be optimized. This research has lead to the following project with the goal of fabricating a first prototype:

  ”ALOVA (engl. all-oxide varactor, Varaktoren basierend auf der Kombination leitfähiger und ferroelektrischer Oxide für Anwendungen in der Mikrowellentechnik)”

# Appendix A

# Thin Film Ferroelectric Varactors

Thin film technology usually relies on the growth of the material of interest on top of a substrate. Different techniques such as pulsed laser deposition (PLD), radio frequency (RF), magnetron sputtering, and molecular beam epitaxy (MBE) are commonly used for the fabrication of thin films [34, 85]. In combination with photolithography, structuring of the sample is possible to achieve high resolutions for patterned structures. Additionally, the ion milling etching is commonly used to remove thin films from the unwanted areas and to pattern the deposited sample into the required configuration.

The PLD technique is a versatile and flexible method which allows growth of different layers and compositions through the use of a focused pulsed laser beam. However, this technique is not a cost-effective process for mass production, as it requires large machinery and vacuum processing [10]. Figure A.1 shows the PLD setup in an ultra-high vacuum (UHV) chamber, used for depositing BST on top of a substrate [10, 11]. In this process, the focused laser beam has a 45 ° angle with respect to the target (the material which must be deposited). By means of laser pulses, the species are ablated from the target material, transferred to the surface of the substrate in a plasma plume, and deposited on top of the substrate. The growth temperature, substrates crystallographic structure, processing parameters, and deposition methods are the factors that can influence the properties of the thin film [85].

In thin-film ferroelectric varactors, both the tunability and loss of the component are determined by the contributions of the ferroelectric layer, conducting electrodes, and ferroelectric/electrode interfaces. Each of the underlying layers are decisive in the crystal structure and, thus, the properties of the next layer [86, 87]. Furthermore, the misfit strain of the dielectric material with the underlying layer determines the change in the dielectric properties of the BST layer [88]. As mentioned, losses of ferroelectric varactors at microwave frequencies depend on the microstructure of the dielectric layer [89]. The dielectric permittivity and tunability of the thin film varactors are significantly smaller than that of the fabricated varactors from the single crystal materials of the same composition. The reduction may be caused by a number of reasons, including a mismatch between the crystal lattices, defects in the ferroelectric film, a dead layer formation at the interface layers, and so on [85].

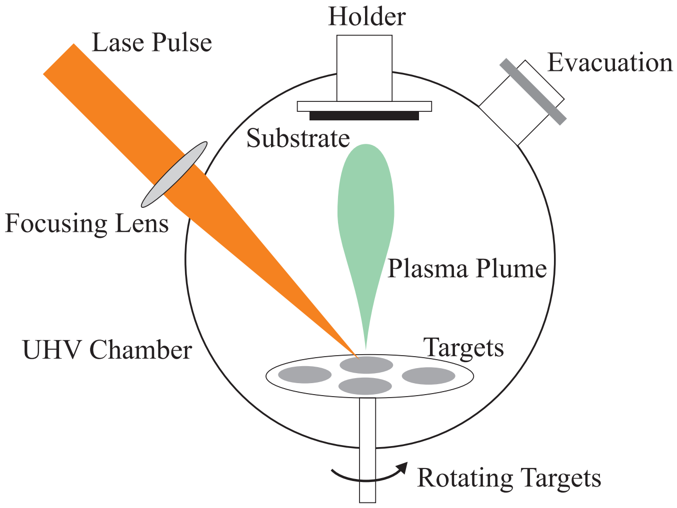

**Figure A.1:** Schematic of a pulsed laser deposition (PLD) system used for thin-film deposition.

To reduce the loss of the varactor, it is necessary to select a conducting electrode material which would form a high barrier height with the ferroelectric material and not interact chemically with the dielectric material [85]. The conductor layer should have a good crystallographic match with the substrate to allow for growth of high quality epitaxial BST thin films. Moreover, the electrode material needs to have low resistivity and permeability. Even the best varactors with a highly tunable BST thin film layer and conductive metal electrodes (Au, Pt, and Ni) suffer from high losses due to microstructural defects of the polycrystalline BST films and the dead layer at the interfaces. The metal electrodes have a low resistivity at room temperature but have a very large lattice mismatch with BST. The quality factor of 100 at 10 GHz is demonstrated in the BST varactors with the Pt,Au electrode overtaking the performance of the competitive semiconductor varactors [90]. However, due to the defect microstructure of the polycrystalline BST films, the reported values of the electric tunability and quality factor of the thin film BST/Pt,Au varactors are significantly smaller in comparison to those of the single crystal ferroelectric materials.

For this reason, efforts were made to use conducting oxide materials as bottom electrodes, enabling the deposition of a dielectric layer with low defect density and misfit strain (comparable lattice parameters) [91]. The performance of the BST thin film ferroelectric varactors can be significantly raised by improving the microstructure of the BST films [10, 85]. The crystal structure and lattice parameters of the oxide electrodes, if selected correctly, allow for the growth of epitaxial MIM varactor heterostructures with superior quality factor and electric tunability, due to a significantly reduced density of defects in the BST films and smooth interfaces between the ferroelectric and electrode material. Due to smooth interfaces, the BST layer can be very thin (few tenths of a nanometer), suitable for low-voltage tunable microwave applications.

The utilization of the oxide electrode materials promoting the growth of single-crystal-like epitaxial ferroelectric films with fewer defects than in the polycrystalline ones is reported in [61, 92, 93]. Due to the resistivity of more than 100 µΩ·cm of the previously used electrode materials ($SrRuO_3$, $LaSrMnO_3$, and $LaNiO_3$), it was concluded that oxide electrodes are too resistive for proper integration into microwave varactors [56]. The epitaxial oxide electrode $SrRuO_3$ provides superior electric tunability of the BST ferroelectric varactors up to 87%. Nevertheless, the high leakage current and losses are the main problems of the BST varactors with the oxide electrodes [61].

Despite the superior microstructure of the epitaxial BST, the losses of the varactors with epitaxial oxide electrodes are comparable to the losses in the Pt/BST/Pt varactors. The effect can be explained by recalling very high resistivity of the oxide electrode materials in comparison to that of the metal electrodes (Pt). For instance, the resistivities of 270 µΩ·cm have been reported for the $SrRuO_3$ thin films [94] at room temperature. This value is 30 times higher than the resistivity of Pt [85]. Hence, it can be concluded that the losses of the varactors can only be reduced by implementing those oxide materials which allow higher conductivity. Among all perovskite oxide materials, $SrMoO_3$ single crystal is shown to have the lowest electrical resistivity of 5.1 µΩ·cm at room temperature [95], which is twice as high as gold's resistivity ($\sim$ 2.44 µΩ·cm). Moreover, $SrMoO_3$ single crystal has a negligible lattice mismatch to BST crystal. This low resistivity and lattice match show the potential of SMO for implementation in the BST thin film varactors.

### Highly Conducting $SrMoO_3$ Thin Films

A reliable and reproducible processing is imperative for the routine manufacturing of oxide thin-film devices and circuits. In addition to the epitaxial growth of the functional SMO and BST layers, one of the most critical points of the technology is the patterning of oxide thin films and formation of the varactor geometry. Especially for measurement of the resistivity in the microwave range, the patterning of the transmission line is crucial. Oxide thin films are typically patterned using photolithography and wet chemical or Ar ion-beam etching. In this work, the processing of the thin film samples had been done by the Advanced Thin Film Technology (ATFT) group at TU Darmstadt. The patterning and structuring have had done by Nikfalazar (IMP) and Mani (ATFT), and the layout design, measurement, characterization and analysis had done by Nikfalazar (IMP).

For the fabrication of the oxide layer, epitaxial $SrMoO_3$ thin films were grown onto 1 mm thick single crystalline $GdScO_3$ ($5\times5$ mm$^2$) substrates with relative permittivity of $\varepsilon_r$=21 by PLD under an ultrahigh vacuum ($10^{-8}$ Torr), as shown in figure A.2(a). KrF excimer laser with 248 nm wavelength, fluence of 0.5 J/cm$^2$, and a repetition rate of 5 Hz were all used to ablate the dense $SrMoO_4$ pallet used as a PLD target. The thickness (400 nm) of the deposited $SrMoO_3$ film was independently determined with high accuracy from the reflection high-energy electron diffraction (RHEED) intensity oscillations, as well as from the thickness fringes in the X-ray diffraction pattern [85].

In the next step, the SMO layer was covered through the spin coating of a positive photoresist (figure A.2(b)). The photoresist was then pre-baked for one minute per µm

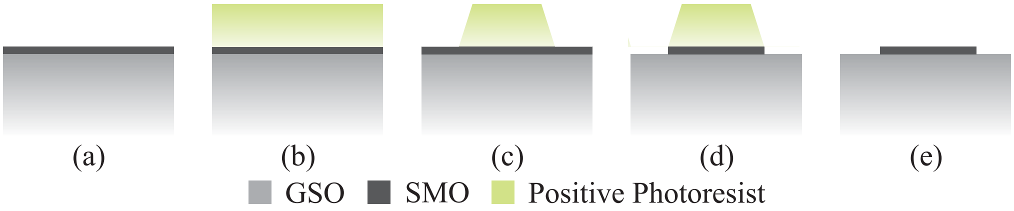

**Figure A.2:** Structuring of the SMO layer by utilizing positive photoresist and wet etching.

thickness at 90 °C on a hotplate. This step is crucial to wards hardening the photoresist before contacting it to the mask. For patterning the structure, precision chromium glass masks were used. By employing the glass mask, a pattern of intense light exposes the positive photoresist. The intense light (ultraviolet) power, wavelength, and exposure time are crucial for the quality of the patterned structure. In the subsequent development process, the exposed area is freed from photoresist and the unexposed areas of the positive photoresist remain intact (figure A.2(c)). In particular cases, a thin layer of the exposed photoresist remains after the development. In this case, oxygen ion etching ($O_2$ plasma) was used to clean the remained photoresist layer.

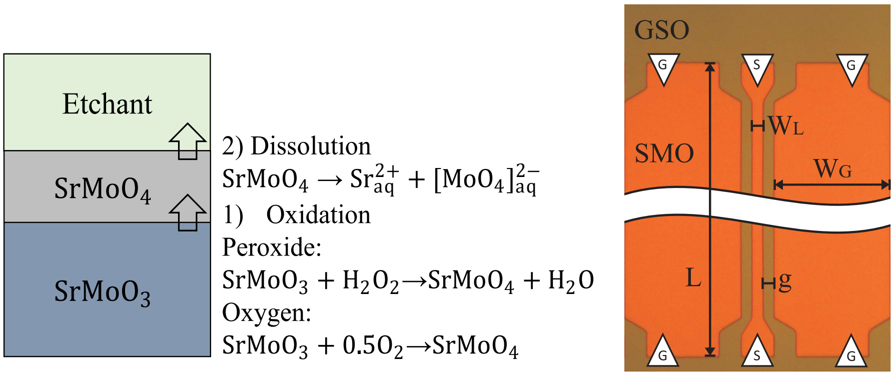

(a) (b)

**Figure A.3:** (a) Scheme of the proposed two-step etching mechanism of $SrMoO_3$ in KOH solution. (b) The fabricated CPW with SMO as a conductor layer on top of the GSO substrate: $W_L$=3 mm, $g$=3 mm,$L$=3 mm, and $W_G$=3 mm.

In this work, a method of chemical wet etching of SMO for thin films with weak alkaline solution (KOH) was developed. SMO is etched in two steps: Primarily through the initial superficial oxidation of the $SrMoO_3$ ($Mo^{4+}$) to $SrMoO_4$ ($Mo^{6+}$). Secondly, the $SrMoO_4$ dissolves in the alkaline etchant, forming molybdate ions and $Sr^{2+}$ (figure A.3(a)).

The addition of an oxidizing agent such as $H_2O_2$ accelerates the $Mo^{4+}$ to $Mo^{6+}$ oxidation and increases the etching rate. By varying the concentration of the oxidizing agent, the etching rates in the range from 100 to 600 nm/min were achieved (appendix A). Such rates are suitable for fast and reliable patterning of any structure with a thick SMO electrode ($\approx$0.5 µm) [85]. During the wet etching process, the photoresist acted as a cover layer. The SMO layer was removed only in the open areas, while the photoresist coated area was isolated from the etchant (figure 3.10(d)). After the wet etching of SMO layer process, the photoresist was completely removed with a solvent, namely acetone and propanol (figure 3.10(e)).

To evaluate the resistivity of the SMO layer, CPWs were patterned by photolithography and wet etching as described above (figure A.3(b)). The CPW lines were contacted by GSG with a 150 µm pitch (Cascade ACP-40-GSG-150, Cascade Microtech) and were measured by a VNA As a reference, a CPW line of Au electrode was realized with a thickness of 140 nm. Figure A.4(a) illustrates the measured and simulated insertion loss of the CPW with Au and SMO conductor layer. Four CPW lines were measured, the results of which were averaged over the entire frequency range. To find the value of the resistivity, an agilent Advanced Design System (ADS) software was employed. In the method of moments (MoM) simulation, all values including GSO permittivity, loss tangent, and geometries were used as constants. The resistivity of the conductor was the variable. In the simulation, the resistivity of the conductor layers were altered to fit with measured data at 10 GHz ($\rho$=28.4 µΩ.cm).

As shown in figure A.4(b), the extracted resistivity values of the Au and SMO layers were optimized by altering the values and matching the transmission line insertion loss ($S_{21}$) of the simulation and measurement over a frequency range between 0.1 and 20 GHz. The resistivity of $\rho_{Au}$=3.52 µΩ·cm and $\rho_{SMO}$=28.4 µΩ·cm resulted in the best fit at 10 GHz. The Au layer showed an almost constant resistivity versus frequency. The SMO layer resistivity value at 10 GHz was 5% higher than the values measured at DC (27.16 µΩ·cm). Such a low resistivity shows high potential of $SrMoO_3$ as a low-loss conductor for implementation in thin film BST varactors for microwave applications.

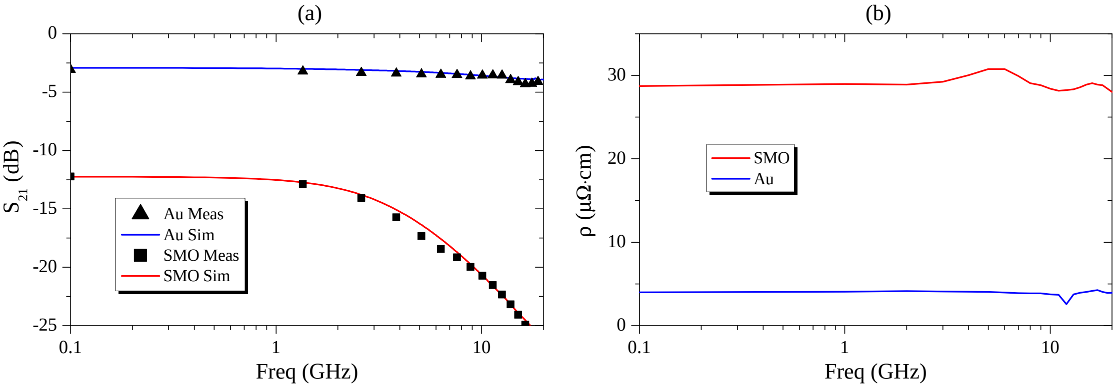

**Figure A.4:** (a) Simulated and measured CPW line insertion loss with Au and SMO conductor layer. (b) The extracted resistivity $\rho$ of the Au and SMO layer versus frequency.

### Thin Film Ferroelectric Varactors Based on $SrMoO_3$ Bottom Electrode

The schematic top and cross-section view of the test varactor structure and the corresponding lumped equivalent circuit are shown in figure A.5. The top electrode structure consists of an inner circle with a diameter $D_{\text{in}}$=20 µm and 30 µm, surrounded by a ring with an inner diameter of $D_{\text{ring}}$=40 µm, and an outer diameter of $D_{\text{out}}$=400 µm.

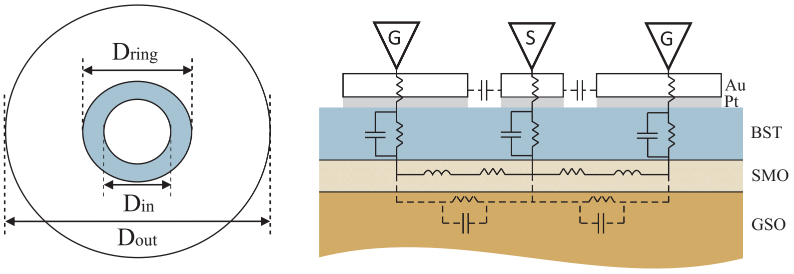

(a) (b)

**Figure A.5:** (a) Top view and (b) cross section of the test structure geometry with denoted positions of the GSG wafer probes. In the lumped equivalent circuit, parasitic capacitances and resistances are illustrated in dashed lines.

Thin-film Au/Pt/BST/SMO varactors with epitaxial BST are fabricated. The SMO bottom electrode (315 nm) and the dielectric layer (BST, 80 nm) with intermediate STO buffer layer are grown on top of GSO substrate by PLD (figure A.6(a)). Following this step, lift-off lithography was performed by patterning the structure with negative photoresist. This step essentially involved the spinning of the photoresist (figure A.6(b)), the pre-baking under 105 °C, exposure and wet chemical development of the resist (figure A.6(c)). The light-exposed area of the negative photoresist is stable to the developer. However, the unexposed area of the negative photoresist is solvable by the developer. The negative photo resist has an undercut after development, which is suitable for the lift-off process.

Later, 20 nm of Pt and 200 nm of Au were deposited by sputtering as a top electrode (figure A.6(d)). The use of a thin Pt layer at the interface with BST allows for the formation of a reproducible Schottky barrier of about 1 eV and leads to a low leakage current of the varactor [96]. The thick Au film has a low resistivity and is used to minimize losses of the top electrode. After the sputtering process, the photoresist covered by Pt/Au layer was removed by the developer (figure 3.10(e)). Figure A.7(a) shows the High Resolution Transmission Electron Microscopy (HRTEM) image of the fabricated varactor. The epitaxial relationship between the deposited layers of the fabricated thin film varactor and the underlying $GdScO_3$ is perfectly visible. A good lattice match between the substrate, STO, SMO, and BST results in a commensurately strained stack of heterostructures, where the in-plane lattices are fully locked and aligned between all of the layers.

### Oxide MIM Varactor: Measurement, Modeling, and Simulation

The reflection measurement was performed on a wafer prober connected to a VNA. The GSG probe with a 150 µm pitch was used to contact the component as shown in figure A.7(b). The biasing voltage (Keithley 2612: Keithley Instruments, Cleveland, OH) was applied by a bias-tee (SHF BT 45B HV200: SHF Communication Technologies

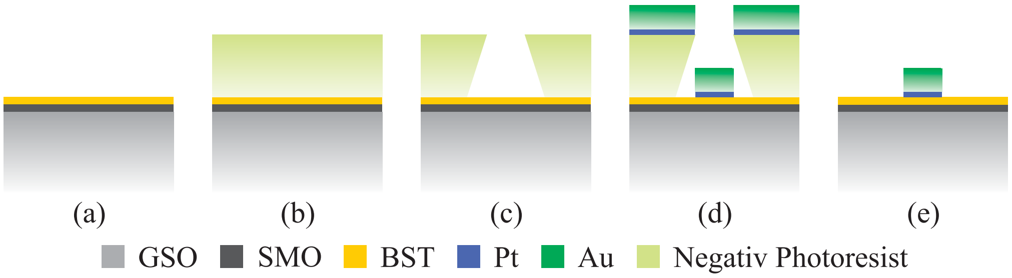

**Figure A.6:** The Pt/Au lift-off process utilizing negative photoresist.

AG, Berlin, Germany) at the 50 Ω RF-port. The reflection coefficient of the varactor structures was measured in the frequency range of 100 MHz to 20 GHz.

Figure A.7(c) shows the BST layer's relative permittivity and the measured tunability $\tau_\varepsilon$ (equation 2.11) of the Au/Pt/BST/SMO varactor. The observed relative permittivity in the BST thin films on SMO ($\varepsilon_r = 180$ in an untuned state) is lower than $\varepsilon_r \sim 1000$ reported in the literature for BST single crystals with the same Ba to Sr ratio. It is assumed to arise from residual strain and point defects (oxygen vacancies) [10]. The BST layer is either within or near the ferroelectric and paraelectric phase transition, as evidenced by weak hysteresis in the relative permittivity $\varepsilon_r(V)$ curve in figure A.7. Interestingly, a 50% tunability is observed at 8 V (1 MV/cm) at 100 MHz. Similar values are typically obtained at bias voltages higher than 20 V for the MIM varactors with Pt electrodes and BST layers thicker than 300 nm [97].

Figure A.8(a) shows the quality factor of the MIM varactor at different biasing voltage/electrical field. The quality factor variation by the biasing voltage reduces at higher frequency ranges, which is showing the increase of contribution of the conductor layer loss. The quality factor of the varactor versus frequency in untuned stated is illustrated in figure A.8(b). At higher frequencies, the losses of SMO (the electrode loss) become dominant. The loss of the conducting SMO has been shown to have weak frequency dependence [85]. At frequencies above 1 GHz, a nearly linear increase of losses over frequency is observed owing to the contribution of the series resistance of the oxide SMO electrode. However, due to the small resistivity of the SMO films (50 µΩ·cm), more than one order of magnitude higher $Q$ values are achieved in the Au,Pt/BST/SMO varactors at frequencies above 1 GHz, in comparison to the previously reported $Q$ values for varactors with oxide electrodes [61]. It can therefore be concluded that, for utilizing high quality factor SMO/BST varactors at microwave frequencies, the thickness of the SMO bottom electrode needs to be increased in order to reduce the series resistance R$_e$ and, consequently, decrease the total losses at microwave frequencies. At low frequencies, quality factor mainly limited by dielectric layer loss [61]. The quality factor at 1 MHz is 135, which resulting in a loss tangent of 0.0074 for the BST film. This value is in a good range in comparison to the reported loss tangent for BST thin film [61, 89, 98].

The frequency dependence of the $K$ of the Au/Pt/BST/SMO varactor is shown in figure A.8(c). The values of $K = 500$ at 1 GHz and $K = 20$ at 10 GHz are obtained. These

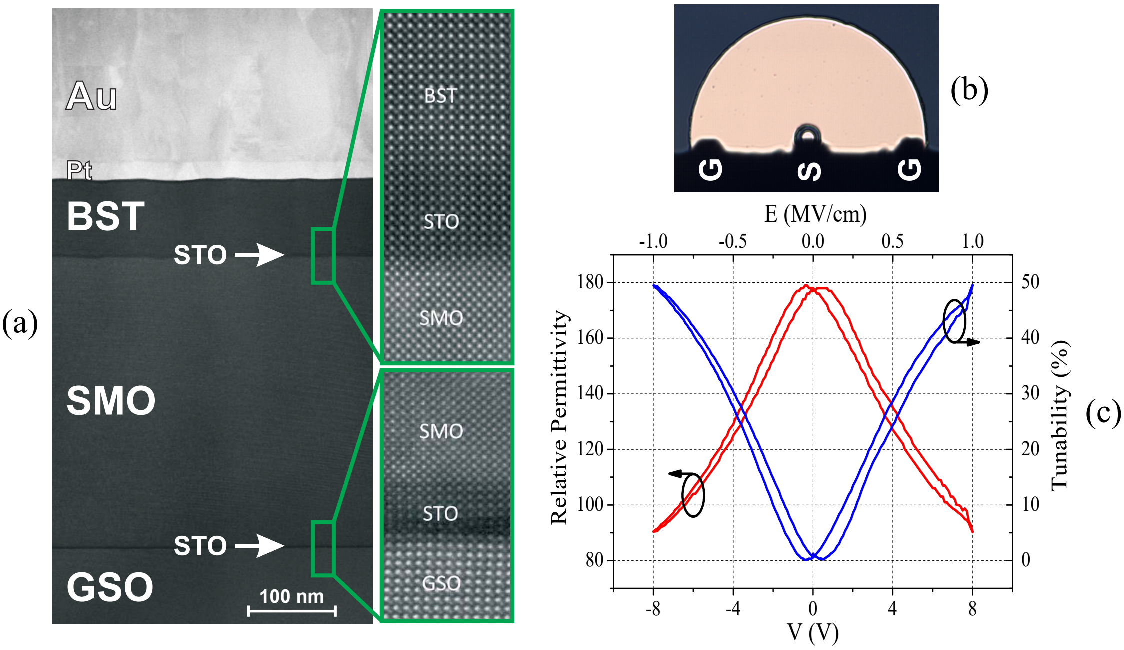

**Figure A.7:** (a) Scanning transmission electron microscope (STEM) image of the cross-section of the varactor. (b) Top view of the measured MIM varactor with positions of the GSG wafer probes (150 µm pitch). (c) Dependencies of relative permittivity $\varepsilon_r$ and tunability $\tau_\varepsilon$ of the Au/Pt/$Ba_{0.4}Sr_{0.6}TiO_3$/SMO varactor versus bias voltage $V$ and electric field $E$ measured at 100 MHz and room temperature.

values are 50 to 100 times higher than the ones previously reported for BST varactors with $SrRuO_3$ electrodes [61] and are the highest values of $K$ ever reported for BST varactors with oxide electrodes. The measurement result shows $K$ of $10^4$ at 100 MHz for the Au/Pt/BST/SMO varactors.

### Equivalent Circuit Modeling

Figure A.9 shows the lumped element equivalent circuit model of the parallel plate capacitor containing a contribution from the conductor and the dielectric losses. The parasitic capacitances and resistances (dashed lines in figure A.5(b)) are negligible in the measured frequency range [56]. Since the area of the outer ring is $\sim$400 times bigger than that of the inner circle, the capacitance of the BST of the outer ring can also be overlooked. As a result, the equivalent circuit of figure A.5(b) can be simplified as shown in figure A.9.

The series resistance $R_e$ represents the interconnect loss from the metal-dielectric interfaces and electrodes (the intrinsic properties of the conductor layer), and $L_s$ is the parasitic inductance of the electrodes. $C_{pt}$ represents the tunable ferroelectric capacitance (the core capacitance), and $R_{pd}$ represents the resistivity of the dielectric, which is frequency dependent and includes intrinsic film properties with parallel parasitic (fringing

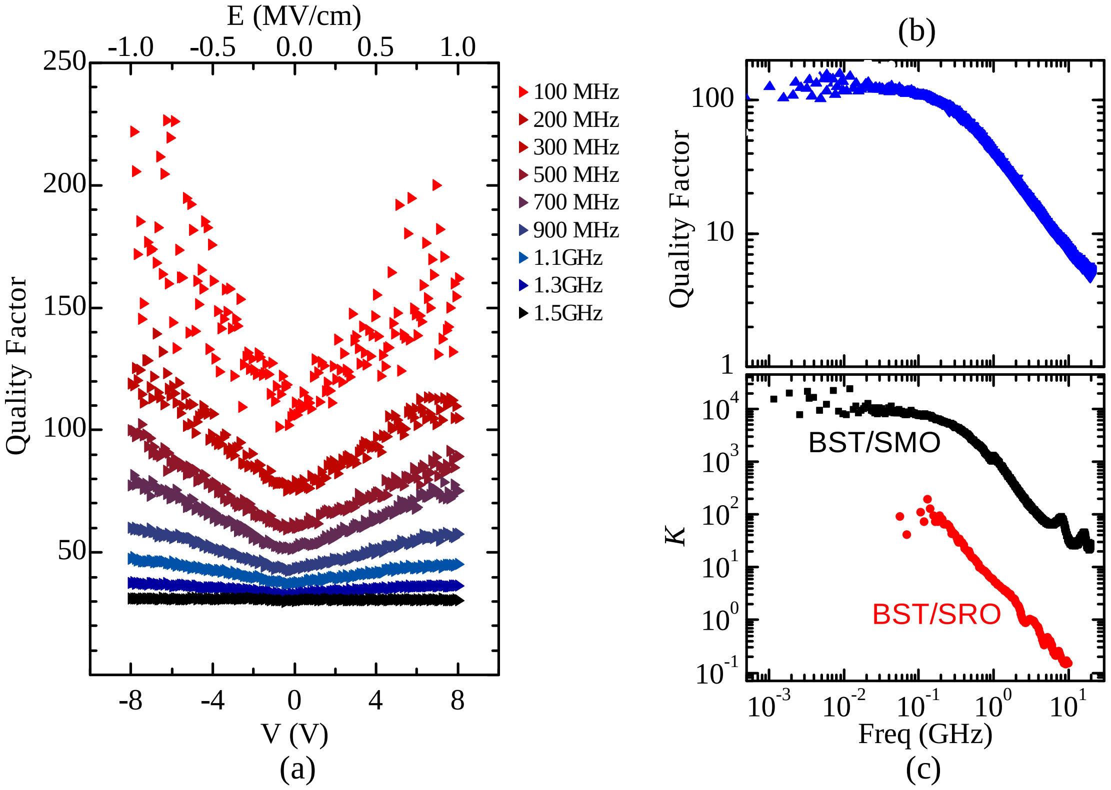

**Figure A.8:** (a) Quality factor of the MIM varactor with an inner circle diameter of $D_{in}$=20 µm versus biasing voltage/electrical field at different frequencies. (b) Quality factor of the MIM varactor versus frequency in the untuned state (0 V). (c) The commutation quality factor $K$ comparison of the varactors with bottom conductor layer of $SrRuO_3$ and $SrMoO_3$[61].

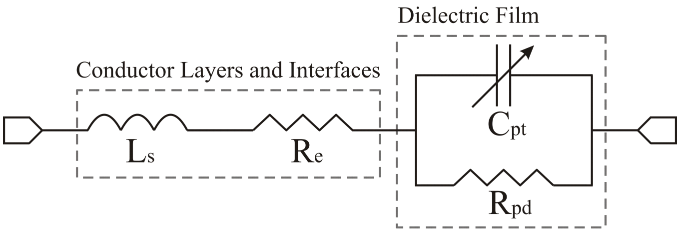

**Figure A.9:** The simple equivalent circuit model of the MIM varactor.

capacitance, the electrical length inductance, measurement error). Based on the equivalent circuit in figure A.9, the total measured impedance $Z_{\text{total}}$ follows:

$$Z_{\text{total}} = j\omega L_s + R_e + R_{pd}\frac{1}{1+Q_\varepsilon^2} + \frac{Q_\varepsilon^2}{j\omega C_{pt}(1+Q_\varepsilon^2)} \qquad \text{(A.1)}$$

where $Q_\varepsilon$ is the quality factor of the dielectric. By excluding the contribution of the parasitic inductance to the total impedance, the varactor's quality factor is given as:

$$\frac{1}{Q_{\text{total}}} = \tan\delta_{\text{total}} = \frac{1}{Q_e} + \frac{1}{Q_\varepsilon} \tag{A.2}$$

$$Q_\varepsilon = \frac{1}{\tan\delta_\varepsilon} = \omega R_{pd} C_{pt} \quad , \quad Q_e = \frac{1}{\tan\delta_e} = \frac{Q_\varepsilon^2}{\omega R_e C_{pt}(1+Q_\varepsilon^2)} \tag{A.3}$$

where $\tan\delta_\varepsilon$ is the dielectric loss. In the measurement by VNA, zero inductance for the GSG probe is assumed. However, this incorrect due to the presence of parasitic inductances [99]. The short, open, and load calibration standards are not ideal. Figure A.10(a) depicts the measured equivalent capacitance with additional inductances (post process correction) of $L_{\text{in}} = 0$, 4 ,8 and 12 pH. The capacitance value becomes constant over the frequency range by including an inductance $L_{in} \approx 12$ pH and integrating it with the measured impedance.

Figure A.10(b) illustrates the quality factor of the varactor with $D_{\text{in}} = 20\,\mu$m. The frequency domain MoM using ADS was employed to model the device and the measured S-parameter curves were fitted by that of the equivalent circuit (figure A.9). The measured, MoM simulated, equivalent circuit model curves (capacitance and quality factor) are in a good agreement over the whole frequency range from 100 MHz to 10 GHz.

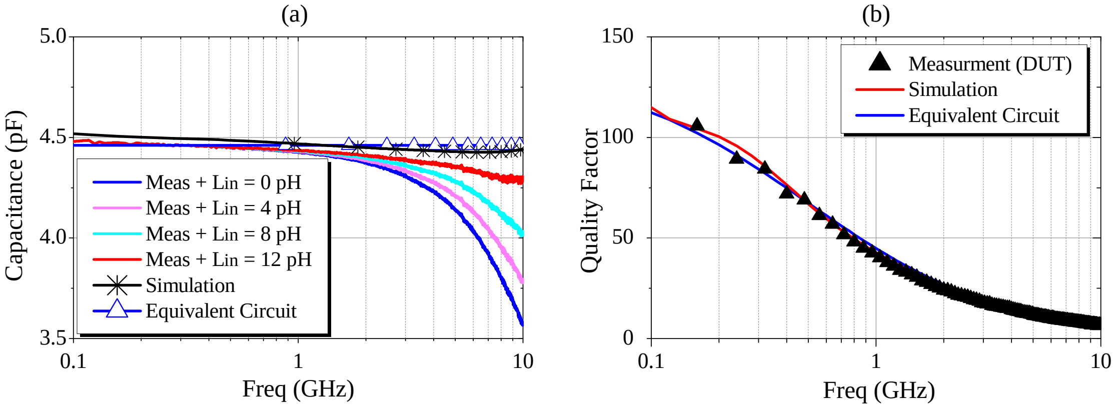

**Figure A.10:** (a) The measured equivalent capacitance with additional inductances of $L_{in} = 0$, 4, 8 and 12 pH, MoM simulation capacitance, and equivalent circuit capacitance versus frequency. (b) The varactor quality factor in the absence of DC bias (0 V and $L_{in} = 12$ pH) for measurement, MoM simulation, and equivalent circuit versus frequency.

The dielectric resistance $R_{pd}$ at very low frequencies is constant, however the dielectric impedance is smaller at high frequencies ($\sim 1/\omega$). The equivalent circuit can thus be approximated as a series LRC. By excluding $L_s$, the total quality factor can be estimated by $Q_e$ (equation A.3). The impedance of two test structures with similar outer, yet different inner diameters, can be used to calculate the sheet resistance $R_s$ of the bottom electrode, as well as the dielectric constant of the BST film [100]:

$$Z_1 - Z_2 = \frac{R_s}{2\pi} \ln \frac{D_2}{D_1} + \frac{1}{j\omega\pi\varepsilon_0\varepsilon_r} (\frac{1}{D_1^2} - \frac{1}{D_2^2}) \tag{A.4}$$

Assuming similar values of $L_s$ and $R_{pd}$ in the two test structures with $D_{\text{out}} = 400\,\mu\text{m}$ and inner diameters of $D_1 = 20\,\mu\text{m}$ and $D_2 = 40\,\mu\text{m}$, we obtained $R_s = 1.85\,\Omega/\square$ as the sheet resistance of the SMO layer. The resistivity of the SMO bottom electrode with thickness of 270 nm is subsequently calculated to be $50\,\mu\Omega\cdot\text{cm}$, which is in good agreement with the literature [85]. Using the above equation, the relative permittivity has a value of $\varepsilon_r = 180$.

The capacitance $C$ of the two parallel plates both of area $A$ separated by the thickness of the dielectric layer $d$ is calculated by $C{=}\varepsilon_0\varepsilon_r A/d$. In this case, the measured value is only $2\%$ different from the calculated $\varepsilon_r$. Therefore, the argument that the contribution of the outer ground capacitance is negligible is cogent.

The presented thin film varactor would be particularly attractive for low-voltage portable applications. However, further investigation needs to be carried out, especially for the patterning of the bottom oxide electrode and the BST layer, crucial for the realization of tunable phase shifters based on thin film varactors. One possible method would be to use a combination of photolithography and ion mill etching technology [10].

Because main limitation of the varactor quality factor at higher frequencies is the conductor resistivity of the SMO layer. On way to improve the quality factor is to increasing the thickness of the SMO bottom electrode, which is reducing the resistor of the conductor layer. The scalability and performance uniformity for prospective mass production rank as other important factors to be considered.

# Appendix B

# Fabrication Parameters

**Table B.1:** photolithography.

| Photoresist | comment |
|---|---|
| AZ 6632 (pos) | Electroplating more than 2 µm |
| AZ 1518 (pos) | Electroplating less than 2 µm |
| ma-N 490 (neg) | Lift-off process and electroplating less than 2 µm |

**Table B.2:** Conductor layer deposition parameters.

| Conductor | Method | Rate |
|---|---|---|
| Au | Thermal Evaporation | $11\,\mathrm{nm\,min^{-1}}$ |
| | Galvanization | $\leq 1.6\,\mathrm{nm\,s^{-1}}$ ($\leq 20\,\mathrm{\mu A\,mm^{-2}}$) |
| | RF-sputtering | $0.7\,\mathrm{nm\,s^{-1}}$ |
| Cr & Cr,Ni | Thermal Evaporation | $10\,\mathrm{nm\,min^{-1}}$ |
| Pt | RF-sputtering | $0.25\,\mathrm{nm\,s^{-1}}$ |

**Table B.3:** Conductor layers etchant solutions.

| Conductor | Etchant | Concentration | Rate (nm/s) |
|---|---|---|---|
| Au | $I_2$:KI:$H_2O$ | 1g:4g:40ml | 3 |
| Cr & Cr,Ni | $(NH_4)_2[Ce(NO_3)_6]$:$HNO_3$:$H_2O$ | 82.3g:45ml:500ml | 0.5 |

**Table B.4:** Expeimental etching results of $SrMoO_3$ and $SrMoO_4$.

| Etchant | Concentration | Rate (nm/s) |
|---|---|---|
| KOH | KOH 4 gr/Lit | 0.6 |
| KOH : $H_2O_2$ | 50ml (KOH 4 gr/Lit) +0.1ml $H_2O_2$ | 14.5 |
| AZ400 | AZ400 1:4 $H_2O$ | 0.7 |
| AZ400 : $H_2O_2$ | 50ml (AZ400 1:4 $H_2O$) +0.1ml $H_2O_2$ | 4 |

# Bibliography

[1] S.-W. Qu, P.-F. Li, S.-W. Y. Run-Liang, Xia and, J. Hu, and Z.-P. Nie, "Low-cost periodic sparse cavity-backed phased array based on multiport elements," *Antennas and Propagation, IEEE Transactions on*, vol. 63, pp. 4175–4179, Sept 2015.

[2] R. Romanofsky, "Array phase shifters: Theory and technology," in *Antenna Engineering Handbook*, 2007. ISBN: 9780071475747.

[3] V. K. Palukuru, J. Perntie, J. Jntti, and H. Jantunen, "Tunable microwave phase shifters using ltcc technology with integrated bst thick films," in *International Journal of Applied Ceramic Technology*, pp. 11–17, 2012.

[4] W. Hu, D. Zhang, M. Lancaster, T. Button, and B. Su, "Investigation of ferroelectric thick-film varactors for microwave phase shifters," *Microwave Theory and Techniques, IEEE Transactions on*, vol. 55, pp. 418–424, Feb 2007.

[5] S. Chandran, *Adaptive Antenna Arrays: Trends and Applications*. Springer Science & Business Media, 2013.

[6] M. Sazegar, *Phasedarray-Antennen mit integrierten Phasenschiebern auf ferroelektrischen Dickschichten*. PhD thesis, TU Darmstadt, 2013.

[7] C. A. Balanis, *Modern Antenna Handbook*. John Wiley & Sons, 2011.

[8] H. Bolandhemmat, M. Fakharzadeh, P. Mousavi, S. Jamali, G. Rafi, and S. Safavi-Naeini, "Active stabilization of vehicle-mounted phased-array antennas," *Vehicular Technology, IEEE Transactions on*, vol. 58, pp. 2638–2650, July 2009.

[9] M. I. SKOLNIK, *RADAR HANDBOOK*. ISBN: 0070579083, 1990.

[10] S. Gevorgian, "Ferroelectrics in microwave devices, circuits and systems: Physics, modelling, fabrication and measurements. engineering materials and processes," in *Springer,ISBN: 9781848825062*, 2009.

[11] Y. Zheng, *Reconfigurable Multiband RF Frontends with Tunable Ferroelectric Devices*. PhD thesis, TU Darmstadt, 2011.

[12] S. Koul and B. Bhat, *Microwave and Millimeter Wave Phase Shifters: Semiconductor and Delay Line Phase Shifters*. Artech House, ISBN: 9780890065853, 1992.

[13] S. Koul and B. Bhat, *Microwave and Millimeter Wave Phase Shifters: Dielectric and ferrite phase shifters*. Artech House, ISBN: 9780890063194, 1991.

[14] G. Rebeiz, *RF MEMS: Theory, Design, and Technology*. J. Wiley, ISBN: 9780471201694, 2003.

[15] H. D. L. Santos, G. Fischer, H. Tilmans, and J. van Beek, "Rf mems for ubiquitous wireless connectivity. part ii. application," *IEEE Microwave Magazine 5.4, pp. 5065. ISSN: 1527-3342*, 2004.

[16] S. Müller, *Grundlegende Untersuchungen steuerbarer passiver Flssigkristall-Komponenten fr die Mikrowellentechnik*. Dissertation in Technische Universitt Darmstadt, 2007.

[17] F. Gölden, *Liquid Crystal Based Microwave Components with Fast Response Times: Material, Technology, Power Handling Capability*. Dissertation in Technische Universitt Darmstadt, 2010.

[18] A. K. Tagantsev, V. O. Sherman, K. F. Astafiev, J. Venkatesh, and N. Setter, "Ferroelectric materials for microwave tunable applications," *In: Journal of Electroceramics 11.1-2, pp. 566*, 2003.

[19] R. J. Mailloux, *Phased Array Antenna Handbook*. 1993.

[20] K.-B. Kim, T.-S. Yun, H.-S. Kim, I.-D. Kim, H.-G. Kim, and J.-C. Lee, "Coplanar ferroelectric phase shifter on silicon substrate with tio2 buffer layer," *European Microwave Conf.*, 2005.

[21] B. Acikel, Y. Liu, A. S. Nagra, T. R. Taylor, P. J. Hansen, J. S. Speck, and R. A. York, "Phase shifters using (ba,sr)tio3 thin films on sapphire and glass substrates," *IEEE MTT-S Int. Microwave Symp.*, 2001.

[22] M. Nikfalazar, M. Sazegar, A. Friederich, C. Kohler, Y. Zheng, A. Wiens, J. Binder, and R. Jakoby, "Inkjet printed bst thick-films for x-band phase shifter and phased array applications," in *Antenna Technology (iWAT), 2013 International Workshop on*, pp. 121–124, March 2013.

[23] R. Romanofsky, J. Bernhard, F. Van Keuls, F. Miranda, G. Washington, and C. Canedy, "K-band phased array antennas based on ba0.60sr0.40 tio3 thin-film phase shifters," *Microwave Theory and Techniques, IEEE Transactions on*, vol. 48, pp. 2504–2510, Dec 2000.

[24] M. Sazegar, Y. Zheng, H. Maune, C. Damm, X. Zhou, J. Binder, and R. Jakoby, "Low-cost phased-array antenna using compact tunable phase shifters based on ferroelectric ceramics," *Microwave Theory and Techniques, IEEE Transactions on*, vol. 59, pp. 1265–1273, May 2011.

[25] F. Zimmermann, *Steuerbare Mikrowellendielektrika aus ferroelektrischen Dickschichten*. PhD thesis, Dissertation. Institut fr Werkstoffe der Elektrotechnik - IWE Karlsruhe, 2003.

[26] K. Yeo, W. Hu, M. Lancaster, B. Su, and T. Button., “Thick film ferroelectric phase shifters using screen printing technology,” *Proceedings of the 34th European Microwave Conference 13, S. 14891492.*, 2004.

[27] V. Palukuru, J. Perntie, M. Komulainen, T. Tick, and H. Jantunen, “Tunable microwave devices using low-sintering-temperature screen-printed barium strontium titanate (bst) thick films,” *Journal of the European Ceramic Society 30.2, S. 389394.*, 2010.

[28] A. Friederich, *Tintenstrahldruck steuerbarer Mikrowellenkomponenten Prozess-, Material- und Bauteilentwicklung*. PhD thesis, TU Darmstadt, 2014.

[29] H. Maune, *Design und Optimierung hochlinearer ferroelektrischer Varaktoren fr steuerbare Hochfrequenz-Leistungsverstrker*. PhD thesis, TU Darmstadt, 2011.

[30] A. K. Tagantsev, V. O. Sherman, K. F. Astafiev, J. Venkatesh, and N. Setter, “Ferroelectric materials for microwave tunable applications,” *Journal of Electroceramics, Vol 11, PP 566,*, 2003.

[31] M. C. Petty, *Molecular Electronics: From Principles to Practice*. 2007.

[32] J. Li, Y. Liu, Y. Zhang, H.-L. Cai, and R.-G. Xiong, “Molecular ferroelectrics: where electronics meet biology,” *Phys. Chem. Chem. Phys, 15, 20786-20796*, 2013.

[33] J.-H. Jeon, “Effect of srtio3 concentration and sintering temperature on microstructure and dielectric constant of ba1-xsrxtio3,” *Journal of the European Ceramic Society 24*, 2004.

[34] W. Menesklou, F. Paul, X. Zhou, H. Elsenheimer, J. R. Binder, and E. Ivers-Tiffee, “Nonlinear ceramics for tunable microwave devices,” *Microsyst Technol*, 2011.

[35] M. Steer and W. D. Palmer, *Multifunctional Adaptive Microwave Circuits and Systems*. SciTech Publishing, 2009.

[36] N. Setter, *Electroceramic-Based MEMS, Fabrication-Technology and Applications*. Springer, Science+Business Media, Inc., New York, Vol. 9, 2005.

[37] J. Stringer and B. Derby, “Limits to feature size and resolution in ink jet printing,” *J. Eur. Ceram. Soc., Vol. 29, No. 5, pp. 913918,*, 2009.

[38] B. Derby, “Inkjet printing ceramics: From drops to solid,” *J. Eur. Ceram. Soc., Vol. 31, No. 14, pp. 25432550*, 2011.

[39] B. de Gans, P. Duineveld, and U. Schubert, “Inkjet printing of polymers: state of the art and future developments,” *Adv. Mater. 16, 203*, 2004.

[40] E. Tekin, P. J. Smith, and U. S. Schubert, “Inkjet printing as a deposition and patterning tool for polymers and inorganic particles,” *The Royal Society of Chemistry*, 2008.

[41] A. Friederich, C. Kohler, M. Sazegar, M. Nikfalazar, R. Jakoby, J. Binder, and W. Bauer, “Preparation of integrated passive microwave devices through inkjet printing,” in *Proceedings of the 9th International Concerence and Exhibition on Ceramic Interconnect and Ceramic Microsystems Technologies (CICMT)*, 2013.

[42] A. Friederich, C. Kohler, M. Nikfalazar, A. Wiens, M. Sazegar, R. Jakoby, W. Bauer, and J. R. Binder, “Microstructure and microwave properties of inkjet printed barium strontium titanate thick-films for tunable microwave devices,” *Journal of the European Ceramic Society 34, Nr. 12, S. 2925-2932*, 2014.

[43] A. Friederich, C. Kohler, M. Nikfalazar, A. Wiens, R. Jakoby, W. Bauer, and J. R. Binder, “Inkjet-printed metal-insulator-metal capacitors for tunable microwave applications,” *International Journal of Applied Ceramic Technology*, pp. n/a–n/a, 2014.

[44] J. Stringer and B. Derby, “Formation and stability of lines produced by inkjet printing,” *Langmuir, 26 (12), pp 1036510372*, 2010.

[45] X. Zhou, M. Sazegar, F. Stemme, J. Hauelt, R. Jakoby, and J. Binder, “Correlation of the microstructure and microwave properties of ba0.6sr0.4tio3 thick-films,” *J. Eur. Ceram. Soc., Vol. 32, No. 16, pp. 43114318*, 2012.

[46] C. Kohler, M. Nikfalazar, A. Friederich, A. Wiens, M. Sazegar, R. Jakoby, and J. R. Binder, “Fully screen-printed tunable microwave components based on optimized barium strontium titanate thick films,” *International Journal of Applied Ceramic Technology*, vol. 12, pp. E96–E105, 2014.

[47] C. Kohler, A. Friederich, M. Sazegar, M. Nikfalazar, F. Stemme, D. Wang, C. Kuebel, R. Jakoby, and J. R. Binder, “Effects of zno-b2-o3 addition on the microstructure and microwave properties of low-temperature sintered barium strontium titanate (bst) thick films,” *International Journal of Applied Ceramic Technology*, vol. 10, pp. E200–E209, 2013.

[48] B. Derby, “Inkjet printing of functional and structural materials: Fluid property requirements, feature stability, and resolution,” *Annu. Rev. Mater. Res., Vol. 40, pp. 395414*, 2010.

[49] C. Kohler, *Anorganische Barium-Strontium-Titanat-Komposite für die Hochfrequenztechnik*. PhD thesis, TU Darmstadt, 2015.

[50] Q. Zhang, J. Zhai, and X. Jao, “Low loss, high tunability of ba0. 4sr0. 6tio3mg3b2o6 microwave composite ceramics,” *In: Journal of American Ceramic Society, 93.9, pp. 25602562*, 2010.

[51] Q. Zhang, J. Zhai, and X. Jao, “Dielectric and percolative properties of ba0. 5sr0. 5tio3mg3b2o6 composite ceramics,” *In: Journal of American Ceramic Society, 93.4, pp. 11381142*, 2011.

[52] E. Carlsson and S. Gevorgian, “Conformal mapping of the field and charge distributions in multilayered substrate cpws,” *Microwave Theory and Techniques, IEEE Transactions on*, vol. 47, pp. 1544–1552, Aug 1999.

[53] C. Weil, *Passiv steuerbare Mikrowellenphasenschieber auf der Basis nichtlinearer Dielektrika*. PhD thesis, TU Damstadt, 2003.

[54] W. Heinrich, “Quasi-tem description of mmic coplanar lines including conductor-loss effects,” *Microwave Theory and Techniques, IEEE Transactions on*, vol. 41, pp. 45–52, Jan 1993.

[55] M. Nikfalazar, A. Friederich, C. Kohler, M. Sazegar, Y. Zheng, A. Wiens, J. R. Binder, and R. Jakoby, “Metal-isolator-metal varactor based on inkjet-printed tunable ceramics,” in *Microwave Conference (GeMIC), 2014 German*, pp. 1–4, March 2014.

[56] P. Bao, T. J. Jackson, X. Wang, and M. J. Lancaster, “Barium strontium titanate thin film varactors for room-temperature microwave device applications,” *J. Phys. D. Appl. Phys., vol. 41, no. 6, p. 063001*, 2008.

[57] C. A. Balanis, *Antenna Theory, 2nd ed.* New York: Wiley, 1997.

[58] A. J. Fenn and P. T. Hurst, *Ultrawideband Phased Array Antenna Technology for Sensing and Communications Systems*. MIT Lincoln Laboratory Series, 2015.

[59] J. B. L. Rao, D. P. Patel, P. K. Park, T. K. Dougherty, J. A. Zelik, D. S. Prior, A. Moffat, and L. C. Sengupta, “Application of ferroelectrics in low-cost microwave phased-array antennas,” *Mat. Res. Soc. Symp. Proc. Vol. 720 Materials Research Society*, 2002.

[60] I. Vendik, V. Pleskachev, and O. Vendik, “Figure of merit and limiting characteristics of tunable ferroelectric microwave devices,” *Progress In Electromagnetics Research Symposium , Hangzhou, China, August 22-26*, 2005.

[61] K. Khamchane, A. Vorobiev, T. Claeson, and S. Gevorgian, “Ba0.25sr0.75tio3 thin-film varactors on srruo3 bottom electrode,” *J. Appl. Phys. 99, 034103*, 2006.

[62] M. Nikfalazar, C. Kohler, D. Kienemund, A. Wiens, Y. Zheng, M. Sohrabi, J. Binder, and R. Jakoby, “Frequency extension of the fully printed phase shifter by paste composite optimization,” in *Microwave Conference (GeMiC), 2015 German*, pp. 146–149, March 2015.

[63] Y. Horii, C. Caloz, and T. Itoh, "Super-compact multilayered left-handed transmission line and diplexer application," *Microwave Theory and Techniques, IEEE Transactions on*, vol. 53, pp. 1527–1534, April 2005.

[64] B. Lee, S. Kahng, and Q. Wu, "Compact uwb bandpass filter as cascaded center-tapped crlh transmission-line zors for improved stopband," *Journal of Electrical Engineering and Technology (JEET)*, Vol. 8, No. 2, March 2013.

[65] A. Kozyrev and D. Van Der Weide, "Nonlinear wave propagation phenomena in left-handed transmission-line media," *Microwave Theory and Techniques, IEEE Transactions on*, vol. 53, pp. 238–245, Jan 2005.

[66] C. Damm, M. Schussler, M. Oertel, and R. Jakoby, "Compact tunable periodically lc loaded microstrip line for phase shifting applications," in *Microwave Symposium Digest, 2005 IEEE MTT-S International*, pp. 4 pp.–, June 2005.

[67] M. Nikfalazar, M. Sazegar, Y. Zheng, A. Wiens, R. Jakoby, A. Friederich, C. Kohler, and J. R. Binder, "Compact tunable phase shifter based on inkjet printed bst thick-films for phased-array application," in *Microwave Conference (EuMC), 2013 European*, pp. 432–435, Oct 2013.

[68] P. Scheele, *Steuerbare passive Mikrowellenkomponenten auf Basis hochpermittiver ferroelektrischer Schichten. Dissertation.* PhD thesis, TU Darmstadt, 2007.

[69] M. J. Rodwell, M. Kamegawa, R. Yu, M. Case, E. Carman, and K. Giboney, "Gaas nonlinear transmission lines for picosecond pulse generation and millimeter-wave sampling," *Microwave Theory and Techniques, IEEE Transactions on*, vol. 39, pp. 1194–1204, Jul 1991.

[70] A. S. Nagra and R. A. York, "Distributed analog phase shifters with low insertion loss," *IEEE Transactions on Microwave Theory and Techniques*, vol. 47, pp. 1705–1711, Sep 1999.

[71] M. Nikfalazar, C. Kohler, A. Heunisch, A. Wiens, Y. Zheng, B. Schulz, M. Mikolajek, M. Sohrabi, T. Rabe, J. R. Binder, and R. Jakoby, "Ltcc phase shifters based on tunable ferroelectric composite thick films," *Frequenz. Journal of RF-Engineering and Telecommunications, Volume 69, Issue 11-12, pages 451-455*, Jan 2015.

[72] K. Yeo, M. Lancaster, B. Su, and T. Button, "Distributed transmission line phase shifter with loaded bst capacitors using thick film technology," *Proceedings of the Mediterranean Microwave Symposium*, 2004.

[73] W. Hu, D. Zhang, M. Lancaster, K. Yeo, T. Button, and B. Su, "Cost effective ferroelectric thick film phase shifter based on screen-printing technology," *Proceedings of the IEEE MTT-S International Microwave Symposium, S. 591594.*, 2005.

[74] W. Hu, D. Zhang, M. Lancaster, T. Button, and B. Su, “Investigation of ferroelectric thick-film varactors for microwave phase shifters,” *IEEE Transactions on Microwave Theory and Techniques 55.2, S. 418424.*, 2007.

[75] A. Giere, C. Damm, P. Scheele, and R. Jakoby, “Lh phase shifter using ferroelectric varactors,” in *2006 IEEE Radio and Wireless Symposium*, pp. 403–406, Oct 2006.

[76] M. Nikfalazar, A. Wiens, M. Mikolajek, A. Friederich, C. Kohler, M. Sohrabi, Y. Zheng, D. Kienemund, S. Melnyk, J. R. Binder, and R. Jakoby, “Tunable phase shifter based on inkjet-printed ferroelectric mim varactors,” *Frequenz. Journal of RF-Engineering and Telecommunications*, 2014.

[77] G. Kumar and K. Ray, “Broadband microstrip antennas,” *Artech House antennas and propagation library, page number:132-138, ISBN 1-58053-244-6,2003.*, 2003.

[78] A. Kishk, “Dielectric resonator antenna, a candidate for radar applications,” *Radar Conference, 2003. Proceedings of the 2003 IEEE*, May 2003, pp. 258 – 264.

[79] A. Petosa, *Dielectric Resonator Antenna Handbook.* Artech House, 2007.

[80] A. Mehmood, M. Nikfalazar, M. Sohrabi, R. Jakoby, M. Hovhanisyan, and M. Letz, “Bulk-glass ceramic based stacked dielectric resonator antenna as phased array element,” in *Microwave Conference (EuMC), 2015 European*, pp. 1331–1334, Sept 2015.

[81] M. Hovhannisyan, H. Braun, Y. Zheng, A. Mehmood, M. Letz, and R. Jakoby, “Bulk-glass ceramics with two microwave crystalline phases for antenna elements in wireless communications,” *Ferroelectrics conference Shefield UK*, Feb 2013.

[82] A. Mehmood, O. Karabey, M. Ayluctarhan, Y. Zheng, H. Braun, M. Hovhannisyan, M. Letz, and R. Jakoby, “Dielectric resonator antenna phased array with liquid crystal based phase shifters,” *Antennas and Propagation (EuCAP), 8th European Conference on , vol., no., pp.2436,2439, 6-11*, April 2014.

[83] R. Kumar Mongia and A. Ittipiboon, “Theoretical and experimental investigations on rectangular dielectric resonator antennas,” *Antennas and Propagation, IEEE Transactions on*, vol. 45, pp. 1348–1356, Sep 1997.

[84] M. A. Khalid, “Mutual coupling and beam steering analysis of patch and dielectric resonator antenna,” Master’s thesis, TU Darmstadt, 2015.

[85] A. Radetinac, A. Mani, S. Melnyk, M. Nikfalazar, J. Ziegler, Y. Zheng, R. Jakoby, L. Alff, and P. Komissinskiy, “Highly conducting srmoo3 thin films for microwave applications,” *Appl. Phys. Lett. 105, 114108*, 2014.

[86] P. Rundqvist, T. Liljenfors, A. Vorobiev, E. Olsson, and S. Gevorgian, “The effect of sio2, pt, and pt/au templates on the microstructure and permittivity of baxsr 1-xtio3films,” *J. Appl. Phys., vol. 100, no. 11, p. 114116*, 2006.

[87] R. Schafranek, S. Payan, M. Maglione, and A. Klein, “Barrier height at (ba,sr)tio3/pt interfaces studied by photoemission,” *Phys. Rev. B, vol. 77, no. 19, pp. 3033*, 2008.

[88] J. H. Haeni, P. Irvin, W. Chang, and D. G. Schlom, “Room-temperature ferroelectricity in strained srtio3,” *Nature, vol. 430, no. August, pp. 758761*, 2004.

[89] S. Sheng, X.-Y. Zheng, P. Wang, and C. Ong, “Effect of bottom electrodes on dielectric properties of high frequency ba0.5sr0.5tio3 parallel plate varactor,” *Thin Solid Films, vol. 518, no. 10, pp. 28642866*, 2010.

[90] A. Vorobiev and et al., “Microwave loss mechanisms in ba0.25sr0.75tio3 thin film varactors,” *Journal of Applied Physics, Oct. 15, pp. 4642-4649, vol. 96, No. 8.*, 2004.

[91] K. Khamchane, A. Vorobiev, T. Claeson, and S. Gevorgian, “Ba0.25sr0.75tio3 thin-film varactors on srruo3 bottom electrode,” *J. Appl. Phys., vol. 99, no. 3, p. 034103*, 2006.

[92] Q. Jia, X. Wu, S. Foltyn, and P. Tiwari, “Structural and electrical properties of ba0.5sr0.5tio3 thin films with conductive srruo3 bottom electrodes,” *Appl. Phys. Lett. 66, 21972199*, 1995.

[93] B. Nagaraj, T. Sawhney, S. Perusse, S. Aggarwal, R. Ramesh, V. S. Kaushik, S. Zafar, R. E. Jones, J. H. Lee, V. Balu, and J. Lee, “(ba,sr)tio3 thin films with conducting perovskite electrodes for dynamic random access memory applications,” *Applied Physics Letters, Volume 74*, 1999.

[94] K. Khamchane, Y. Boikov, and Z. Ivanov, “Temperature and electric field response of a dielectric (ba,sr)tio3 layer between perovskite-type manganite electrodes,” *Ann. Phys, 13, 12, S. 103 - 105*, 2004.

[95] I. Nagai, N. Shirakawa, S. Ikeda, R. Iwasaki, H. Nishimura, and M. Kosaka, “Highest conductivity oxide srmoo3 grown by a floating-zone method under ultralow oxygen partial pressure,” *Appl. Phys. Lett. 87, 024105*, 2005.

[96] R. Schafranek, S. Payan, M. Maglione, and A. Klein, “Barrier height at (ba,sr)tio3/pt interfaces studied by photoemission,” *Phys. Rev. B 77, 195310*, 2008.

[97] A. Vorobiev, P. Rundqvist, K. Khamchane, and S. Gevorgian, “Silicon substrate integrated high q-factor parallel-plate ferroelectric varactors for microwave/millimeterwave applications,” *Appl. Phys. Lett. 83, 3144*, 2003.

[98] G. Subramanyam, M. W. Cole, N. X. Sun, T. S. Kalkur, N. M. Sbrockey, G. S. Tompa, X. Guo, C. Chen, S. P. Alpay, G. A. Rossetti, K. Dayal, L. Chen, and D. G. Schlom, "Challenges and opportunities for multi-functional oxide thin films for voltage tunable radio frequency/microwave components," *Journal of Applied Physics 114, 191301; doi: 10.1063/1.4827019*, 2013.

[99] M. Tiggelman, K. Reimann, J. Liu, M. Klee, W. Keur, R. Mauczock, J. Schmitz, and R. Hueting, "Identifying dielectric and resistive electrode losses in high-density capacitors at radio frequencies," in *Microelectronic Test Structures, 2008. ICMTS 2008. IEEE International Conference on*, pp. 190–195, March 2008.

[100] Z. Ma, A. J. Becker, P. Polakos, H. Huggins, J. Pastalan, H. Wu, K. Watts, Y. H. Wong, and P. Mankiewich, "Rf measurement technique for characterizing thin dielectric films," *IEEE Trans. Electron Devices, vol. 45, no. 8, pp. 18111816*, 1998.

# Own Publications

### Articles in Journals

[1] M. Nikfalazar, M. Sazegar, A. Mehmood, A. Wiens, A. Friederich, H. Maune, Joachim R. Binder, and R. Jakoby: Two-Dimensional Beam Steering Phased Array Antenna With Compact Tunable Phase Shifter Based on BST Thick-Films, *Antennas and Wireless Propagation Letters, IEEE*, vol.PP, no.99, pp.1-1, Juli. 2016.

[2] M. Nikfalazar, C. Kohler, A. Wiens, A. Mehmood, M. Sohrabi, H. Maune, Joachim R. Binder, and R. Jakoby: Beam Steering Phased Array Antenna with Fully Printed Phase Shifters Based on Low-Temperature Sintered BST-Composite Thick Films, *Microwave and Wireless Components Letters, IEEE*, vol. 26, no. 1, pp. 70-72, Jan. 2016.

[3] M. Nikfalazar, A. Mehmood, M. Sohrabi, M. Mikolajek, A. Wiens, H. Maune, C. Kohler, Joachim R. Binder, and R. Jakoby: Steerable Dielectric Resonator Phased Array Antenna Based on Inkjet-Printed Tunable Phase Shifter with BST Metal-Insulator-Metal Varactors, *Antennas and Wireless Propagation Letters, IEEE*, vol. 15, no. , pp. 877-880, March. 2016.

[4] M. Nikfalazar, C. Kohler, A. Heunisch, A. Wiens, Y. Zheng, B. Schulz, M. Mikolajek, M. Sohrabi, T. Rabe, J. R. Binder, R. Jakoby: LTCC Phase Shifters Based on Tunable Ferroelectric Composite Thick Films, *Frequenz. Journal of RF-Engineering and Telecommunications*, volume 69, issue 11-12, pages 451-455, Jan 2015.

[5] M. Nikfalazar, A. Wiens, M. Mikolajek, A. Friederich, C. Kohler, M. Sohrabi, Y. Zheng, D. Kienemund, S. Melnyk, Joachim R. Binder, and R. Jakoby: Tunable Phase Shifter Based on Inkjet-Printed Ferroelectric MIM Varactors, *Frequenz. Journal of RF-Engineering and Telecommunications, volume 69, issue 1-2, pages 39-46*, Jan 2015.

[6] A. Mani, M. Nikfalazar, F. Muench, A. Radetinac, Y. Zheng, A. Wiens, S. Melnyk, H. Maune, L. Alff, R. Jakoby, P. Komissinskiy: Wet Chemical Etching of SrMoO3 Thin Films, *Materials Letters*, volume 184, pages 173-176, Dec 2016.

[7] A. Radetinac, A. Mani, S. Melnyk, M. Nikfalazar, J. Ziegler, Y. Zheng, R. Jakoby, L. Alff, P. Komissinskiy: Highly conducting SrMoO3 thin films for microwave applications, *Applied Physics Letters*, vol.105, no.11, pp.114108,114108-5, 2014.

[8] A. Friederich, C. Kohler, M. Nikfalazar, A. Wiens, M. Sazegar, R. Jakoby, W. Bauer, and J. R. Binder: Microstructure and microwave properties of inkjet printed barium

strontium titanate thick-films for tunable microwave devices, *Journal of the European Ceramic Society 34, Nr. 12, PP. 2925-2932*, 2014.

[9] A. Friederich, C. Kohler, M. Nikfalazar, A. Wiens, R. Jakoby, J.R. Binder: Inkjet-Printed Metal-Insulator-Metal Capacitors for Tunable Microwave Applications, , *International Journal of Applied Ceramic Technology, 12 (S1), E164-173*, 2015.

[10] M. Sazegar, Y. Zheng, C. Kohler, H. Maune, M. Nikfalazar, Joachim R. Binder, and R. Jakoby: Beam Steering Transmitarray Using Tunable Frequency Selective Surface With Integrated Ferroelectric Varactors, *Antennas and Propagation, IEEE Transactions on*, vol.60, no.12, pp.5690,5699, Dec 2012.

[11] C. Kohler, A. Friederich, M. Sazegar, M. Nikfalazar, F. Stemme, D. Wang, C. Kuebel, R. Jakoby, and J.R. Binder: Effects of ZnOB2O3 Addition on the Microstructure and Mi- crowave Properties of Low-Temperature Sintered Barium Strontium Titanate (BST) Thick Films, *International Journal of Applied Ceramic Technology*, 2013, 10.S1, E200E209.

[12] C. Kohler, M. Nikfalazar, A. Friederich, A. Wiens, M. Sazegar, R. Jakoby, and Joachim R. Binder: Fully Screen-Printed Tunable Microwave Components Based on Optimized Barium Strontium Titanate Thick Films, *International Journal of Applied Ceramic Technology*, 2015, 12: E96E105.

**Articles in Conferences and Workshops**

[13] M. Nikfalazar, A. Mehmood, M. Sohrabi, A. Wiens, Y. Zheng, H. Maune, M. Mikolajek, A. Friederich, C. Kohler, J. R. Binder, and R. Jakoby : Low Bias Voltage Tunable Phase Shifter Based on Inkjet-Printed BST MIM Varactors for C/X-Band Phased Arrays, *Proc. 45th European Microwave Conf., IEEE*, 2015.

[14] M. Nikfalazar, C. Kohler, A. Wiens, Y. Zheng, M. Sohrabi, Joachim R. Binder, and R. Jakoby: Frequency Extension of the Fully Printed Phase Shifter by Paste Composite Optimization, *Germany Microwave Conference (GeMIC), IEEE*, 2015.

[15] M. Nikfalazar, A. Friederich, C. Kohler, Y. Zheng, A. Wiens, Joachim R. Binder, and R. Jakoby: Fully Inkjet-Printed Tunable S-Band Phase Shifter on BST Thick Film, *Proc. 44th European Microwave Conf., IEEE*, 2014.

[16] M. Nikfalazar, M. Sazegar, A. Friederich, C. Kohler, Y. Zheng, A. Wiens, Joachim R. Binder, and R. Jakoby: Metal-Isolator-Metal Varactor Based on Inkjet-Printed Tunable Ceramics, *Germany Microwave Conference (GeMIC), IEEE*, 2014.

[17] M. Nikfalazar, C. Kohler, A. Friederich, M. Sazegar; Y. Zheng, A. Wiens, Joachim R. Binder, and R. Jakoby: Fully printed tunable phase shifter for L/S-band phased array application, *Microwave Symposium (IMS), IEEE MTT-S International*, 2014.

[18] M. Nikfalazar, M. Sazegar, Y. Zheng, A. Wiens, A. Friederich, C. Kohler, Joachim R. Binder, and R. Jakoby: Compact tunable phase shifter based on inkjet printed BST

thick-films for phased-array application, *Proc. 43th European Microwave Conf., IEEE*, 2013.

[19] M. Nikfalazar, M. Sazegar, A. Friederich, C. Kohler, Y. Zheng, A. Wiens, Joachim R. Binder, and R. Jakoby: Inkjet printed BST thick-films for X-band phase shifter and phased array applications, *International Workshop on Antenna Technology (iWAT), IEEE*, 2013.

[20] M. Nikfalazar, M. Sazegar, Y. Zheng, H. Maune, A. Mehmood, and R. Jakoby: Tunable Split Ring Resonators ( SRR ) Filter based on Barium-Strontium-Titanate Thick Film, *Germany Microwave Conference (GeMIC), IEEE*, 2012.

[21] A. Friederich, C. Kohler, M. Sazegar, M. Nikfalazar, R. Jakoby, J.R. Binder, and W. Bauer: Preparation of Integrated Passive Microwave Devices Through Inkjet Printing, *Proceedings of the 9th International Conference and Exhibition on Ceramic Interconnect and Ceramic Microsystems Technologies*, 2013, S. 238245.

[22] A. Wiens, S. Preis, C. Kohler, D. Kienemund, H. Maune; O. Bengtsson, M. Nikfalazar, J.R. Binder, W. Heinrich, R. Jakoby: Tunable In-Package Impedance Matching for High Power Transistors Based on Printed Ceramics, *Proc. 45th European Microwave Conf., IEEE*, 2015.

[23] A. Mehmood, M. Nikfalazar, M. Sohrabi, R. Jakoby, M. Hovhanisyan and M. Letz: Bulk-Glass Ceramic Based Stacked Dielectric Resonator Antenna As Phased Array Element , *Proc. 45th European Microwave Conf., IEEE*, 2015.

[24] D. Kienemund, M. Nikfalazar, C. Kohler, A. Friederich, A. Wiens, H. Maune, M. Mikolajeky, Joachim R. Binder, and R. Jakoby: Temperature dependence of a tunable phase shifter based on inkjet printing technology, *Germany Microwave Conference (GeMIC), IEEE*, 2015.

[25] A. Wiens, S. Preis, C. Schuster, M. Nikfalazar, C. Damm, M. Schuessler, W. Heinrich, O. Bengtsson, and R. Jakoby: Wideband tunable GaN HEMT module utilizing thin-film BST varactors for efficiency optimization, *Microwave Symposium (IMS), IEEE MTT-S International*, 2016.

[26] H. Maune, M. Nikfalazar, C. Schuster, T. Franke, W. Hu, M. Nickel, D. Kienemund, A. Prasetiadi, C. Weickhmann, M. Jost, A. Wiens, and R. Jakoby: Tunable microwave component technologies for SatCom-platforms, *Germany Microwave Conference (GeMIC), IEEE*, 2016.

### Conference Presentations

[27] A. Friederich, C. Kohler, M. Sazegar, M. Nikfalazar, R. Jakoby, J.R. Binder, and W. Bauer: Inkjet printing of tunable microwave devices, *5th International Conference on Shaping of Advanced Ceramics*, 2013.

[28] A. Friederich, C. Kohler, M. Sazegar, M. Nikfalazar, R. Jakoby, J.R. Binder, and W. Bauer: Preparation of Integrated Passive Microwave Devices Through Inkjet Printing, *Ceramic Interconnect and Ceramic Microsystems Technologies*, 2013.

[29] C. Kohler, A. Friederich, D. Wang, M. Nikfalazar, M. Sazegar, R. Jakoby, and J.R. Binder: Microstructure and microwave properties of low temperature sintered BST (Ba0.6Sr0.4TiO3) thick-films and their applicability to co-firing processes, *10th Pacific Rim Conference on Ceramic and Glass Technology*, 2013.

[30] A. Friederich, C. Kohler, M. Nikfalazar, M. Sazegar, R. Jakoby, J.R. Binder, and W. Bauer: Inkjet printing of tunable microwave devices, *10th Pacific Rim Conference on Ceramic and Glass Technology*, 2013.

[31] A. Friederich, C. Kohler, M. Nikfalazar, M. Sazegar, R. Jakoby, J.R. Binder, and W. Bauer: Tintenstrahlgedruckte Dickschicht-Kondensatoren fr steuerbare Mikrowellenbauteile, *Jahrestagung der Deutschen Keramischen Gesellschaft*, 2014.

[32] C. Kohler, A. Friederich, M. Nikfalazar, A. Wiens, R. Jakoby, J.R. Binder: Gedruckte Varaktoren fr die Mikrowellentechnik, *Gemeinschaftsausschuss Hochleis-tungskeramik von DGM und DKG, 5.Sitzung des Arbeitskreises Funktionskeramik*, 2014.

[33] C. Kohler, A. Wiens, J. Xu, B. Kubina, M. Nikfalazar, R. Jakoby, J. R. Binder: Novel fabrication methods for ferroelectric-dielectric composite ceramics and their potential of tailoring the microwave dielectric properties, *11th Pacific Rim Conference on Ceramic and Glass Technology*, 2015.

**Conference Posters**

[34] C. Kohler, A. Friederich, M. Sazegar, M. Nikfalazar, D. Wang, R. Jakoby, and J.R. Binder: Niedrig-sinternde Ba0,6Sr0,4TiO3 (BST)-Dickschichten und deren Anwendbarkeit auf Co- Sinter-Prozesse, *Jahrestagung der Deutschen Keramischen Gesellschaft*, 2013.

[35] A. Friederich, C. Kohler, M. Sazegar, M. Nikfalazar, R. Jakoby, J.R. Binder, and W. Bauer: Preparation of Integrated Passive Microwave Devices Through Inkjet Printing, *Ceramic Interconnect and Ceramic Microsystems Technologies*, 2013.

[36] A. Friederich, C. Kohler, M. Nikfalazar, M. Sazegar, R. Jakoby, J.R. Binder, and W. Bauer: Tintenstrahldruck steuerbarer Dickschicht-Kondensatoren fr Hochfrequenzanwendungen, *Jahrestagung der Deutschen Keramischen Gesellschaft*, 2014.

[37] M.T. Arnous, A. Wiens, S. Preis,H. Maune, K. Bathich, M. Nikfalazar,R. Jakoby, G. Boeck: Load-modulated GaN power amplifier implementing tunable thick film BST components, *Microwave Integrated Circuits Conference (EuMIC)*, pp.416,419, 2013.

[38] A. Wiens, M.T. Arnous, H. Maune, M. Sazegar, M. Nikfalazar, C. Kohler, J.R. Binder, G. Boeck, R. Jakoby: Load modulation for high power applications based on printed ceramics, *Microwave Symposium Digest (IMS), IEEE MTT-S International*, 2013.

## Awards

1. Best Paper Award as First Author

*International Workshop on Antenna Technology (iWAT), IEEE*, 2013

2. Poster Award as Co-author

*Jahrestagung der Deutschen Keramischen Gesellschaft*, 2013

3. Poster Award as Co-author

*9th International Conference and Exhibition on Ceramic Interconnect and Ceramic Microsystems Technologies*, 2013

## Patent

A. Radetinac, A. Mani, P. Komissinskiy, L. Alff, M. Nikfalazar, *'Mikroelektronische Elektrodenanordnung'*, Eingereicht: 12.02.2016, Amtliches Aktenzeichen: 10 2016 102 501.1

## Supervised Work

1. M. Sohrabi, *'Dielectric Resonator Phased Array with Inkjet Printed Tunable Ferroelectric MIM-Varactors Phase Shifters'*, Master Thesis (D 2224-M), 2015.

2. M. Rasteh, *'Tunable diplexer for a reconfigurable uplink and downlink of a satellite communication system at C-band'*, Master Thesis (D 2237-M), 2015.

# Abbreviations

| **Abbreviation** | **Meaning** |
|---|---|
| ADS | Advanced Design System |
| BST | Barium Strontium Titanate |
| BW | Bandwidth |
| CD | charged defect |
| CPW | Coplanar Waveguide |
| DR | Dielectric Resonator |
| DRA | Dielectric resonator antenna |
| FoM | Figure of Merit |
| GSG | Ground-signal-ground |
| GS | Ground-signal |
| HRTEM | High Resolution Transmission Electron Microscopy |
| IDC | Interdigital Capacitor |
| LC | Liquid Crystals |
| LTCC | Low Temperature Co-fired Ceramics |
| MoM | Method of Moment |
| MEMS | Micro Electromechanical Systems |
| MIM | Metal Insulator Metal |
| MMIC | Monolithic Microwave Integrated Circuit |
| PLD | Pulsed Laser Deposition |
| PPA | Phased Array Antenna |
| PS | Phase Shift |
| RF | Radio frequency |
| RFID | Radio-frequency Identification |
| SEM | Scanning Electron Microscopy |
| SLL | Side Lobe Level |
| VNA | Vector Network Analyser |

# Curriculum Vitae

## Personal Data

Name: Mohammad Nikfalazar
Date of birth: 21.09.1983
Birth Place: Tehran, Iran

## Education

**2001-2005**
B.Sc. in Electrical Engineering, Major Option in Telecommunication, Azad University Branch: Shahrerey, Tehran, Iran

**2005-2008**
M.Sc. in Electrical Engineering; Major Option in Optics and Microwave Engineering, K. N. Toosi University of Technology, Tehran, Iran

**2011-2016**
Dr.-Ing. in Electrical Engineering; specialization in Microwave Engineering, TU Darmstadt, Darmstadt, Germany

Darmstadt 06.07.2016
Mohammad Nikfalazar